36. Particle Detectors for Non-Accelerator Physics

Revised March 2026. See the various sections for authors.

36.1 Introduction

Non-accelerator experiments have become increasingly important in particle physics and astrophysics. From them comes the evidence of physics beyond the SM, with the discovery of neutrino oscillations and adiabatic flavor conversion. Explored energies range from the meV scale to above the EeV, some 24 orders of magnitude. The physics and the design of the detectors vary as a consequence. Some experiments look at astrophysical high-energy phenomena using the atmosphere as a detector in the fluorescence and Cherenkov observatories or the polar ice and the ocean water in neutrino telescopes. Experiments on extremely rare events, such as neutrino-less double beta decay, solar neutrinos and dark matter induced scattering, need dedicated fully equipped deep underground laboratories, existing in different countries. Critical is the research to push back the ultra-low radioactive background frontier, with dedicated facilities in these laboratories. Detectors range from hyper-pure liquid scintillators, both organic and not, to thermalized and ballistic phonon detectors at the sub-Kelvin temperature, to dual phase noble fluid TPCs, etc. Space-based detectors also use some unique instrumentation, but these are beyond the present scope of this review. Gravitational wave detectors are not included as well.

36.2 High-energy cosmic-ray hadron and gamma-ray detectors

36.2.1 *Atmospheric fluorescence detectors*

Revised October 2025 by F. Salamida (L'Aquila U.; INFN, LNGS).

Cosmic-ray fluorescence detectors (FDs) use the atmosphere as a giant calorimeter to measure isotropic scintillation light that traces the development profiles of extensive air showers. An extensive air shower (EAS) is produced by the interactions of ultra high-energy ($E > 10^{17}$ eV) subatomic particles in the stratosphere and upper troposphere. The amount of scintillation light generated by an EAS is proportional to the energy deposited in the atmosphere and nearly independent of the primary species. With energies extending beyond 10^{20} eV, ultra high energy cosmic rays (UHECRs) are the highest energy subatomic particles known to exist. In addition to particle arrival directions, energy spectra and primary composition, the astroparticle science investigated with FDs also includes multi-messenger studies, searches for high energy photons, neutrinos, monopoles and deeply penetrating forms of dark matter. The Pierre Auger Observatory FD also measures UV scintillation that traces the development of ring-shaped atmospheric transient luminous events, called Elves, in the ionosphere that are initiated by strong lightning [1]. Similar phenomena have also been observed from space by Mini-EUSO [2].

Previous experiments with FDs included the pioneering Fly's Eye [3,4], and the High Resolution Fly's Eye (HiRes and HiRes prototype) [5]. The use of atmospheric nitrogen fluorescence to detect extensive air showers was proposed in the 1950's by Greisen and Chudakov, and further developed in the 1960's through the systematic studies of Bunner [6,7]. The current generation of experiments include the Telescope Array (TA) [8] in the northern hemisphere, and the larger Pierre Auger Observatory (Auger) [9] in the southern hemisphere. (Discussion, with extensive references, of current and possible future UHECR experiments can be found[in [10].) Auger and TA are hybrid observatories. Their FD telescopes overlook sparse arrays of particle detectors on the ground. Select parameters are listed in Table 36.1. TA and Auger have each one FD site populated with additional telescopes that view up to 60° in elevation to measure lower EASs using a combination of scintillation and direct Cherenkov light. As part of a fourfold coverage upgrade of TA (TAx4), 12 HiRes refurbished telescopes have been installed at the north and south-east sites of TA. A set of prototype fluorescence telescopes, known as FAST [11], has been developed as a cost-effective design for next-generation ultra-high energy cosmic ray observatories. These small-aperture telescopes, equipped with a single wide field-of-view photomultiplier and simple optics, have been successfully deployed and operated at both the Telescope Array site and the Pierre Auger Observatory, where they have detected air showers and validated the concept. A similar approach is being pursued by the CRAFFT [12] project in Japan, which uses Fresnel lenses and single-PMT readout to achieve comparable goals of simplicity and scalability.

The fluorescence light is emitted primarily between 290 and 430 nm (Figure 36.1) with major lines at 337, 357, and 391 nm, when relativistic charged particles, primarily electrons and positrons, excite nitrogen molecules in air, resulting in transitions of the 1P and 2P systems. Reviews and references for the pioneering and recent laboratory measurements of fluorescence yield, $Y(\lambda, P, T, u)$, including dependence on wavelength (λ), temperature (T), pressure (p), and humidity (u) may be found in Refs. [13–15]. The results of various laboratory experiments have been combined (Figure 36.2) to obtain an absolute average and uncertainty for Y(337 nm, 800 hPa, 293 K, dry air) of 7.04 ± 0.24 ph/ MeV after corrections for different electron beam energies and other factors. The units of ph/ MeV correspond to the number of fluorescence photons produced per MeV of energy deposited in the atmosphere by the electromagnetic component of an EAS.

An FD element (telescope) consists of a non-tracking spherical mirror of less than astronomical quality, a"camera" of photomultiplier tubes (PMTs) near the focal plane, and a flash ADC readout

Table 36.1: Parameters of major fluorescence detectors. Note 1: Year when all FD sites were operational. Note 2: At TA 1 of the 3 FD sites features 24 telescopes from the HiRes experiment. Note 3: A-C for one telescope where A is the full area and C the area obscured by the camera and support structures. Thus A-C is the effective light collecting area. For the modified Schmidt design at Auger, the area of the entrance pupil, A, is listed because the pupil is smaller than the mirror and thus defines the entrance aperture. For the other experiments, the area of the mirror, A, is listed

Observatory	Fly's Eye	HiRes	Telescope Array	Pierre Auger
Location	Dugway UT US	Dugway UT US	Delta UT US	Malargüe AR
Start-End	1981-1992	1996-2006	2008-present	2005-present
Sites (note 1)	2 (1986)	2 (1999)	3 (2008)	4 (2008)
Separation	3.3 km	12.6 km	31-40 km	39-62 km
Telescopes/site	67,18	21,42	12+8,12,14+10+4	6, 6, 6, 6+3
Pixel FOV	5.5°	1°	1°	1.5°
Telescope FOV Azi×Elv	≈18°×≈18°	16°×13.5°	18°×15° (note 2)	30°×28.1°
Light collection area (note 3)	$1.95\,\mathrm{m}^2$ - $0.25\,\mathrm{m}^2$	$3.72\,\mathrm{m}^2$ - $0.5\,\mathrm{m}^2$	$6.8\,\mathrm{m}^2$ - $0.85\,\mathrm{m}^2$ (for 2 sites)	$3.80\,\mathrm{m}^2$ - $0.80\,\mathrm{m}^2$ (modified schmidt)
Energy Scale Uncertainty	≤40%	≈20%	≈20%	14%

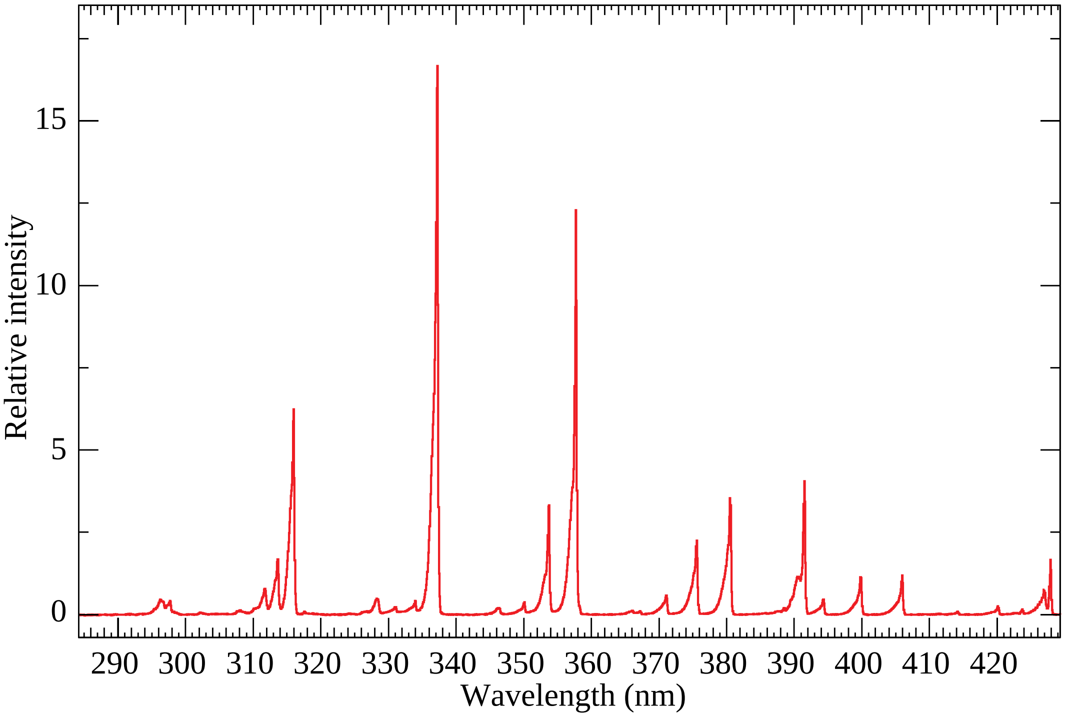

Figure 36.1: Measured fluorescence spectrum excited by 3 MeV electrons in dry air at 800 hPa and 293 K. Airfly experiment. Figure from Ref [16].

system with a pulse and track-finding trigger scheme [9, 18]. The major experiments listed in

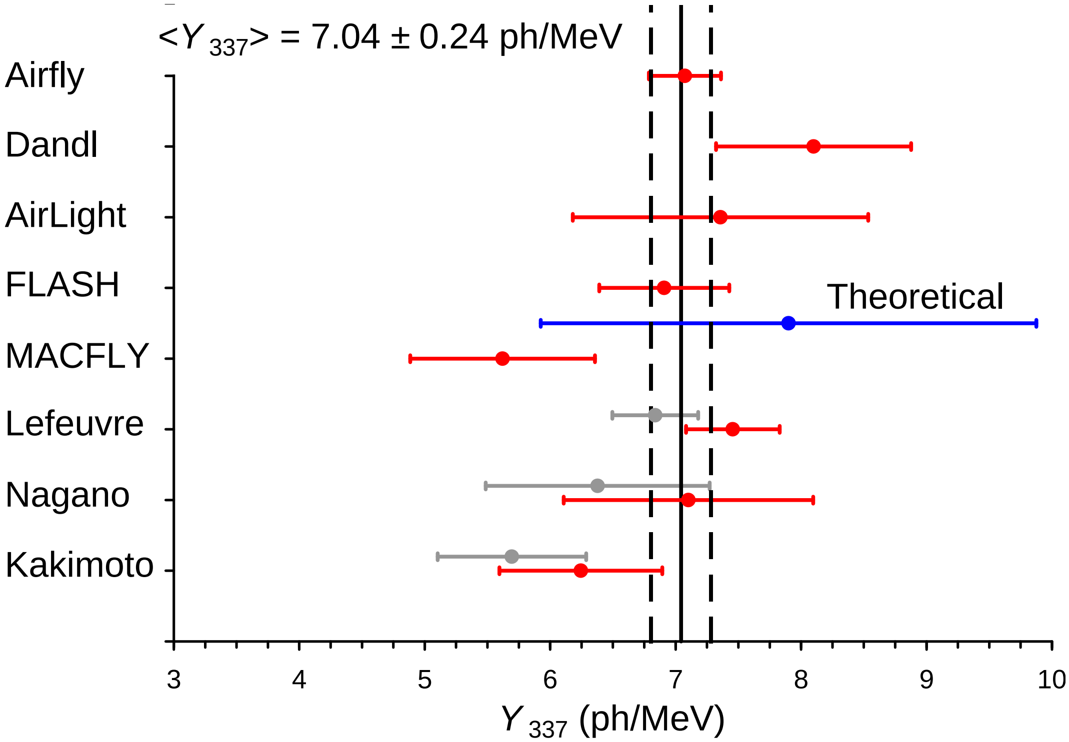

Figure 36.2: Fluorescence yield values and associated uncertainties at 337 nm (Y_{337}) in dry air at 800 hPa and 293 K The methodology and corrections that were applied to obtain the average and the uncertainty are discussed extensively in this reference. The vertical axis denotes different laboratory experiments that measured FY. The gray bars show three of the original measurements to illustrate the scale of the corrections applied. Figure from Ref [17].

Table 36.1 all use conventional PMTs (for example, Hamamatsu R9508 or Photonis XP3062) with grounded cathodes and AC coupled readout. Segmented mirrors have been fabricated from slumped or slumped/polished glass with an anodized aluminum coating or fabricated using shaped aluminum that was then chemically anodized with $AlMgSiO_5$. A broadband UV filter (custom fabricated, BG-3, or Schott MUG-6) reduces background light such as starlight, airglow, man-made light pollution, and airplane strobe-lights.

At 10^{20} eV, where the flux drops below 1 EAS/km^2 century, the aperture for an eye of adjacent FD telescopes that span the horizon can reach 10^4 km^2 sr. FD operation requires (nearly) moonless nights and clear atmospheric conditions, which typically imposes a duty cycle of about 10%. Arrangements of LEDs, calibrated diffuse sources [19], pulsed UV lasers [20], LIDARs [1] and IR detectors that are sensitive to clouds are used for photometric calibration, atmospheric calibration [21], and determination of exposure [22]. For purposes of optical transmission, the atmosphere is treated as having a dominant molecular component and a secondary aerosol component. The latter is well described [23] by molecular scattering theory and models derived from radiosonde measurements. The aerosol component can include dust, haze and pollution and the aerosol optical depth profile must be measured on site in the UV during FD data taking.

The EAS generates a track consistent with a light source moving at $v = c$ across the FOV. The number of photons (N_γ) as a function of atmospheric depth (X) can be expressed as [14]

---

[1] LIDAR stands for "Light Detection and Ranging" and refers here to systems that measure atmospheric properties from the light scattered backwards from laser pulses directed into the sky.

$$\frac{\mathrm{d}N_\gamma}{\mathrm{d}X} = \frac{dE^{\mathrm{tot}}_{\mathrm{dep}}}{dX} \int Y(\lambda, P, T, u) \cdot \tau_{\mathrm{atm}}(\lambda, X) \cdot \varepsilon_{\mathrm{FD}}(\lambda)\mathrm{d}\lambda, \tag{36.1}$$

where $\tau_{atm}(\lambda, X)$ is the atmospheric transmission, including wavelength (λ) dependence, and $\varepsilon_{\mathrm{FD}}(\lambda)$ is the FD efficiency. $\varepsilon_{\mathrm{FD}}(\lambda)$ includes geometric factors and collection efficiency of the optics, quantum efficiency of the PMTs, and other throughput factors. The typical systematic uncertainties, τ_{atm} (10%) and $\varepsilon_{\mathrm{FD}}$ (photometric calibration 10%), currently dominate the systematic uncertainty the absolute EAS energy scale. FD energy resolution, defined as event-to-event statistical uncertainty, is typically less than 10% for final data samples used for science analysis.

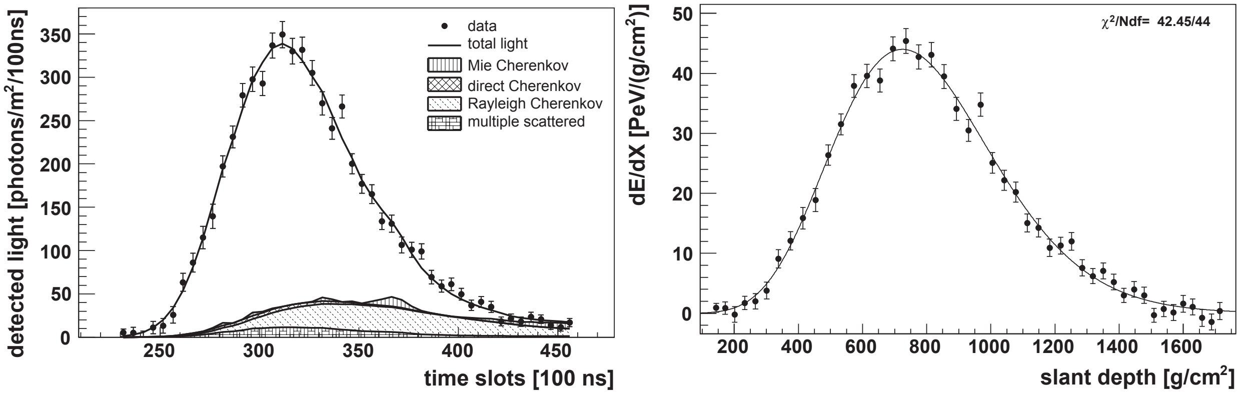

Figure 36.3: Example light profile (left) of one EAS recorded by the Pierre Auger FD and the corresponding profile (right) of energy deposited in the atmosphere vs atmospheric slant depth. The light profiles include the estimated components of Cherenkov light that have been scattered out of the forward beam by the molecular and aerosol (Mie) components of the atmosphere. The reconstructed energy of this EAS was $3.0 \pm 0.2 \times 10^{19}$ eV. Figure from Ref [24].

Analysis methods to reconstruct the EAS profile and deconvolve the contributions of re-scattered scintillation light, and direct and scattered Cherenkov light are described in [3] and more recently in [25]. The EAS energy is typically obtained by integrating over the Gaisser-Hillas function [26]

$$E_{\mathrm{cal}} = \int_0^\infty [w_{\mathrm{max}} \left(\frac{X - X_0}{X_{\mathrm{max}} - X_0}\right)^{(X_{\mathrm{max}} - X_0)/\lambda} e^{(X\mathrm{max} - X)/\lambda}]\mathrm{d}X, \tag{36.2}$$

where E_{cal} is the energy of electromagnetic energy component of the EAS and X_{max} is the atmospheric slant depth at which the shower reaches its maximum energy deposit rate. This maximum dE/dX is denoted as w_{max}. X_0 and λ are two shape parameters. Recent analyses adopt a modified Gaisser–Hillas parameterization that decouples the width L and asymmetry R, improving the robustness of the fit [27].

The energy of the primary cosmic ray is obtained by correcting E_{cal} upward by about 10% to account for the invisible energy carried by particles that do not interact in the atmosphere. Auger reported a data-driven method to estimate the invisible energy from the muon number at ground level and Xmax to reduce systematic uncertainties [28]. Energy resolution, $\Delta E/E$, of 15-20% is achievable, provided the geometric fit of the EAS axis is constrained, typically by multi-eye stereo projection or hybrid observations, and the profile fit of EAS development along the track is constrained by the observed rise and fall about X_{max}. An example of a recorded EAS light profile and its corresponding dE/dX development profile are shown in Fig. 36.3. In 2023, the Pierre Auger Collaboration released a public dataset [29] of the 100 highest energy cosmic ray events collected over a 17-year span through 2020 with an additional 9 energetic hybrid events used in the calibration procedure. In 2024 the Pierre Auger Collaboration published the first systematic comparison of $X_{\max}$ measured with radio and fluorescence techniques for the same set of 53 air showers, finding no significant bias (-3.9 ± 11.2 g/cm^2) and a resolution better than 15 g/cm^2 [30]. These results also benefit from the ongoing *AugerPrime* upgrade [31]. Besides enhancing the surface-detector array with the installation of Surface Scintillator Detectors (SSD) and dedicated radio antennas, AugerPrime also deploys new front-end electronics that provide higher sampling speed and dynamic range, thereby enabling a more accurate time synchronisation of FD–SD coincident events. Recent results also show excellent agreement between the radio and FD-based energy scales, providing a strong and independent validation of the energy scale determined by the FD [32].

An FD that would look down on the Earth's atmosphere from orbit, and thus monitor a far larger area than any ground-based instrument, is an active area of R&D. Prototypes already flown include the pioneering TUS instrument [33, 34] (2016–2018 on the Lomonosov satellite). The JEM-EUSO collaboration has tested balloon pathfinders in 2014 (EUSO-Balloon) [35], 2017 (EUSO-SPB1) [36], and 2023 (EUSO-SPB2) [37]. During its 2023 flight the EUSO-SPB2 mission recorded UV signals compatible with extensive air showers using both a fluorescence and a Cherenkov telescope, providing a critical validation of the optical and trigger systems planned for future orbital detectors [37, 38]. The Mini-EUSO [39] FD continues recording terrestrial UV emission by looking down through a 25 cm diameter UV-transmitting window inside the International Space Station since 2019.

Looking ahead, the Probe of Extreme Multi-Messenger Astrophysics (POEMMA) is in the NASA Probe-class pre-proposal phase. Its baseline design foresees two wide-field Schmidt satellites flying in formation to observe UHECRs and cosmogenic tau neutrinos from space [40, 41].As a precursor to the satellite mission, the POEMMA collaboration is developing a super-pressure balloon pathfinder (PBR), combining fluorescence, Cherenkov, and radio detectors, with a launch planned in 2027 [42].

36.2.2 *Atmospheric Cherenkov telescopes for high-energy gamma ray astronomy*

Revised October 2025 by W. Hofmann (MPIK).

A wide variety of astrophysical objects produce high-energy γ-ray photons. Leptonic or hadronic particles, accelerated to relativistic energies, produce γ-rays typically through inverse Compton boosting of ambient photons or through the decay of neutral pions produced in hadronic interactions. Below some 10s of GeV, γ-ray emission can be efficiently detected using satellite or balloon-borne instrumentation, with an effective area approximately equal to the size of the detector (typically $< 1\,\mathrm{m}^2$). At higher energies, a technique with much larger effective collection area is required to measure astrophysical γ-ray fluxes, which decrease rapidly with increasing energy. Atmospheric Cherenkov detectors achieve effective collection areas of $> 10^5\,\mathrm{m}^2$ by using the Earth's atmosphere as an intrinsic part of the detection technique. A hadronic cosmic ray or high energy γ-ray incident on the Earth's atmosphere induces a particle cascade, or air shower. Relativistic charged particles in the air shower generate Cherenkov radiation, which is emitted along the shower direction. For vertically incident γ-rays in the TeV range, the maximum emission occurs at an altitude of $\sim$10 km [43]. Following absorption and scattering in the atmosphere [43], the Cherenkov light at ground level peaks at a wavelength $\lambda \approx 300$–350 nm. At typical observatory altitudes of 1-2 km a.s.l., Cherenkov light illuminates a light pool with a radius of $\sim$120-130 m, with roughly uniform light intensity across the light pool [43, 44]. Beyond the light pool radius, the intensity of Cherenkov light decreases rapidly. More deeply penetrating higher-energy γ-ray showers generate a peaked intensity distribution, distant showers at large zenith angles a larger light pool [43, 44]. The intensity is approximately proportional to the energy of the primary γ-ray, and is typically $\sim$100 photons/m^2 for a vertical 1 TeV primary, arriving in a brief flash of a few nanoseconds. The light yield varies with the seasonal atmospheric density profile, by 10% or more [43]. The Cherenkov pulse can be detected by using large reflecting surfaces to focus the Cherenkov light onto fast photo sensors. See [45, 46] for accounts of the historical development of the technique, [47] for a recent overview, and [48] for an exhaustive compilation of materials.

Imaging atmospheric Cherenkov telescopes (IACTs), such as H.E.S.S., MAGIC and VERITAS, use large (> 100 m^2) segmented mirrors on steerable mounts to focus the Cherenkov light onto arrays of photosensors (referred to as the "cameras") that record a Cherenkov image of each air shower. The intensity, shape and orientation of the Cherenkov images are used to reconstruct the γ-ray energy and arrival direction, and to discriminate γ-ray primaries from cosmic rays that provide a uniform background. Images resulting from purely electromagnetic γ-ray induced cascades appear as narrow, elongated ellipses in the camera. The long axis of the ellipse corresponds to the vertical extension of the air shower, and points back towards the source position in the field-of-view. If multiple telescopes are used to view the same shower ("stereoscopy"), the source position is simply the intersection point of the various image axes. Cosmic-ray primaries produce secondaries with large transverse momenta, which initiate sub-showers. Their images are consequently wider and less regular than those with γ-ray primaries. Reflecting the distance to the air shower maximum ($\sim$10 km for vertical incidence) and the scale of transverse structures in γ-ray showers (some 10 meters), IACT cameras mostly use relatively coarse pixel sizes in the range of $0.08° - 0.19°$ (Table 36.2). The image of a $\sim$10 km long air shower viewed at $\sim$100 m impact distance extends over roughly one degree, hence cameras need to provide fields of view of few degrees. Most modern instruments have larger fields of view, up to 10°, to cover extended γ-ray sources and enable sky surveys. Table 36.2 lists major IACT systems operating or under construction; all are stereoscopic systems, that provide improved resolution of the γ-ray direction and higher background rejection compared to single telescopes. Whereas in the operating few-telescope stereoscopic systems the telescopes are distributed over an area of the scale of the light pool radius – to ensure that multiple telescopes are illuminated by a given shower – the systems under construction use larger numbers of IACTs, covering areas larger than the light pool, and providing effective detection areas on the scale of 10^6 m^2.

IACTs are deployed at sites with dark skies and a large number of clear nights. Most IACT sites are well above sea level, at 1-2 km elevation (VERITAS, H.E.S.S., MAGIC, CTAO). Altitudes in the 4-5 km range provide lower energy thresholds [58]; for example, the MACE telescope [59] is located at 4.3 km a.s.l. IACTs benefit from sites with low geomagnetic field; large transverse fields spread the shower and reduce performance by $\sim 1\%$ per μG field [44]. At typical sites, IACTs log about 1000 - 1500 h per year, also depending on the level of moon light up to which telescopes are operated.

Traditionally, IACTs use single-mirror optics for imaging; for cost reasons, segmented mirrors are used. Mirror facet size ranges from $\sim 0.3\,\mathrm{m}^2$ to ~ 2 m^2, increasingly moving from aluminized ground-glass mirrors to lightweight composite sandwich structures. For mirror diameters d up to 10 - 15 m (VERITAS, H.E.S.S. CT1-4, CTAO MST), mostly Davies-Cotton optics is used, with facets of focal length f arranged on a shell of radius f, whereas larger mirrors use a parabolic shape (MAGIC, H.E.S.S. CT5, CTAO LST). Davies-Cotton optics provides better imaging over an extended field of view, but is not isochronous; for large telescopes the time dispersion is significant compared to the (ns) Cherenkov signal time scales. The off-axis point spread function (PSF) of single-mirror telescopes deteriorates rapidly with decreasing f/d [60, 61]; large f on the other hand results in large cameras and heavy support structures. As a compromise, $f/d \approx 1.0 - 1.3$ is typically chosen. Dual-mirror Schwarzschild-Coulder optics was proposed [62] to provide a near-uniform PSF across fields of view up to 10°, and a small plate scale suitable for silicon photo multipliers (SiPM).

Table 36.2: Parameters of major IACT systems, operating or under construction. In the optics line, DC stands for Davies-Cotton, DC' for modified DC, P for parabolic, SC' for modified Schwarzschild-Couder. "Max. tel. dist." is the maximum distance between pairs of telescopes, as a measure for the extent of the array. The CTAO telescope numbers refer to the "alpha" configuration.

	H.E.S.S.		MAGIC	VERITAS	ASTRI	CTAO			LACT
Site	Namibia		La Palma	Arizona, US	Tenerife	La Palma and Chile			Sichuan, China
Altitude [m]	1800		2200	1300	2400	2200 / 2100			4400
Max. tel. dist. [m]	170		85	170	500	600 / 1800			1200
Status (2025)	Operational		Operational	Operational	Construction	Construction			Construction
Reference	[49]		[50,51]	[52,53]	[54]	[55]			[56,57]
Telescopes	CT1-4	CT5				SST	MST	LST	
Number	4	1	2	4	9	0 / 37	9 / 14	4 / 0	32
Mirror dia. [m]	12	28	17	12	4.3	4.3	11.5	23	6
Focal len. [m]	15	36	18	12	2.2	2.2	16	28	8
Optics	DC	P	P	DC	SC'	SC'	DC'	P	DC
FoV [deg.]	5.0	3.4	3.5	3.5	10.5	8.8	7.7 / 7.5	4.3	8
Pixel size [deg.]	0.16	0.08	0.1	0.15	0.19	0.16	0.17	0.1	0.19
Pixel number	960	1758	1039	499	2368	2048	1855/1764	1855	1616
Photodet.	PMT	PMT	PMT	PMT	SiPM	SiPM	PMT	PMT	SiPM

The first IACTs to implement Schwarzschild-Couder optics are the pSCT prototype telescope [63], and the ASTRI and CTAO SST telescopes. IACTs are usually focused on the height of shower maximum (about 10 km for vertical TeV γ-rays). For very large telescopes (d beyond 25 - 30 m), the finite depth of field limits telescope performance; Plenoscope optics [64] has been proposed as a way out. Alt-az mounts are generally employed to point IACTs, either using a central positioner (e.g. VERITAS, CTAO MSTs) or – in particular for larger telescopes - a cradle on a circular rail (e.g. H.E.S.S., MAGIC). Positioning speeds range from 20 s (CTAO LST) to 1-2 minutes. Cameras use mostly photomultipliers (PMTs), with a peak quantum efficiency (QE) approaching 40%, but silicon sensors (SiPM) as pioneered in the FACT telescope [65] are increasingly used (pSCT, ASTRI, CTAO SST, LACT) since they can operate under high illumination (moonlight) and provide higher QE, but not necessarily a better performance (signal to noise) for detecting the Cherenkov photons; see [66] for a comparison. A disadvantage of SiPMs is their red-sensitivity resulting in high night-sky background (NSB) rates unless filtered. Even with the blue-sensitive PMT response, night-sky background rates are in the range of few 100 MHz per pixel, for large mirrors. To avoid pile-up of NSB, exposure time for Cherenkov images should not exceed a few ns. For signal recording, either fast Flash-ADC systems used, or 1-2 GHz analog capacitor pipelines that store signals until a trigger decision is obtained. In most modern cameras, the full readout electronics is housed in the camera body. Triggering is usually multi-level, with a first-level decision based on the camera image using a coincidence or signal sum of neighboring pixels, followed by a second-level decision requesting a coincidence of multiple telescopes and initiating data transfer to storage. Camera-level triggers typically require about 50-100 detected photons in an air shower image; readout rates are in the kHz range.

For an overview of data analysis techniques, see e.g. [67]. The simplest form of image reconstruction parametrizes images by an ellipse (Hillas parameters) and reconstructs the shower direction from the intersection of image ellipses [68]. A wide range of improved reconstruction algorithms is used, in particular fits of the image distribution using semi-analytical [69] or MC-generated [70] image templates. Cosmic-ray rejection in its simplest form uses the size of the minor axis of the image ellipse to remove cosmic-ray showers; advanced techniques use the quality-of-fit of gamma-ray image templates, and/or machine learning using a wide range of image parameters. For optimizing the analysis, and determining effective detection areas, extensive Monte Carlo simulations are used, frequently based on the CORSIKA [71] air shower simulator. Lacking a "test beam" and relying on the atmosphere as detection medium, the absolute calibration of IACTs is challenging. Intensity of muon rings is one means for calibrating the telescope response [72], and atmospheric monitoring by independent devices (e.g. LIDARs [73]) or via the telescope trigger rates serves to monitor atmospheric transmission. Low-level image and air shower reconstruction is usually performed using custom software, but high-level analysis is increasingly relying on open-source packages such as Gammapy [74]. While cosmic rays are effectively rejected, still background remains that must be subtracted in the study of γ-ray sources. Techniques for background determination [75] include pointing the telescope offset from the source, and using off-regions distributed symmetrically to the telescope axis; using event rates in a ring around the source; globally fitting a background level from the full field of view; or using dedicated off-runs pointing towards an empty region of sky.

At low energies, where the light intensity in the Cherenkov light pool is below the trigger threshold of a telescope, IACTs only trigger because of fluctuations in shower development or light yield, and the trigger probability and hence the effective detection areas increase steeply with energy. Once the intensity in the light pool matches the trigger threshold, the effective area starts to saturate at $\sim 10^5$ m^2 (for vertical incidence on a single telescope or telescope array with size not larger than the light pool). Typical angular resolutions of telescope systems are $\sim$5 arc-min, but arc-min scale resolution can be achieved for well-reconstructed high-energy events. Typical γ-ray energy resolution is $\sim$10%. In the image analysis, 99% or more of the cosmic rays can be rejected based on image shapes; an additional factor of $\gg 100$ suppression can be gained from an angular cut around the (point) source position. Sensitivity is usually quoted as the minimally detectable point-source γ-ray energy flux $E^2 F_{min}(E)$ in a 0.2 decade energy band. Fig. 36.4 illustrates the flux sensitivity of IACT systems. At low energy, sensitivity is governed by the strong energy dependence of the effective area, but often starts to be limited by background systematics. At mid-energy, with roughly constant effective area, background statistics limits the sensitivity, resulting in a roughly constant $E^2 F_{min}(E)$. At high energy, telescopes are γ-ray rate limited, with $E^2 F_{min}(E) \sim E$. Currently operating systems reach peak sensitivities around 10^{-12} erg cm^{-2}s^{-1} for 50 h of observations, the larger next-generation systems approach 10^{-13} erg cm^{-2}s^{-1}. A special mode are observations at large zenith angles, of 60° and beyond. At these angles, the distance to the shower maximum is increased by factors of a few, and the size of the light pool is increased correspondingly. Effective detection areas can be increased by up to an order of magnitude compared to observations near zenith, at the expense of an increase in energy threshold (e.g. [76,77]) and potentially increased systematic errors.

The first astrophysical source to be convincingly detected using the imaging atmospheric Cherenkov technique was the Crab Nebula, in 1989 [80]. Modern imaging atmospheric Cherenkov telescopes have sensitivity sufficient to detect sources at 1% of the Crab Nebula flux in about 10 hours, can measure the spectrum of the Crab pulsar and the nebula from $\sim$20 GeV to $\sim$100 TeV [76, 81], and can resolve the $\sim$1 arc-min size of the Crab Nebula [82]. Well over 200 TeV γ-ray sources – both galactic and extragalactic – were discovered using IACTs [83]. A significant fraction of the galactic sources were detected by scanning the Galactic plane from the southern hemisphere with the H.E.S.S. telescope array [84]. The CTAO IACT arrays – the first IACT system to be operated as an open observatory – are expected to boost the number of detected sources to 500 or more; see [85] for a discussion of science with CTAO. The first 23 m diameter CTAO-LST is already operational on La Palma (e.g. [86]); the "alpha" configuration of CTAO (Table 36.2) should become operational around 2030. On the same time scale, the LACT telescopes at the LHAASO site will provide a significant step in sensitivity.

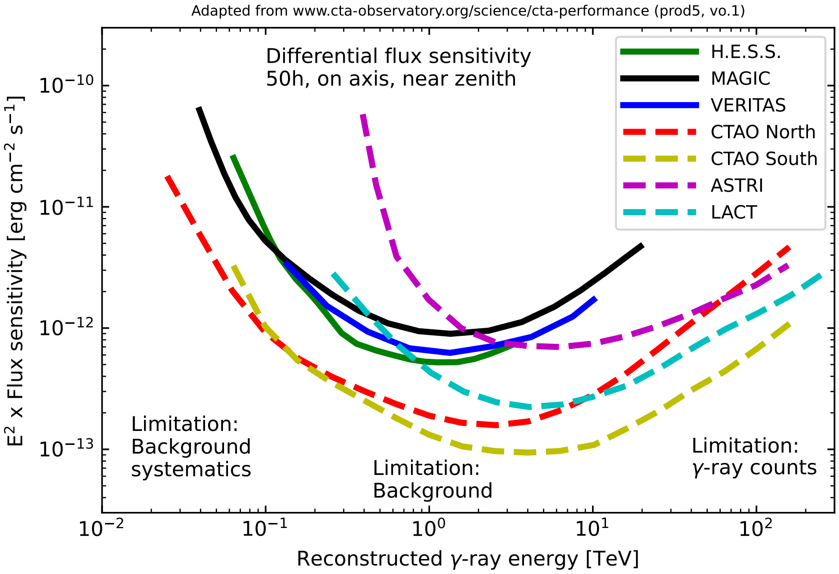

Figure 36.4: Differential flux sensitivity for IACT systems, in operation (solid lines) or under construction (dashed). Adapted from CTAO; sensitivity curves from [78](H.E.S.S.), [51](MAGIC), [79](VERITAS), [54](ASTRI), [57](LACT). Differences at the level of 20-30% may arise from slight differences in definition of sensitivity.

A recent development is the use of IACT arrays for intensity interferometry, using either dedicated photon detectors or special pixels in the camera. The multiple baselines provided by IACT arrays allow imaging of stars on milli-arc-sec scales, and first results are highly promising (e.g. [87–89]).

36.3 Large neutrino detectors

36.3.1 *Deep liquid detectors for rare processes*

Revised October 2025 by J. Cao (IHEP Beijing).

Deep, large detectors for rare processes tend to be multi-purpose with physics reach that includes not only solar, reactor, supernova and atmospheric neutrinos, but also searches for baryon number violation and lepton number violation, searches for exotic particles and beyond-the-standard-model physics, and neutrino and cosmic-ray astrophysics in different energy regimes. The detectors may also serve as targets for long-baseline neutrino beams for neutrino oscillation studies. In general, detector design considerations can be divided into high- and low-energy regimes, for which background and event reconstruction issues differ. The high-energy regime, from about 100 MeV to a few hundred GeV, is relevant for proton decay searches, atmospheric neutrinos and high-energy astrophysical neutrinos. The low-energy regime (a few tens of MeV or less) is relevant for supernova, solar, reactor and geological neutrinos.

Large water Cherenkov and scintillator detectors (see Table 36.3) usually consist of a volume of transparent liquid viewed by photosensors (see Section 35.2); the liquid serves as active target. While some early detectors are segmented into subvolumes individually viewed by photosensors, monolithic detectors usually have better performance and are cost-effective for large volume. A typical detector configuration is shown in Figure 36.5.

A “fiducial volume” is usually defined within the target volume, some distance away from the

Table 36.3: Properties of large detectors for rare processes. If total target mass is divided into modules, the number of modules is indicated in parentheses. Projects with first data expected in 2025 or later are indicated in italics.

Detector	Mass, kton (modules)	PMTs (diameter, cm)	Photocathode Coverage	p.e./MeV	Dates
BUST	0.33, scint (3150)	1/module (15)	segmented	40	1980–
MACRO	0.56, scint (476)	2-4/module (20)	segmented	18	1989–2000
LVD	1, scint (840)	3/module (15)	segmented	15	1992–2023
KamLAND	0.41[*], scint	1325 (43) + 554 (51)[†]	34%	460	2002–
Borexino	0.1[*], scint	2212 (20)	30%	500	2007–2021
CHOOZ	0.005, scint (Gd)	192 (20)	15%	130	1997–1998
Double Chooz	0.017, scint (Gd)(2)	390/detector (25)	13%	200	2011–2017
Daya Bay	0.160, scint (Gd)(8)	192/detector (20)	5.6%[‡]	163	2011–2020
RENO	0.032, scint (Gd)(2)	354/detector (25)	14%	230	2011–2023
SNO+	0.78, scint[§]	9362 (20)	31%[¶]	400–600	2021–
JUNO	18.3[*], scint	17596 (51) + 25587 (8)	77.9%	1780	2025–
IMB-1	3.3[*], H_2O	2048 (12.5)	1%	0.25	1982–1985
IMB-2	3.3[*], H_2O	2048 (20)	4.5%	1.1	1987–1990
Kam I	0.88/0.78[*], H_2O	1000/948 (51)	20%	3.4	1983–1985
Kam II	1.04[*], H_2O	948 (51)	20%	3.4	1986–1990
Kam III	1.04[*], H_2O	948 (51)	20%[‖]	4.3	1990–1995
SK I	22.5[*], H_2O	11146 (51)	40%	6	1996–2001
SK II	22.5[*], H_2O	5182 (51)	19%	3	2002–2005
SK III-V	22.5[*], H_2O	11129 (51)	40%	6	2006–2020
SK-Gd	22.5[*], H_2O (Gd)	11129 (51)	40%	6	2020–
Hyper-K	188[*], H_2O	20000 (51) + 800 (mPMT)	20%	6	2028 (exp.)
SNO	1, D_2O	9438 (20)	31%[¶]	9	1999–2006
DUNE	40[*], Ar (4)	TBD[**]	TBD[**]	TBD[**]	2028 (exp.)[††]

[*] Indicates typical fiducial mass used for data analysis; this may vary by physics topic.
[†] Measurements made before 2003 only considered data from the 43-cm PMTs.
[‡] The effective Daya Bay coverage is 12% with top and bottom reflectors.
[§] SNO+ ran with water fill from May 2017 to July 2019.
[¶] The effective SNO and SNO+ coverage is 54% with light collectors.
[‖] The effective Kamiokande III coverage was 25% with light collectors.
[**] Photodetector technology and coverage varies according to TPC type and is not yet fully determined.
[††] Modules will be constructed in a phased approach.

photosensors, to have relatively uniform detector response and to suppress ambient backgrounds. A nonscintillating buffer is necessary only for liquid scintillator (LS) detectors to shield the active target from natural radioactivities from the photosensors and detector structures. The liquid volume usually requires purification and there may be continuous recirculation of liquid.

Photomultiplier tubes (PMTs) commonly used as photosensors for such large detectors have typical sizes ranging from 20 cm to 51 cm in diameter, quantum efficiencies in the 20–31% range, and time responses at nano-second level. PMTs are usually potted to be water-proof or oil-proof to protect the bases containing high voltage dividers. Protection covers may be needed to avoid chain reaction of implosion. Earth magnetic field can be shielded either for individual PMTs by wrapping

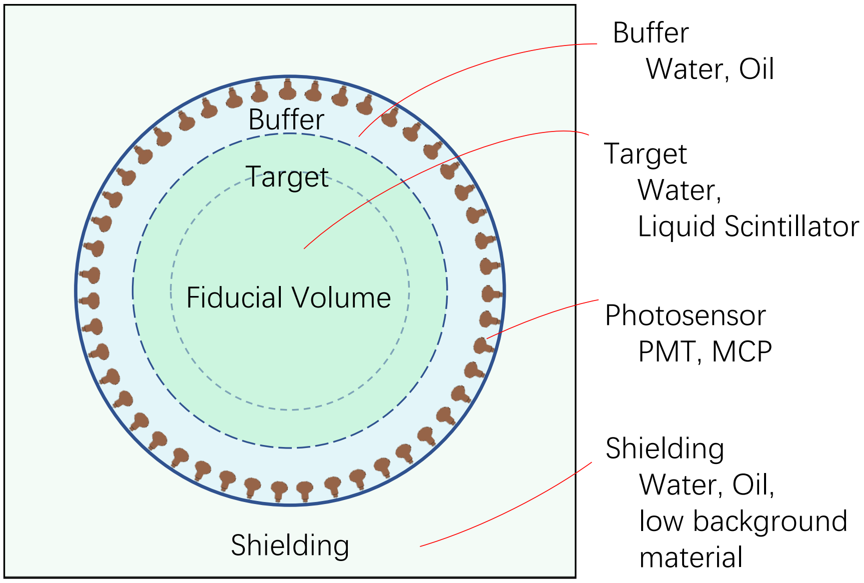

Figure 36.5: Schematic illustration of a typical water Cherenkov or liquid scintillator detector. An array of photosensors view the active target volume to detect the Cherenkov and/or scintillation light. For a liquid scintillator detector, usually there is a nonscintillating buffer between the target and the photosensors. The whole detector is usually surrounded by shielding materials and equipped with muon veto detectors.

high magnetic permeability material or for the whole detector with compensating coils, to diminish the impact to the PMT collection efficiency. Devices to increase light collection, *e.g.*, reflectors or waveshifter plates, may be employed. Silicon Photomultipliers (SiPMs) and Microchannel Plates (MCPs) are new optional photosensors. Comparing with PMTs, SiPMs have higher quantum efficiency but much higher dark noise, and MCPs have faster time response.

Charges and times, sometimes the full waveforms, of photosensors are recorded and digitized. Triggering is usually based on coincidence of hits within a time window comparable to the detector's light-crossing time. For large homogeneous detectors, the event interaction vertex and energy deposition are determined using relative timing and/or charge distribution of photosensors in the detector. Usually, arbitrary light reflection is minimized to understand the light propagation and improve vertex and energy reconstruction. This can be achieved by placing black sheets between photosensors or blackening the inner surface of the detector. Meanwhile, light reflection is usually maximized to increase muon detection efficiency for outer veto detectors.

Because in most cases one is searching for rare events, large detectors are usually sited underground to reduce cosmic-ray-related background (see Chapter 30). The minimum depth required varies according to the physics goals [90]. To shield the cosmogenic backgrounds (for both water and LS detectors) and ambient natural radioactivities (for LS detectors), detectors are usually surrounded by water, oil, or other shielding material and equipped with muon veto detectors.

36.3.1.1 *Liquid scintillator detectors*

Past and current large underground detectors based on hydrocarbon scintillator include BUST, MACRO, LVD, KamLAND, Borexino, SNO+ and JUNO. Experiments at nuclear reactors include CHOOZ, Double CHOOZ, Daya Bay, and RENO. As shown in Figure 36.5, a nonscintillating buffer hosting the photosensors is necessary. A large LS detector usually consists of two or even three concentric liquid layers, separating by concentric thin acrylic vessels or balloons made of nylon transparent to scintillation light.

Organic liquid scintillators (see Section 35.3) for large detectors are chosen for high light yield and attenuation length, good stability, compatibility with other detector materials, high flash point, low toxicity, and low cost. They are made by dissolving a few gram per litre fluor into solvent. The most popular solvents are 1,2,4-trimethylbenzene (pseudocumene) and linear alkylbenzene (LAB). LAB is an ideal choice especially with very good transparency for a gigantic detector. Pseudocumene has a low flash point and is relatively aggressive to detector materials; thus is often diluted with alkane. Xylene is more volatile but has very good pulse shape discrimination power. The most popular fluor is 2,5-diphenyloxazole (PPO). Besides the primary fluor, a secondary fluor, aka waveshifter, is usually added to shift the scintillation light to longer wavelength where the LS is more transparent; thus the light yield increases. The most popular waveshifters include p-bis-(o-methylstyryl)-benzene (bis-MSB) and 1,4-bis(5-phenyl-2-oxazolyl)benzene (POPOP). Antioxidant may be added into LS for long-term stability.

Liquid scintillators have a typical light yield of $\sim 10^4$ photons/MeV. The attenuation length ranges from 5 to 20 meters when measured at ~ 430 nm wavelength. Some solvents such as LAB have strong Rayleigh scattering, which contributes significantly to the attenuation length. The absorption length of LS can be as long as 70 meters. With current highest photocathode coverage 78% and 30% PMT photon detection efficiency (PDE, defined as the peak quantum efficiency times collection efficiency), about 1,780 pe/MeV of energy deposition can be obtained. The energy resolution reaches 3% at 1 MeV [91] and is still dominated by photon statistics. With a typical 20–40% coverage and $\sim 20\%$ PDE, the energy resolution is about $5-7\%/\sqrt{E(\mathrm{MeV})}$. The energy response of LS is not linear and depends on particle types due to ionization quenching. Careful calibration with multiple sources at multiples energy points is needed. Other quenching effects, such as oxygen and temperature, may reduce the light yield at 10% level. Light is emitted with a time response consisting of several exponential components, depending on the solvents and fluors. Usually most light is emitted in tens of nanoseconds. Typical resolution of position reconstruction, using charges and times of PMT hits, is a few tens of cm at ~ 1 MeV.

Radioactive backgrounds from photosensors, detector materials, LS itself, and immediate environment are serious issues for LS detectors. Dedicated detector design, careful selection of materials, purification of the scintillator, and well controlled assembly environment and procedure are essential (see Section 36.6). Radon and Krypton in air as well as Radon decay daughters may impose serious challenges to the experiment. The lower detection threshold of a LS detector is often determined by the ^{14}C content in LS with the 156 keV β-decay endpoint energy. Fiducialization helps to reduce the backgrounds originating from the outer part of the detector. The intrinsic backgrounds from the LS itself have been purified to $< 9.4 \times 10^{-20}$ g/g for ^{238}U and $< 5.7 \times 10^{-19}$ g/g for ^{232}Th [92].

For $\bar{\nu}_e$ detection via inverse beta decay on free protons, $\bar{\nu}_e + p \to n + e^+$, the time coincidence of the prompt positron signal and the delayed neutron capture signal suppresses significantly the radioactive backgrounds. Doping a small fraction of Gadolinium (or other elements with high neutron capture cross section, such as Cadmium and Lithium) in the LS, *e.g.* $\sim 0.1\%$ by mass, the neutron capture time could be reduced from ~ 200 μs to ~ 30 μs. Futhermore, the total gamma energy released from the neutron capture increases from 2.2 MeV to 8 MeV, well above the radioactive background energy thus providing a clean tag for antineutrino. Doping inorganic Gadolinium (as well as other elements) into organic scintillator requires specialized formulation to ensure adequate transparency and stability.

One can also dissolve neutrinoless double beta decay ($0\nu\beta\beta$) isotopes in scintillator. This has been realized by KamLAND-Zen, which deployed a 1.9 m-radius balloon containing enriched Xe dissolved in scintillator inside KamLAND, and ^{130}Te is planned for SNO+.

Liquid scintillator is especially suitable for detection of low-energy events. However, scintillation light emission is nearly isotropic, and therefore directional capabilities are relatively weak. Developing technology such as water-based liquid scintillator with reduced scintillation light yield [93] or liquid scintillator with slow fluors [94] provides the directional capability by separating the Cherenkov light from the scintillation.

36.3.1.2 *Water Cherenkov detectors*

Very large imaging water detectors reconstruct ten-meter-scale Cherenkov rings produced by charged particles (see Section 35.5). The first such large detectors were IMB and Kamiokande. Currently, the only operational detector of this kind is Super-Kamiokande (Super-K, SK), which has a fiducial mass of 22.5 kton and a total mass of 50 kton. Hyper-Kamiokande (Hyper-K) is under construction and will have a fiducial mass of 188 kton and a total mass of 258 kton.

Super-K is instrumented with 11,129 20-inch PMTs of a peak quantum efficiency $\sim 20\%$, corresponding to a photocathode coverage of $\sim 40\%$. Hyper-K will be equipped with at least 20,000 20-inch PMTs and 800 mPMTs, a module about 20-inch in size and assembled with multiple 3-inch PMTs, corresponding to $\sim 20\%$ photocathode coverage. Hyper-K PMTs have a quantum efficiency $\sim 31\%$ and a higher collection efficiency than Super-K, resulting in similar pe yields for the two detectors.

For volumes of this scale, absorption and scattering of Cherenkov light are non-negligible. Attenuation length of the high purity water have been achieved at the order of 100 meters with continuous recirculation and purification. Radon need be carefully stripped from water to reduce the detector noise during both the water production and recirculation. Maintaining a temperature gradient in the detector to avoid water convection helps to further reduce such noise. Given the giant detector size, PMT readout electronics works usually underwater to avoid signal attenuation; thus requires high reliability. Degassing may be a serious issue that causes high voltage breakdown when air in the underwater electronics boxes or cracks in connectors is gradually removed by the degassed pure water. A solution is to regas the pure water with nitrogen [95].

Cherenkov detectors are excellent electromagnetic calorimeters. The number of Cherenkov photons produced by an e/γ is nearly proportional to its kinetic energy, ~ 6 pe/MeV for Super-K. For massive particles, the number of photons produced is also related to the energy, but not linearly. The directionality of Cherenkov light allows individual particle tracks to be reconstructed. Vertex and direction fits are performed using PMT hit charges and times, requiring that the hit pattern be consistent with a Cherenkov ring.

High-energy ($\sim$100 MeV or more) neutrinos from the atmosphere or beams interact with nucleons; for the nucleons bound inside the ^{16}O nucleus, nuclear effects must be considered. Various event topologies, with final-state particles contained, exiting, or entering the detector, can be distinguished by their timing and fit patterns, and by presence or absence of light in a veto. At high energies, the energy resolution is approximately $3\%/\sqrt{E_{\mathrm{vis}}(\mathrm{GeV})}$ for Super-K. The absolute energy scale in this regime can be known to $\sim$ 2–3% using cosmic-ray muon energy deposition, Michel electrons and π^0 from atmospheric neutrino interactions. Typical vertex resolutions for GeV energies are a few tens of cm. Angular resolution for determination of the direction of a charged particle track is a few degrees. For a neutrino interaction, because some final-state particles are usually below Cherenkov threshold, knowledge of direction of the incoming neutrino direction itself is generally worse, depending on neutrino energy.

Multiple particles in an interaction (so long as they are above Cherenkov threshold) may be reconstructed, allowing for the exclusive reconstruction of final states. In searches for proton decay, multiple particles can be kinematically reconstructed to form a decaying nucleon. Particle identification can be done with high reliability with pattern recognition: γ rays and electrons shower, and electrons scatter, which results in fuzzy rings, whereas muons, pions and protons make sharp rings.

In spite of the fairly low light yield, large water Cherenkov detectors may be employed for reconstructing low-energy events, down to *e.g.* $\sim$ 4-5 MeV for Super-K. Using an electron LINAC and/or nuclear sources, approximately 0.5% determination of the absolute energy scale has been achieved at solar neutrino energies. Angular resolution is limited by multiple scattering in this energy regime (25–30°). At these energies, radioactive backgrounds become a dominant issue. In the few to few tens of MeV range, radioactive products of cosmic-ray-muon-induced spallation are troublesome, and are removed by proximity in time and space to preceding muons. Gadolinium doping using $Gd_2(SO_4)_3$ has now been initiated for Super-K to improve selection of low-energy $\bar{\nu}_e$ and other events with accompanying neutrons.

The Sudbury Neutrino Observatory (SNO) detector was the only instance of a large heavy water detector. In addition to an outer 1.7 kton of light water, SNO contained 1 kton of D_2O, giving it unique sensitivity to neutrino neutral current ($\nu_x + d \to \nu_x + p + n$), and charged current ($\nu_e + d \to p + p + e^-$) deuteron breakup reactions. The neutrons were detected in three ways: via capture on deuterons, via capture on dissolved ^{35}Cl, and via specialized ^{3}He counters.

36.3.1.3 *Noble liquid detectors*

Noble liquids scintillate and can be used as the active medium for particle detection. Detectors employing argon and xenon are also used as time-projection chambers (TPCs), either as dual-phase low-energy recoil detectors, or as track-imaging detectors. Noble-liquid detectors with low energy (few to few tens of keV) capability for detecting electronic and nuclear recoils are employed for dark matter and other rare event searches and are described in Sec. 36.4. These detectors can also be employed for some of the same physics (solar neutrino, baryon number violation, astrophysical neutrino transient searches, etc.) as for the other large detectors described here, especially as they approach tens of ton scale and higher (e.g., XLZD, DarkSide-20k, ARGO). Track-imaging time-projection chambers, which are described in detail Section 36.4, have a dynamic range reaching down to the few to few tens of MeV scale, enabling sensitivity to e.g., solar and supernova burst neutrinos. Surface LArTPCs have significant cosmic backgrounds, but may still have sensitivity to astrophysical transients such as supernova burst neutrinos. DUNE will be sufficiently deep to have sensitivity to steady-state low-energy neutrino sources such as solar neutrinos.

36.3.2 *Neutrino telescopes*

Revised March 2026 by U.F. Katz (Erlangen U.) and C. Spiering (DESY, Zeuthen).

The primary goal of neutrino telescopes (NTs) is the detection of astrophysical neutrinos, in particular those which are expected to accompany the production of high-energy cosmic rays in astrophysical accelerators. NTs in addition address a variety of other fundamental physics issues like the indirect search for dark matter, studies of neutrino oscillations, searches for exotic particles like magnetic monopoles or study of cosmic rays and their interactions [96–98]. Electromagnetic radio frequency detectors for high energy neutrinos are discussed in "Radio emission from (ultra-) high energy particle showers" section 36.3.3.

NTs are large-volume arrays of “optical modules” (OMs) installed in open transparent media like water or ice, at depths that completely block the daylight. The OMs are sensitive to individual photons of the Cherenkov light induced by charged secondary particles produced in reactions of high-energy neutrinos in or around the instrumented volume. The time of photon-induced signals (“hits”) is registered with a precision of a few nanoseconds. The neutrino energy, E_ν, and direction can be reconstructed from the hit pattern recorded. NTs typically target an energy range $E_\nu \gtrsim 100\,\mathrm{GeV}$; sensitivity to lower energies is achieved in dedicated setups with denser instrumentation.

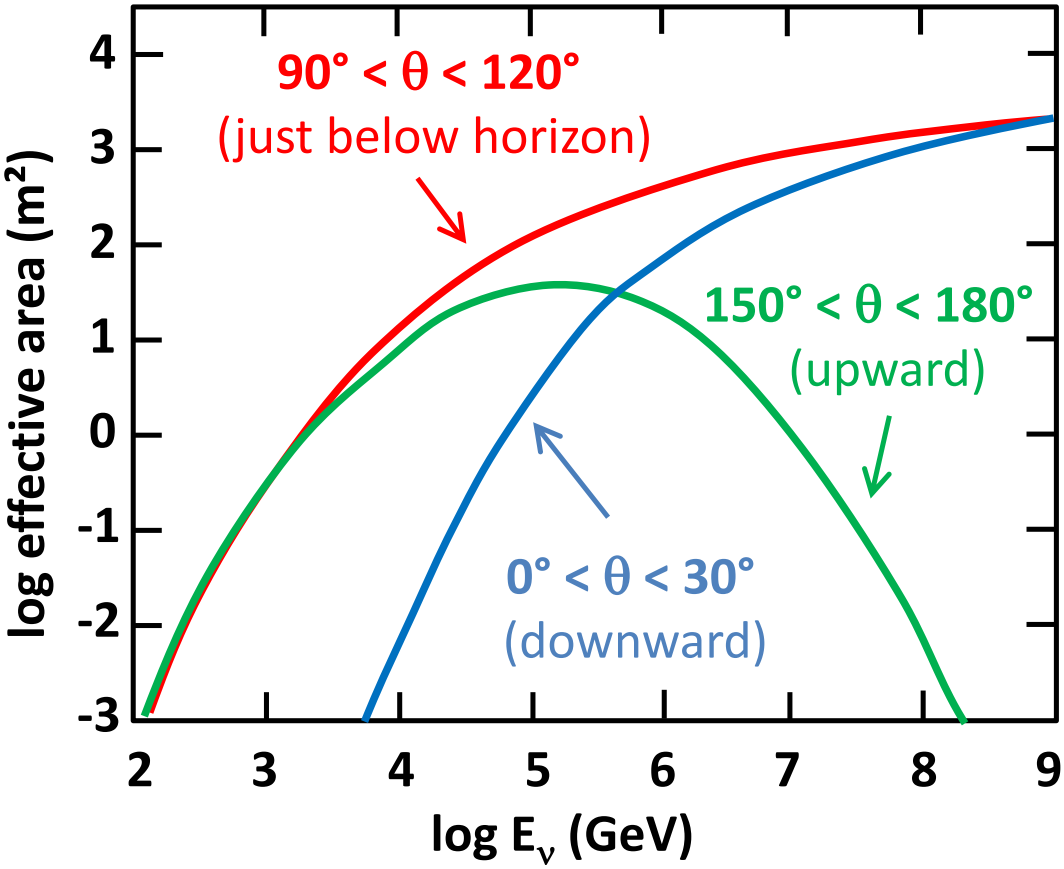

Figure 36.6: Average over the effective ν_μ and $\overline{\nu}_\mu$ areas for IceCube as an example of a cubic-kilometre NT, as a function of neutrino energy for three intervals of the zenith angle θ. The values shown here correspond to a specific event selection for point source searches.

In detecting cosmic neutrinos, three sources of backgrounds have to be considered: (i) *atmospheric neutrinos* from cosmic-ray interactions in the atmosphere, which can be separated from cosmic neutrinos on a statistical basis, or, for down-going neutrinos, by vetoing accompanying muons; (ii) down-going punch-through *atmospheric muons* from cosmic-ray interactions, which are suppressed by several orders of magnitude with respect to the ground level due to the large detector depths and can be further reduced by selecting upward-going or high-energy neutrinos or by self-veto methods; (iii) random backgrounds due to photomultiplier (PMT) dark counts, ^{40}K decays (mainly in sea water) or bioluminescence (only water). Atmospheric neutrinos and muons allow for investigating neutrino oscillations and cosmic ray anisotropies, respectively. Since 2012, it has become obvious that a precise measurement of the energy-zenith-distribution of atmospheric neutrinos in the energy range from a few to about 100 GeV may allow for determining the neutrino mass hierarchy by exploiting matter-induced oscillation effects in the Earth [99, 100].

Neutrinos can interact with target nucleons N through charged current ($\overset{(-)}{\nu}_\ell N \to \ell^\mp X$, CC) or neutral current ($\overset{(-)}{\nu}_\ell N \to \overset{(-)}{\nu}_\ell X$, NC) processes. A CC reaction of a $\overset{(-)}{\nu}_\mu$ produces a muon track and a hadronic particle cascade, whereas all NC reactions and CC reactions of $\overset{(-)}{\nu}_e$ produce particle cascades only. CC interactions of $\overset{(-)}{\nu}_\tau$ can have either signature, depending on the τ decay mode. Of particular interest is the so-called double-bang signature, where the τ decays sufficiently far away from the primary interaction to create a second, distinguishable cascade (typically at PeV energies and above). In most astrophysical models, neutrinos are expected to be produced through the $\pi/K \to \mu \to e$ decay chain, *i.e.*, with a flavour ratio $\nu_e : \nu_\mu : \nu_\tau \approx 1 : 2 : 0$. For sources outside the solar system, neutrino oscillations turn this ratio to $\nu_e : \nu_\mu : \nu_\tau \approx 1 : 1 : 1$ upon arrival on Earth.

The total neutrino-nucleon cross section is about $10^{-34}\,\text{cm}^2$ at $E_\nu = 20\,\text{TeV}$ and rises roughly linearly with E_ν below this energy and as $E_\nu^{0.3-0.5}$ above, flattening out towards high energies. The CC:NC cross-section ratio is about 2:1. At energies above several TeV, neutrino absorption in the Earth becomes noticeable; for vertically upward-moving neutrinos (zenith angle $\theta = 180^\circ$), the survival probability is $74\,(27, < 2)\%$ for $10\,(100, 1000)$ TeV. The energy transferred to the final-state lepton varies between 0 and 100% of E_ν, with a mean of 50% (65%) for neutrinos (antineutrinos) at 100 GeV and 75% for both neutrinos and antineutrinos at 10 PeV.

The final-state lepton follows the initial (anti)neutrino direction with an average mismatch angle of about $\langle\phi_{\nu\ell}\rangle \approx 1^\circ/(E_\nu/\text{TeV})^{0.55}$, with a steeper decrease beyond 10 TeV, reaching 0.005° at 1 PeV [101]. These values indicate the intrinsic kinematic limit to the angular resolution of NTs. For CC $\overset{(-)}{\nu}_\mu$ reactions at energies above about 10 TeV, the angular resolution is dominated by the muon reconstruction accuracy of a few times 0.1° at most. For muon energies $E_\mu \gtrsim 1\,\text{TeV}$, the increasing light emission due to radiative processes allows for reconstructing E_μ from the measured Cherenkov light intensity with an accuracy of $\sigma(\log E_\mu) \approx 0.3$; at lower energies, E_μ can be estimated from the length of the muon track if it is contained in the detector. These properties make CC $\overset{(-)}{\nu}_\mu$ reactions the prime channel for the identification of individual astrophysical neutrino sources.

Hadronic and electromagnetic particle cascades at the relevant energies are 5–20 m long, *i.e.*, short compared to typical OM spacings. The total amount of Cherenkov light provides a direct measurement of the cascade energy with an accuracy of about 20% at energies above 10 TeV and 10% beyond 100 TeV for events contained in the instrumented volume. Except for double-bang events, the neutrino flavour and reaction mechanism can, however, be determined on a statistical basis at best, and neutrinos from NC reactions or τ decays may carry away significant "invisible" energy. Above 100 TeV, the average directional reconstruction accuracy of cascades is better than 10 (2) degrees in polar ice (sea water), the difference being due to the inhomogeneity of the ice and stronger light scattering in ice. These features, together with the small background of atmospheric $\overset{(-)}{\nu}_e$ and $\overset{(-)}{\nu}_\tau$ events, makes the cascade channel particularly interesting for searches for a diffuse, high-energy excess of extraterrestrial over atmospheric neutrinos. Cascade events can also be used to complement the muon channel in searches for point sources or transient signals, albeit with inferior angular accuracy compared to muon tracks.

The detection efficiency of a NT is quantified by its effective area, *e.g.*, the fictitious area for which the full incoming neutrino flux would be recorded (see Figure 36.6). The increase with E_ν is due to the rise of neutrino cross section and muon range, while neutrino absorption in the Earth causes the decrease at large θ for large E_ν. Identification of downward-going neutrinos requires stringent event selection to suppress atmospheric muons, hence the cut-off towards low E_ν at low θ. Due to the small cross section, the effective area is many orders of magnitude smaller than the geometrical dimension of the detector; a $\overset{(-)}{\nu}_\mu$ with 1 TeV can, *e.g.*, be detected with a probability of the order 10^{-6} if the NT is on its path.

Due to the long muon range, CC interactions of up-going $\overset{(-)}{\nu}_\mu$ can be detected from far outside the instrumented volume. This method also works for horizontal neutrinos up to about 10° above the horizon (depth dependent), where the background from atmospheric muons become prohibitive. Alternatively, one can select events that start inside the instrumented volume and thus remove incoming muons that generate early hits in the outer layers of the detector. Such a veto-based event selection is sensitive to neutrinos of all flavours from all directions, albeit with a reduced efficiency since a part of the instrumented volume is sacrificed for the veto. Such a muon veto, or vetoing events with a coincident signal in the surface array, also rejects down-going atmospheric neutrinos that are accompanied by muons from the same air shower and thus reduces the atmospheric-neutrino background. Actually, the breakthrough in detecting high-energy cosmic neutrinos was first achieved with this technique.

Note that the fields of view of NTs at the South Pole and in the Northern hemisphere are complementary for each reaction channel and neutrino energy.

36.3.2.1 *The Projects*

Table 36.4 lists past, present and future neutrino telescope projects and their main parameters.

Table 36.4: Past, present and future NT projects and their main parameters. The milestone years give the times of project start, of first data taking with partial configurations, of detector completion, and of project termination. Projects with first data expected past 2026 are indicated in italics. The size refers to the largest instrumented volume reached during the project development. The status of projects under construction is reported at the time of writing. See [98] for references to the different projects where unspecified.

Experiment	Milestones	Location	Size (km^3)	Remarks
DUMAND	1978/–/–/1995	Pacific Ocean		Terminated due to technical/funding problems
NT-200	1980/1993/1998/2015	Lake Baikal	10^{-4}	First proof of principle
GVD [102]	2012/2015/–/–	Lake Baikal	ca. 1	High-energy ν astronomy data taking with 14 clusters
AMANDA	1990/1996/2000/2009	South Pole	0.015	First deep-ice NT
IceCube [103]	2001/2005/2010/–	South Pole	1.0	First km^3-sized detector 6 additional strings installed 2025/26 (IceCube Upgrade)
IceCube-Gen2 [104]	2014/–/–/–	South Pole	5–10	Planned future extension of IceCube covering low and high energies, a surface array and radio detection
NESTOR	1991/–/–/2012	Med. Sea		2004 data taking with prototype
NEMO	1998/–/–/–	Med. Sea		R&D project, prototype tests
ANTARES	1997/2006/2008/2022	Med. Sea	0.010	First deep-sea NT
KM3NeT/ARCA [100]	2013/2021/–/–	Med. Sea	ca. 1	High-energy configuration for neutrino astronomy. Under construction, data taking with 45 strings
KM3NeT/ORCA [100]	2014/2020/–/–	Med. Sea	0.007	Low-energy configuration for neutrino mass hierarchy. Under construction, data taking with 33 strings
KM3NeT Phase 3	2013/–/–/–	Med. Sea	ca. 3	Possible future extension, 6 ARCA blocks + ORCA
P-ONE [105]	2018/–/–/–	Pacific Ocean	$\mathcal{O}(1)$	Planned future NT, R&D phase
TRIDENT [106]	2021/–/–/–	South China Sea	$\mathcal{O}(10)$	Planned future NT, R&D phase
HUNT [107]	2022/–/–/–	South China Sea or Lake Baikal	$\mathcal{O}(30)$	Planned future NT, R&D phase Prototype tests in Lake Baikal
NEON [108]	2023/–/–/–	South China Sea	$\mathcal{O}(10)$	Planned future NT, R&D phase

36.3.2.2 *Properties of media*

The efficiency and quality of event reconstruction depend strongly on the optical properties (absorption and scattering length, intrinsic optical activity) of the medium in the spectral range of bialkali photocathodes (300–550 nm). Large absorption lengths result in a better light collection, large scattering lengths in superior angular resolution. Deep-sea sites typically have effective scattering lengths of > 100 m and, at their peak transparency around 450 nm, absorption lengths of 50–65 m. The absorption length for Lake Baikal is 22–24 m. The properties of South Polar ice vary strongly with depth; at the peak transparency wave length (400 nm), the scattering length is between 5 and 75 m and the absorption length between 15 and 250 m, with the best values in the depth region 2200–2450 m and the worst ones in the layer 1950–2100 m.

Noise rates measured by PMTs with a diameter of 25 cm in deep polar ice are about 0.5 kHz per PMT and almost entirely due to radioactivity in the OM components. The corresponding rates in sea water are typically 60 kHz, mostly due to ^{40}K decays. Bioluminescence activity can locally cause rates on the MHz scale for seconds; the frequency and intensity of such "bursts" depends strongly on the sea current, the season, the geographic location, and the geometry of the detector elements. Experience from ANTARES shows that these backgrounds are manageable without a major loss of efficiency or experimental resolution.

36.3.2.3 *Technical realisation*

Optical modules (OMs) and PMTs: An OM is a pressure-tight glass sphere housing one or several PMTs with a time resolution in the nanosecond range, and in most cases also electronics for control, high-voltage generation, operation of calibration LEDs, time synchronisation and signal digitisation.

Hybrid PMTs with 37 cm diameter have been used for NT-200, conventional hemispheric PMTs with 20 cm diameter for AMANDA and with 25 cm diameter for ANTARES, IceCube and Baikal-GVD. A novel concept has been chosen for KM3NeT. Each OM (43 cm) is equipped with 31 PMTs (7.5 cm), plus control, calibration and digitisation electronics. Advantages are that (i) the overall photocathode area exceeds that of a 25 cm PMT by more than a factor of 3; (ii) the individual readout of the PMTs results in a very good separation between one- and two-photoelectron signals which is essential for online data filtering and random background suppression; (iii) the hit pattern on an OM provides directional information; (iv) no mu-metal shielding against the Earth magnetic field is required. A multi-PMT optical module is also one of the two selected options for the IceCube Upgrade (see below). It contains 24 3-inch PMTs in a smaller-diameter glass vessel matching the maximal size of the ice holes. The second OM type for the Upgrade features two 8-inch PMTs (one upward- and one downward-pointing). See [104] for details. Figure 36.7 shows the OM designs currently used in IceCube and KM3NeT.

Readout and data filtering: In current NTs the PMT data are digitised in situ: for ANTARES and Baikal-GVD in special electronics containers close to the OMs, for IceCube and KM3NeT inside the OMs. For IceCube, data are transmitted via electrical cables of up to 3.3 km length, depending on the location of the strings and the depth of the OMs; for ANTARES, KM3NeT and Baikal-GVD optical fibre connections have been chosen (several 10 km for the first two and 4 km for GVD).

The full digitised waveforms of the IceCube OMs are transmitted to the surface for pulses appearing in local coincidences on a string; for other pulses, only time and charge information is provided. For ANTARES (time and charge) and KM3NeT (time and time over threshold), all PMT signals above an adjustable threshold are sent to shore.

The data are subsequently processed on online computer farms, where multiplicity- and topology-driven filter algorithms are applied to select event candidates. The filter output data rate is about 10 GByte/day for ANTARES and of the order 1 TByte/day for IceCube (100 GByte/day transferred via satellite) and KM3NeT.

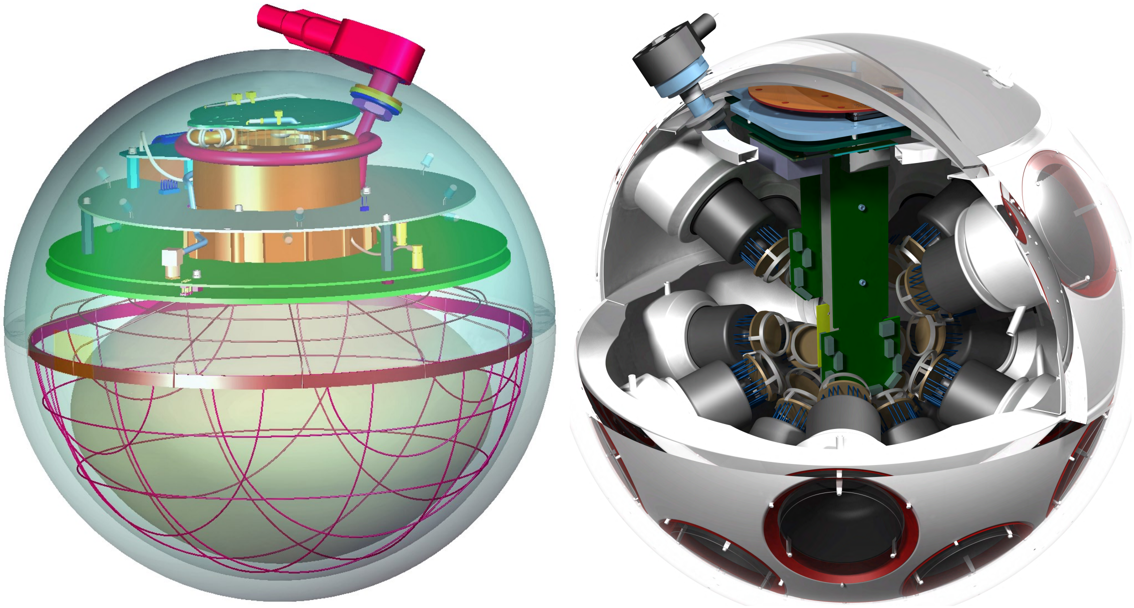

Figure 36.7: Schematic views of the digital OMs of IceCube (left) and KM3NeT (right).

Calibration: For efficient event recognition and reconstruction, the OM timing must be synchronised at the few-nanosecond level and the OM positions and orientations must be known to a few 10 cm and a few degrees, respectively. Time calibration is achieved by sending synchronisation signals to the OM electronics and also by light calibration signals emitted in situ at known times by LED or laser flashers (ANTARES, KM3NeT). Precise position calibration is achieved by measuring the travel time of light calibration signals sent from OM to OM (IceCube) or acoustic signals sent from transducers at the sea floor to receivers on the detector strings (ANTARES, KM3NeT, Baikal-GVD). Absolute pointing and angular resolution can be determined by measuring the "shadow of the moon" (*i.e.*, the directional depletion of muons generated in cosmic-ray interactions). IceCube and ANTARES have both shown that they have angular resolution below 1°, confirming MC calculations which indicate a precision of $\approx 0.5^\circ$ for energies above 10 TeV. For KM3NeT, simulations indicate that sub-degree precision in the absolute pointing can be reached; for ORCA, 0.5° accuracy has been demonstrated..

Detector configurations: IceCube [103] (see Figure 36.8) consists of 5160 Digital OMs (DOMs) installed on 86 strings at depths of 1450 to 2450 m in the Antarctic ice; except for the DeepCore region, string distances are 125 m and vertical distances between OMs 17 m. 324 further DOMs are installed in IceTop, an array of detector stations on the ice surface above the strings. DeepCore is a high-density sub-array at large depths (*i.e.*, in the best ice layer) at the centre of IceCube.

The NT200 detector in Lake Baikal at a depth of 1100 m consisted of 8 strings attached to an umbrella-like frame, with 12 pairs of OMs per string. The diameter of the instrumented volume was 42 m, its height 70 m. Meanwhile, at the time of writing, the Baikal collaboration has installed and is operating the first 14 clusters of a future cubic-kilometre array, GVD [102]. It will consist of 20 clusters, each with 288 OMs at 8 strings, plus several single strings between the clusters; its completion is scheduled for 2028.

The operation of ANTARES (see [98, 109] and references therein) was terminated in 2022. It comprised 12 strings with lateral distances of 60–70 m, each carrying 25 triplets of OMs at vertical distances of 14.5 m, located at depths of 2.1–2.4 km, starting 100 m above the sea floor. An additional string held devices for calibration and environmental monitoring. A system to investigate

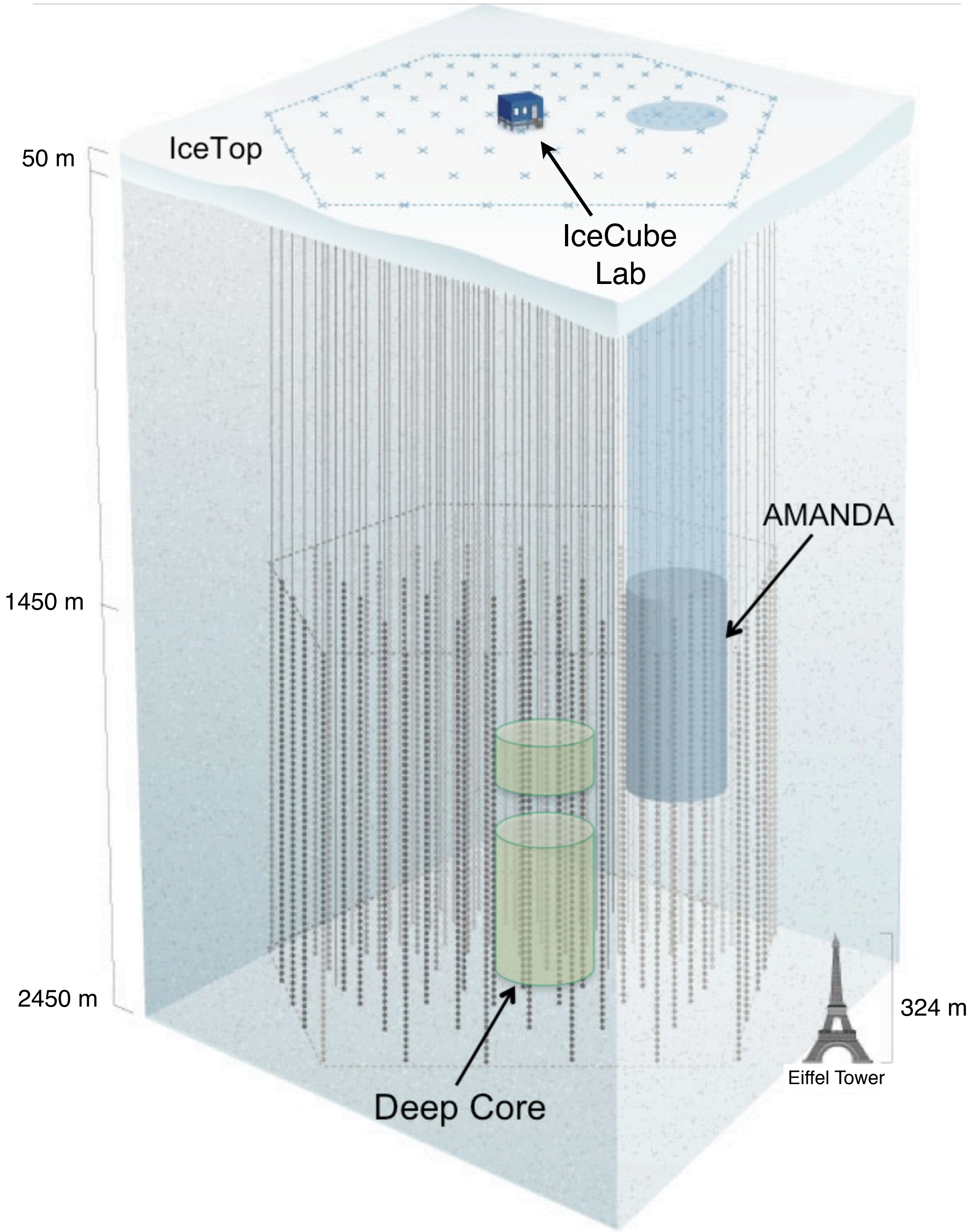

Figure 36.8: Schematic view of the IceCube neutrino observatory comprising the deep-ice detector including its nested dense part DeepCore, and the surface air shower array IceTop. Six strings of the IceCube Upgrade are installed in the DeepCore volume. The IceCube Lab houses data acquisition electronics and the computer farm for online processing. Operation of AMANDA was terminated in 2009.

the feasibility of acoustic neutrino detection was also implemented.

KM3NeT will consist of building blocks of 115 strings each, with 18 OMs per string. Operation of the first strings deployed has successfully verified the KM3NeT technology and sensitivity. In the upcoming phase of its staged implementation, KM3NeT aims at two building blocks for neutrino astronomy, with vertical distances between OMs of 36 m and a lateral distance between adjacent strings of 90 m (ARCA, for *Astroparticle Research with Cosmics in the Abyss*) and at one block for the measurement of the neutrino mass hierarchy, with vertical distances between OMs of 9 m and a lateral distance between adjacent strings of about 20 m (ORCA, for *Oscillation Research with Cosmics in the Abyss*) [100]. The installation of ARCA near Capo Passero, East of Sicily (depth 3440 m) and of ORCA near Toulon (depth 2450 m) is ongoing and as of now (March 2026) 45/33 strings have been deployed for ARCA/ORCA and are continuously taking data. Completion of the full ARCA and ORCA arrays is planned for 2030.

P-ONE (*Pacific Ocean Neutrino Experiment*) [105] is a new initiative in its R&D phase, envisaging a large NT in the Pacific Ocean off the Canadian coast. It is intended to use an existing deep-sea cable infrastructure and to optimise the sensitivity for horizontal neutrinos with energies beyond about 100 TeV.

Three Chinese collaborations are currently working towards projects on the 10 km^3 scale. TRIDENT (*Tropical Deep-Sea Neutrino Telescop*) is a proposed neutrino telescope in the South China Sea with an instrumented volume of 7.5 km^3. R&D and site exploration efforts are ongoing and a pathfinder (TRIDENT Phase-1) is planned to be commissioned around 2026 [110]. HUNT (*High-energy Underwater Neutrino Telescope*) aims at an instrumented volume of 30 km^3, either in the South China Sea or in Lake Baikal [107]. NEON (*NEutrino Observatory in the Nahnhai*) envisages another detector of 10 km^3 in the South China Sea [108]. Whether there will be a process convergence among these three projects appears open at present.

36.3.2.4 *Results*

See Sect. 30.4 for a summary of the results from neutrino telescopes.

36.3.2.5 *Plans beyond 2025*

The IceCube Upgrade project serves to create a very densely instrumented region by deploying additional strings in the DeepCore volume. Main objectives are to inclease the low-energy sensitivity, to improve the calibration of ice properties and thus also the archival data, and to test new technologies. In the Antarctic summer season 2025/26, six strings for the Upgrade have been deployed and are currently in their commissioning phase.

Within the future IceCube-Gen2 project, it is planned to extend the sensitivity of IceCube towards higher energies by installing a large-volume extension, combined with a radio array for highest-energy neutrinos and a surface array providing also a powerful veto against atmospheric events [104].

More information on the future extensions of GVD and KM3NeT and on P-ONE and the Chinese projects TRIDENT, HUNT and NEON are given above and in Table 36.4.

36.3.3 *Radio emission from (ultra-)high energy particle showers*

Revised March 2026 by S.R. Klein (NSD LBNL; UC Berkeley) and A. Nelles (DESY, Zeuthen; Erlangen U.).

Coherent radio-frequency (RF) electromagnetic radiation is an attractive signature to search for particle cascades produced by interactions of high-energy particles. RF signatures have been used to study both cosmic-ray air showers and to search for neutrino-induced showers. This article will discuss the radio signal generation in neutrino-induced showers. Radio signals from cosmic rays are discussed elsewhere [111,112]. The density of the medium (i.e. ice, air, lunar regolith, salt) determines how rapidly a shower develops. This, in turn, affects the radio emission mechanisms. In dense media, radio Cherenkov radiation dominates, while in air, geomagnetic radiation is dominant.

At lower energies, incoherent optical Cherenkov radiation is frequently used, as discussed in

"Neutrino telescopes" section 36.3.2. This article uses the general definitions and properties of neutrino telescopes as described in 36.3.2.

36.3.3.1 *Signal generation and its characteristics*

As discussed in the "Passage of Particles Through Matter" review Sec. 34 the electromagnetic component of a high energy shower gives rise to radio emission. The signal generation depends on the particle energy and the medium; the type of primary particle is unimportant. The medium must be non-conducting and transparent at RF frequencies. The shower develops over a length scale given by the radiation length X_0, which is much larger for air than for solids.

Coherent radio Cherenkov-like emission occurs because the shower contains more electrons than positrons. The coherent radio Cherenov emission, also known as Askaryan effect comes from the net current due to this excess [113–115].

In air, during propagation through the geomagnetic field, the relative motion of electrons and positrons is affected, which leads to a varying transverse current, usually referred to as the geomagnetic effect [111]. All effects may be described more generally as being due to radiation from a time-varying net charge [116]. Their relative importance is governed by the density of the medium, as the electric field of the Askaryan component scales as the net charge excess, and a lower density allows the geomagnetic effect to gain importance. Thus, in solid materials the emission from the Askaryan effect dominates, but it is a $< 20\%$ correction in air showers.

The net charge excess comes at the tail end of the shower, when the particles are mostly low-energy (< 100 MeV). There, positrons in the bean can annihilate on atomic electrons and inverse Compton scattering can accelerate atomic electrons into the shower. Even initially hadronic showers will have a low-energy tail that largely consists of $e^{\pm}$ and photons.

Coherent radiation is possible at wavelengths longer than the instantaneous thickness of the shower along an observer's line of sight. Since air showers have a larger extent than showers in solid media, their coherent radiation appears at lower frequencies [117]. If the density get too low, e.g. in very horizontal air showers, coherence is lost [118].

High-frequency radiation is concentrated around the Cherenkov angle θ_C. Viewed directly on the Cherenkov cone, the electric field strength, ϵ_{Ch} at a frequency f from an electromagnetic shower from a ν_e with energy E_ν in ice may be roughly parameterized as [119, 120]

$$\epsilon_{\mathrm{Ch}}(V/\mathrm{mMHz}) = 2.53 \times 10^{-7} \frac{E_\nu}{1\mathrm{TeV}} \frac{f}{f_c} \left[\frac{1}{1 + (f/f_c)^{1.44}} \right]. \tag{36.3}$$

The electric field strength increases linearly with frequency, up to a cut-off frequency f_c, which is set by the transverse size of the shower [121, 122]. The maximum wavelength c/f_c is roughly the Molière radius divided by $\cos(\theta_C)$ where θ_C is the Cherenkov angle. The cutoff frequencies depend on the density (which affects the Molière radius). They are about 1 GHz in ice, about 3 GHz in the lunar regolith, and below 100 MHz in air, except exactly on the Cherenkov angle, where all frequencies are coherent by definition.

Near f_c, radiation is narrowly concentrated around θ_C [121, 122]. At lower frequencies, the limited length of the emitting region leads to a broadening in emission angle around the Cherenkov cone. Away from θ_C, the electric field from Eq. (36.3) is reduced by [119],

$$\frac{\epsilon}{\epsilon_{\mathrm{Ch}}} = \exp\left(-\frac{1}{2} \frac{(\theta - \theta_C)^2}{(2.2^\circ \times [1\mathrm{GHz}/f])^2} \right). \tag{36.4}$$

The angular distribution of the signal around θ_C can be parameterized by a Gaussian peak modulated by a $\sin\theta$. In both ice and the lunar regolith, θ_C is about 56°, in air only 1°. Close to θ_C, the 1 GHz maximum frequency in ice/regolith leads to a generated pulse width of ≈ 1 ns.

These equations are appropriate for ice. More general parameterizations can be found in [120, 123].

More accurate calculations of the predicted radio signal, in particular air showers are not easily parameterized, but require detailed Monte Carlo simulations. For air showers, these are built on microscopic air shower simulations, calculate the emission from all individual particles in the shower development and add them for different observer positions [111]. For neutrinos, most approaches calculate (directly or from a parameterization) the Askaryan signal from a shower profile. The signal is then propagated through the medium and into an antenna model [120].

At energies above 10^{16} eV in ice, the Landau-Pomeranchuk-Migdal effect lengthens electromagnetic showers, by reducing the cross-sections for bremsstrahlung and pair production [124]. The lengthening of the shower leads to a narrowing of the radio emission around the Cherenkov cone, and a reduction in high-frequency emission away from the cone [120]. At higher energies, this leads to two separate components of the Askaryan radiation from a neutrino interaction: an un-altered component from the hadronic portion of the shower and an angularly narrowed component from the LPM-lengthened electromagnetic shower. The width of the narrowed component scales as $E_\nu^{1/3}$. If these two components can be observed separately, they could, in principle, be combined to determine the inelasticity of the neutrino interaction [125], allowing for improved measurements of low$-x$ parton distributions and searches for beyond-standard-model interactions.

Similarly, energetic outgoing $\mu^\pm$ and $\tau^\pm$ from neutrino interactions dominantly lose energy via stochastic pair production and photonuclear interactions. These secondary particles will produce electromagnetic showers that can be detected by radio detectors, if they are above threshold energy. This will enable multiple detections of the same particle track and thus present interesting reconstruction opportunities and flavor sensitivity [126].

At still higher energies, above 10^{20} eV, the LPM effect strengthens, and the electromagnetic shower splits into multiple subshowers with significant separation. When these separations become large enough, the subshowers will effectively become independent radiators, with the total emission showing substantial event-by-event variation, depending on the division into subshowers [124]. Because of this, many experiments that study higher energy (well above 10^{20} eV) neutrinos focus on the hadronic shower from the struck nucleus. This contains an average of only about 20% of the energy, but with fewer large fluctuations [127].

36.3.3.2 *Energy regime of radio detectors*

In the coherent regime, the electric field amplitude is linearly proportional to the shower energy. Since the signal is a radio wave, the field amplitude decreases as $1/R$, plus potential absorption in the intervening medium, while the energy fluence decreases as $1/R^2$, again, plus potential absorption. The detection threshold depends on the distance to the antenna and the bandwidth and noise characteristics of the antenna and detector. For an antenna located in the detection medium, at a distance of 1 km the typical threshold is around 10^{17} eV. For stand-off (remote sensing) detectors, the threshold rises roughly linearly with the distance. These thresholds can be reduced by using directional antennas and/or combining the signals from multiple antennas using beam-forming techniques.

RF detectors are used to search for energetic neutrinos from three types of sources: astrophysical objects (*i.e.* extending measurements of the neutrino energy spectrum observed at TeV to PeV energies upward in energy), cosmogenic neutrinos associated with cosmic-ray-cosmic microwave background radiation (CMBR) interactions, and neutrinos from beyond-standard-model physics. These three types are very roughly associated with energies below 10^{18} eV, the energy range 10^{18} to 10^{20} eV, and above 10^{20} eV, albeit with considerable overlap.

Cosmogenic neutrinos are produced when ultra-high energy (UHE) protons with energy $E \gtrsim 5\times$

10^{19} eV interact with photons from the CMBR, infrared light from old stars, and other extragalactic background light. These protons are excited to a Δ^+ resonance which may decay via $\Delta^+ \rightarrow n\pi^+$, leading to neutrinos with energies above 10^{18} eV [128,129]. The cosmogenic neutrino signal depends heavily on the fraction of UHE cosmic-rays that are protons. For a 100% proton composition (strongly disfavored by most data [130]), observing a cosmogenic neutrino signal of at least a few events per year requires a solid or liquid detector with an active volume of about 100 km^3 [131].

To reach the effective volumes necessary to observe the expected low fluxes of UHE neutrinos, common, naturally occurring, non-conducting solid (or potentially liquid) media, with a long absorption length for radio waves are needed. Optical Cherenkov detectors are limited by short ($<$ 100 m) attenuation lengths [132] so would require a prohibitively expensive number of sensors. The radio detection technique has been used to detect air showers, targeting neutrinos as well as cosmic rays, and to search for neutrino showers in ice, salt domes and the lunar regolith.

36.3.3.3 *Reconstruction of particle energy and direction and background suppression*

Since radio detectors view the interaction from afar, the reconstruction techniques differ from optical neutrino telescopes.

Radio detection is a calorimetric measurement, thus provides good energy estimates of the shower energy. The energy fluence (time-integrated pulse power) of the signal scales quadratically with shower energy. It also depends on the distance to the shower, through potential attenuation losses and the usual $1/R$ loss in electric field amplitude. The arrival times in antennas and a spherical wave approximation can be used to determine the interaction vertex, although some uncertainty due to the viewing angle with respect to the Cherenkov angle may remain, if not corrected for by using the frequency information. If the radio signal travels through media where the index of refraction varies (like the firn of glacial ice), then ray-tracing techniques may be required to follow the signal back to the interaction point. For buried antennas, the bending of the signal trajectories due to the depth-dependent index of refraction creates an opportunity. For some geometries, there are two paths to the detector: a ‘direct’ path, with minor bending, and a second where the signal is bent beyond horizontal, bouncing off the surface before reaching the antenna. By measuring the time difference between the two paths, the distance to the interaction vertex may be determined; this greatly simplifies the energy determination [133, 134]. For most neutrino interactions (except for ν_e charged-current interactions), the shower energy is less than the neutrino energy. The uncertainty on the interaction inelasticity is a major contributor to the uncertainty in the neutrino energy, along with uncertainties on the distance between the antenna(s) and the interaction vertex [135].

Reconstruction of the neutrino arrival direction depends on several aspects of the signal and on a good understanding of the properties of the medium. First, the direction from the antenna to the interaction site must be determined. This can be done by using the relative timing from separated antennas, or using beam-forming techniques with multi-element arrays. For air showers, the signal arrival direction is (almost) equal to the particle arrival direction, with corrections being obtainable by fitting a hyperbolic wavefront [111, 112].

For showers in solid/liquid media, the arrival direction with respect to the interaction point - antenna vector is determined from two additional angles. The frequency spectrum can be used to determine the angle between signal arrival direction and Cherenkov cone according to Eq. (36.4). The second angle can be determined from the polarization of the signal. The radio signal is produced with a linear polarization in the plane containing both the particle direction and the radio wave direction. These two angles can be combined to determine the direction, subject to a (usually) four-fold ambiguity, due to uncertainty as to whether the antenna is inside or outside the Cherenkov cone, and because the particle direction can be flipped 180° without affecting the observed signal [136]. Often, some of these solutions can be rejected because they correspond to long path lengths through the Moon or the Earth, where the neutrino would be absorbed. Spectral information is crucial for the reconstruction and background rejection. However, large bandwidth antennas typically disperse (i.e. broaden) the pulses. As long as the dispersion can be compensated for in the trigger and backgrounds controlled, a large bandwidth detector is the most sensitive.

All radio experiments must contend with background. Common sources are anthropogenic noise, antenna/preamp noise, charge generated by blowing snow, lightning, and, at low frequencies, radiation from the Milky Way. While narrowband noise impacts triggering and contaminates signal quality, impulsive backgrounds could mimic a signal. One of the major issues for radio-detection experiments is anthropogenic noise. Most anthropogenic noise has distinctive characteristics (such as being narrow-band, and coming from near the horizon) which makes it possible to reject during data analysis, via narrow-band filters and other techniques. However, these factors pose a challenge for triggering on the radio signal and reduce data purity. This is even an issue in Antarctica, where communication radios and passing satellites can mimic showers, at least at the trigger level. The need to limit anthropogenic noise has led most experimental groups to select remote locations for their detectors. Still, experiments need to reduce trigger-level noise, and/or to reject background at the analysis level. At this point, no robust and generally applicable strategy has been reported. For example, for multi-element arrays, the threshold drops as the square root of number of antennas, since the signal adds in-phase while the backgrounds add with random phases [137]. It seems, however, that e.g. triboelectric signals recorded in periods with winds exceeding 10 m/s are a problematic trigger-level background, for experiments in polar regions [138] and will require removal during analysis.

Most dedicated air shower experiments have used radio antennas in combination with at least one other detector technology, such as scintillation counters, if the site suffers from significant RF backgrounds and/or computing power on autonomous stations is limited. Exceptions are neutrino experiments with sensitivity to air showers, which are located in uninhabited polar regions, enabling them to relatively efficiently self-trigger on air showers [139, 140].

Lunar experiments (discussed below) use different techniques to reduce the anthropogenic background. Some experiments use multiple antennas, separated by at least hundreds of meters; by requiring a coincidence within a small time window, anthropogenic noise can be rejected. With good enough timing, beam-forming techniques can be used to further reduce the background. An alternative approach is to use beam forming with multiple feed antennas viewing a single reflector, to ensure that the signal points back to the moon.

Due to the similarity in the radio emission of air showers and neutrino showers, the more abundant cosmic rays can act as background to neutrino searches. In-ice detectors need to suppress in-air emission that is refracted into the ice, emission that is created from developing air showers continuing in the ice, as well as from stochastic energy-losses of atmospheric muons. Lunar experiments may faces challenges in separating neutrino interactions from cosmic ray interactions.

36.3.3.4 *Recent experiments*

Figure 36.9 shows some current limits from neutrino searches, including those from prototype arrays. Except for LOFAR, which is fully operational, projected limits from future experiments are not shown in the figure. Notably, the KM3NeT collaboration has observed an event with an energy above 100 PeV (with a central energy of 220 PeV) [141]. This observation is in tension (2.9σ) with the IceCube flux limit [142]. Various origin scenarios are being discussed.

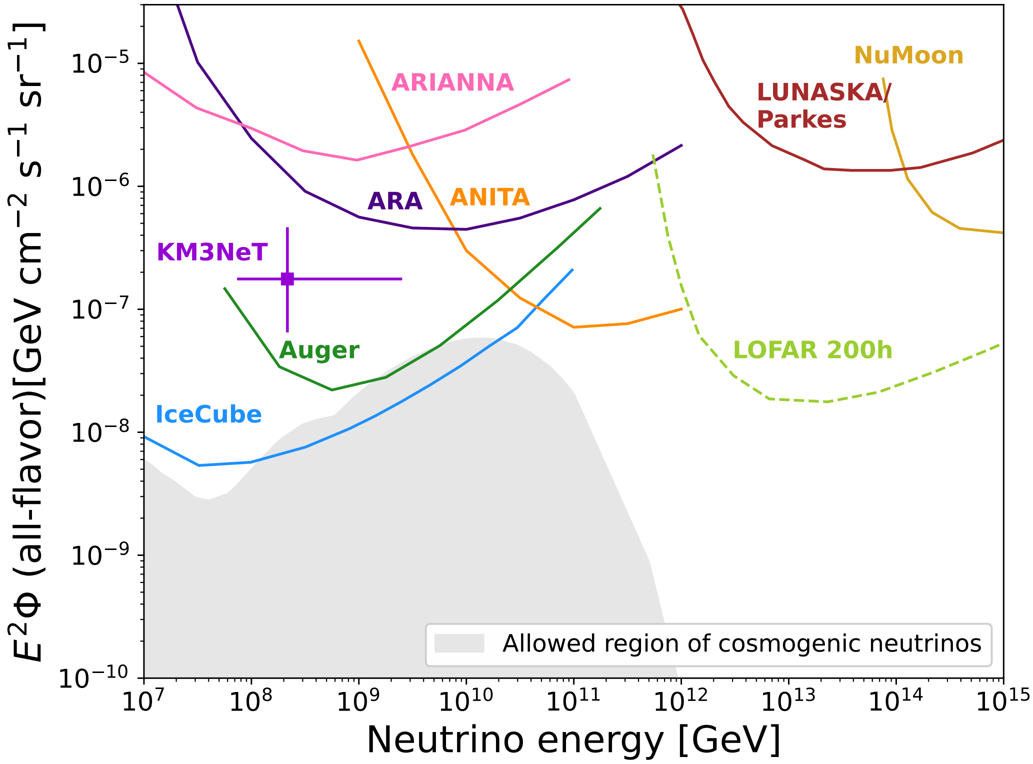

Figure 36.9: Representative 3-flavor (summed, assuming equal fluxes of each flavor) differential (over one decade in energy) limits from different experiments and prototype experiments. Shown are limits from the IceCube ultra-high energy ν search [142], the Auger search for earth-skimming ν_τ [143], the LUNASKA/Parkes [144] and NuMoon lunar searches [145], the ANITA balloon experiment [146], ARA [147] and ARIANNA prototypes [148], along with projections for the LOFAR array [149]. Also shown is the flux implied by the event seen by KM3NeT [141]. The ARA and ARIANNA limits are from prototype arrays, and indicate the energy range that might be covered, with far higher sensitivity by larger arrays (see 36.3.3.5). The shaded area is the allowed region for cosmogenic neutrinos from a recent global analysis as published in [104] following the methods from [150].

i. *Ice*

The most common dense medium transparent to radio waves is ice. Natural ice is an attractive medium for neutrino detection with radio attenuation lengths from over 300 m to 1 km [151]. The attenuation length varies with frequency and ice temperature, with higher attenuation in warmer ice. Although glacial ice is mostly uniform, the top $\approx$ 100 m of ice, the 'firn,' exhibits a gradual transition from packed snow at the surface (typically $\rho = 0.35$ g/cm^3) to solid ice ($\rho = 0.92$ g/cm^3) below [152]. The thickness of the firn varies with location; it is thicker in central Antarctica than in the coastal ice sheets or in Greenland. The density variation has several implications.

The index of refraction depends linearly on the density, so radio waves curve downward in the firn. This bending reduces the effective volume of shallow or aerial antennas. A shallow antenna cannot see near-surface interactions at large horizontal distances. There are also indications that the increase in firn density is slightly non-monotonic [153,154]. This leads to non-monotonic changes in index of refraction which may create waveguides that trap a small fraction of the radio energy and propagate it horizontally.

In one type of experiment, antennas mounted on high-altitude balloons observe the ice from above. Radio signals from in-ice neutrino interactions propagate to the surface, traverse the ice-air interface, and then travel to the balloon. The surface roughness of the ice can affect signals as they transition from the ice to the atmosphere. The best known example, ANITA, has made four flights around Antarctica, floating at an altitude around 35 km [155]. Its 32/40/48 (depending on the flight) dual-polarization horn antennas scanned the surrounding ice, out to the horizon (650 km away). Because of the small angle of incidence, ANITA could use polarization information to separate signals from background; ν signals should be vertically polarized, while most background from cosmic-ray air showers should be horizontally polarized.

As with all radio-detection experiments, ANITA had to contend with anthropogenic backgrounds. The ANITA collaboration uses their multiple antennas as a phased array to achieve good pointing accuracy, with a resolution of 0.2-0.4° in elevation, and 0.5-1.1° in azimuth. They rejected all events that pointed toward known or suspected areas of human activity. ANITA has set the most stringent flux limits yet on neutrinos with energies above 10^{20} eV [146]. The ANITA experiment has also reported several anomalous events, matching cosmic ray signals, but with unexpected polarization signature, which the collaboration has indicated might be from Earth-skimming ν_τ [156, 157]. However, this interpretation is controversial and firmly excluded by both Auger [158] and IceCube [142].

Because of the significant source-detector separation, ANITA is most sensitive at energies above 10^{19} eV. A lower energy threshold requires a smaller antenna-target separation.

Other ice based experiments use antennas located within the active volume, allowing them to reach thresholds around 10^{17} eV, or lower with phased array antennas. This approach was pioneered by the RICE experiment [159] which buried 18 half-wave dipole antennas in holes drilled for AMANDA at the South Pole, at depths from 100 to 300 m. The hardware was sensitive from 200 MHz to 1 GHz. Each antenna fed an in-situ preamplifier which transmitted the signals to surface digitizing electronics.

Following RICE, two groups have deployed prototype arrays which have explored different detector concepts. The Askaryan Radio Array (ARA) deployed surface and buried antennas at the South Pole [160], while the Antarctic Ross Iceshelf Antenna Neutrino Array (ARIANNA) installed shallow antennas on the Ross Ice Shelf [148], about 110 km north of McMurdo station. ARIANNA offered the possibility of detecting downward-going ν, from the radio waves reflected off the ice-sea water interface on the bottom of the Ross Ice Shelf, while ARA took advantage of the colder, deeper ice at the South Pole, with its longer radio attenuation length. ARA buried antennas up to 200 m deep to be able to observe a larger portion of ice, due to the refraction of the signal in the firn. In contrast, ARIANNA deployed antennas just below the surface, allowing them to use high-gain, but large log periodic dipole antennas. At ARA, phased-array trigger techniques have been demonstrated that can reduce the energy threshold by a factor of several [137, 161].

Both experiments use stations which operate independently, spaced far enough to maximize sensitivity, but where only a small fraction of neutrino events will be visible in multiple stations. Each station includes multiple antennas, which will be sensitive to both horizontal and vertical polarization. The expected angular resolution is a few degrees [136].

The Radio Neutrino Observatory Greenland (RNO-G) is under construction at Summit Station, Greenland, where the ice is about 3,000 m thick. RNO-G is planned to consist of 35 stations, which employ ARIANNA-style shallow antennas, an ARA-style phased array and deep antennas, and draws on ANITA's electronics heritage [162]. Installation speed is limited by the drill speed. In July, 2025, 8 stations were operational with holes for 4 additional stations prepared for installation.

ii. *The Moon*

Because of its large size and non-conducting regolith, and the availability of large radio-telescopes, the Moon is an attractive target [163]. Conventional radio-telescopes are quite well suited to lunar neutrino searches, with natural beam widths not too dissimilar from the size of the Moon. Still, there are experimental challenges. The attenuation length is typically estimated to be 9 m/f(GHz) [164], so only near-surface interactions can be studied. The composition of the lunar regolith is not well known, and there are significant uncertainties due to this uncertainty. One big limitation of lunar experiments is that the 385,000 km target-antenna separation leads to energy thresholds above 10^{20} eV.

The effective volume probed by experiments depends on the geometry, which itself depends on the frequency range used. At high frequencies f, the electric field strength is high, leading to a lower energy threshold, but the sensitive volume is limited because the Cherenkov cone only points toward the Earth for a narrow range of geometries. Lower frequency radiation is more isotropic, so the effective volume is larger, but, because the electric field is weaker, the energy threshold is higher. The $1/f$ dependence of the attenuation length in the lunar regolith further increases the effective volume at low frequencies. The frequency range affects the energy dependence of the sensitivity. As can be seen in Fig. 36.9, a low-frequency experiment like NuMoon (which covered 115-180 MHz) has good sensitivity, but only above about 10^{14} GeV, while Lunaska/Parkes, which observed in the range 1200-1500 MHz, has a higher flux limit, but is sensitive above about $10^{12.5}$ GeV.

Current limits and projected sensitivities are sensitive to many details. A recent review [165] compared different radio-detection experiments using a common framework, and found some significant shifts in sensitivities due to, e.g. different assumptions about lunar composition and inelasticities.

With modern technology, it is increasingly viable to search over very broad frequency ranges [166]. One technical challenge is due to dispersion (frequency dependent time delays) in the ionosphere. Dispersion can be largely removed with a de-dispersion filter, using either analog circuitry or post-collection digital processing.

iii. *Air*

Radio detection in air is sensitive to all particles inducing air showers. Radio-detection can be used to determine the energy of cosmic rays, as done by e.g. the Auger and Tunka-Rex experiments [167,168]. Radio signals can also be used to infer the atmospheric depth for shower-maximum, where the shower contains the most particles, as done by e.g. the LOFAR and Tunka-Rex collaborations [168, 169]. This depth is sensitive to the cosmic-ray composition. Reconstructing the particle arrival direction is much easier in air since the Cherenkov angle, and thus the radio wavefront, aligns with the axis to 1°. Radio-detection is also useful for energy cross-calibrations between different experiments. The Pierre Auger collaboration has recently shown that radio can provide an independent energy scale calibration, in good agreement with the other detectors of the observatory [170].

One variation on the radio-detection approach is to look for radio emission from Earth-skimming ν_τ [171, 172]. Although ν_τ are much less commonly produced than ν_μ and ν_e, over astrophysical distances, oscillations lead to a $\nu_e : \nu_\mu : \nu_\tau$ ratio near $1 : 1 : 1$, for almost all non-exotic acceleration and propagation mechanisms.

If the ν_τ traverse the Earth and interact while traveling upward, the resulting $\tau^\pm$ may exit the Earth before decaying. 83% of the time, the decay produces a hadronic or electromagnetic shower in the atmosphere [173]. Experiments have searched for these upgoing showers, and for the resulting optical Cherenkov and coherent RF radiation. The threshold energy dependence for these searches depends on several factors, notably including the average $\tau^{\pm}$ decay length, which increases linearly with energy. For somewhat lower energy ν_τ, with shorter decay lengths, a mountain may serve as a target, with $\tau^{\pm}$ expected to emerge from the other side. The Pierre Auger observatory sets stringent limits on this neutrino flux at energies above 10^{17} eV [143]. The Pierre Auger Collaboration has recently upgraded their surface array to include radio antennas at all water Cherenkov detectors. This array will improve the sensitivity of the instrument to horizontal showers, both for composition sensitivity for cosmic rays and for the detection of Earth skimming neutrinos [174].

36.3.3.5 *Future experiments*

Looking ahead, RNO-G [162] will continue deployment in the next years and has reached the largest yearly sensitivity of any radio array thus far. Further out, the proposed IceCube-Gen2 expansion includes a substantial radio array component [104], which will be sensitive to both neutrinos from the ice and air showers from cosmic rays. PUEO, a successor of ANITA, with significantly improved sensitivity, completed its first flight early 2026 [175].

For lunar neutrino detection, several large radio detector arrays should reach significantly lower energies in the near future. The LOFAR array is taking data with 36 detector clusters spread over Northern Europe [149]. Also, the Square Kilometer Array (SKA) with its roughly 60,000 antennas will push thresholds down to near 10^{20} eV [166]. The SKA will also study air showers [176].

A number of dedicated prototype ν_τ radio-detection experiments exist. The GRAND Collaboration, e.g., is proposing to deploy a large array of simple autonomous radio stations optimized for near-horizontal signals [177]. As of 2025 a first proto-array is operational.

36.4 Large time-projection chambers for rare event detection

Written October 2025 by L. Baudis (Zurich U.).

Initially developed for particle physics experiments at accelerators (see *Section 35.6.5*), the concept of a Time Projection Chamber (TPC) [178] evolved and is now tailored to a large range of applications, most notably to experiments in astroparticle physics searching for rare interactions deep underground. Present and proposed experiments designed to observe interactions of dark matter and other exotic particles, second order weak nuclear decays, as well as neutrinos from a variety of sources are based on TPCs operated with pure noble elements, either in gaseous or liquid form. The detectors aim for large target masses, low energy thresholds (keV-scale) and ultra-low levels of backgrounds from radioactivity and cosmic rays. Historical introductions, reviews of the operation principles, instrumentation and technological aspects, as well as applications, are found in Refs. [179–184].

The two most common noble fluids employed as detector media in present TPCs for rare event searches are argon and xenon, either as a high-pressure gas, or in liquid phase, or in liquid and gas phase (dual-phase). An interaction within the active volume of a TPC will create ionisation electrons and scintillation photons. The prompt scintillation signal is detected with one or two arrays of photosensors, while the ionisation electrons, which drift in the pure medium under the influence of an external, uniform electric field, are observed either directly with charge sensors, or via proportional scintillation, or electroluminescence. Since transverse electron diffusion is small, albeit non-negligible, the ionisation signal provides the $x - y$ information of the interaction site, with the $z-$information coming from the drift time measurement. The TPC thus yields a three-dimensional event localisation, enabling fiducial volume selections and differentiation between single- and multiple-scatters in the active volume. These features are crucial for filtering out rare events from the much higher backgrounds due to residual radioactivity of detector components.

The specific energy loss (dE/dx) depends on the primary interacting particle, and leads to a distinct ratio of scintillation to ionisation for gammas/electrons, alphas and fast neutrons, allowing for further background discrimination. Two examples for the operation principle of TPCs for rare event detection are shown in Fig. 36.10.

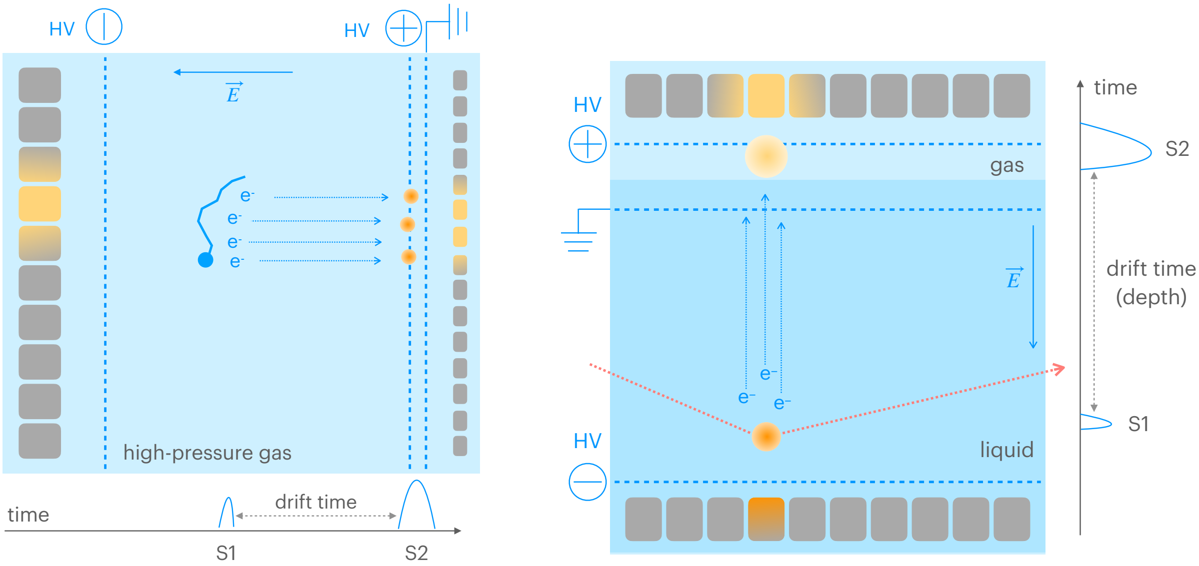

Figure 36.10: Operation principle of TPCs for rare event detection: a high-pressure gas (left) and a dual (liquid/gas) phase (right) TPC. A particle interaction yields a prompt scintillation signal (S1) and a delayed, amplified proportional scintillation signal (S2). The latter is caused by ionisation electrons drifted in a homogeneous electric field (and, for dual phase TPCs, extracted into the gas phase above the liquid). In these examples, both S1 and S2 signals are observed with photosensor arrays placed behind the anode and cathode (left), or at the top and bottom (right) of the TPC. The position information along the drift field is inferred from the time difference between the two light signals, while the position in the transverse plane to the field is derived from the S2 light pattern in the photosensor plane close to the electroluminiscent light production site.

The properties of liquid argon as detection medium in a TPC are reviewed in *Section 35.7*. Here some properties for xenon are given in Tab. 36.5. In the liquid phase, the high xenon density allows for compact, large and homogeneous detector geometries with efficient self-shielding against external radiation, given that the cross sections for the photoelectric effect, Compton scattering and pair production scale as $Z^5/E_\gamma^{7/2}$, Z/E_γ and $Z^2\ln(2E_\gamma)$, respectively, for incoming X-rays and gammas with energy E_γ. The radioactive isotopes ^{124}Xe, ^{126}Xe, ^{134}Xe and ^{136}Xe have very long half-lives, and their second-order weak decay modes are subject to investigation (see *Section 36.4.2*).

In an argon or xenon detector, the energy loss of an incident particle is shared between ionisation, excitation and sub-excitation electrons liberated in the ionisation process. The average energy loss in ionisation is slightly larger than the ionisation potential, as it includes multiple ionisation processes. In their condensed phases, argon and xenon exhibit a band structure of electronic states, with the band gap energy being around 14.3 eV and 9.3 eV for liquid argon and xenon, respectively. In gaseous xenon, the ionisation potential is about 12.1 eV. Scintillation arises from excited atoms (excitons) and from ions, via recombination, with the emitted vacuum-ultraviolet (VUV) photons in single bands centred at $\lambda = 128$ nm for argon and $\lambda = 175$ nm for xenon. The excited dimers (or excimers), at their lowest excited level, de-excite to the dissociative ground state by the emission of a single VUV photon. This comes from the large energy gap between the lowest excitation and the ground levels, forbidding other decay channels such as non-radiative transitions. The scintillation light has two decay components due to de-excitation of spin singlet and spin triplet states of the excited dimers to the ground state. The singlet and triplet states refer to the total spin quantum number (s=0 or s=1) of the excited Rydberg electron and the angular momentum due to the molecular orbit, with the shorter and longer decay shapes being produced by the de-excitation of s=0 states (spin-allowed) and s=1 states (spin-forbidden), respectively. The different pulse decay time for different type of particle interactions, and thus ionisation densities, is employed to discriminate electronic from nuclear recoils. While this is very effective in liquid argon, due to the large time separation of (6 ± 1) ns versus (1500 ± 100) ns, it is more difficult to put in practice for xenon [185], considering the much smaller separation, (2.2 ± 0.3) ns versus (27 ± 1) ns, of the two components.

Table 36.5: Physical properties, volume fraction in the atmosphere, radioactive isotopes of the noble element xenon.

Property [unit]	Xe
Atomic number, mean atomic mass [g/mol]	54, 131.29
Boiling T_b and melting T_m point at 1 atm [K]	165.0, 161.4
Gas density at 1 atm and 298 K (T_b) [g/l]	5.40 (9.99)
Liquid density at T_b [g/cm^3]	2.94
Volume ratio ($\rho_{\text{liduid}}/\rho_{\text{gas}}$)	526
Dielectric constant of liquid	1.95
Scintillation light yield (in liquid, at 122 keV) [186]	63 photons/keV
Wavelength (peak centred at)	175 nm
Decay time constants (s=0, s=1)	2.2 ns, 27 ns
Refractive index	1.69
Electron mobility* [188]	0.29 mm^2/(μs V) ($\lesssim$100 V/cm) 0.01 mm^2/(μs V) ($\gtrsim$100 V/cm)
Volume fraction in Earth's atmosphere [ppb]	87
Isotopes with spin, abundance [%]	^{129}Xe, 26.44; ^{131}Xe, 21.18
Radioactive isotopes, abundance [%] and T$_{1/2}$ [y]	^{136}Xe, 8.87; 2.2×10^{21} [189,190] ^{124}Xe, 0.095; 1.1×10^{22} [191–193] ^{134}Xe, 10.4; $>8.7\times10^{20}$ (90% C.L.) [194] ^{126}Xe, 0.089; $>1.9\times10^{22}$ (90% C.L.) [195]

*Measured values in two benchmark regimes, so-called "cold" and "hot" electrons [187]. In the first case, the electron energies are due to thermal bath of the xenon fluid and they rapidly gain energy with increasing field; in the second case, the electrons have gained most of their energy through acceleration in the field and experience increased energy loss on their path due to collisions with Xe atoms.

The recombination-independent, mean energy required to produce a single detectable quantum (photon or electrons), called the W-value, assumes that each recombining electron-ion pair produces an exciton, which leads to a photon. In liquid argon, the W-value is (19.5 ± 1.0) eV [196]. In liquid xenon, the widely-adopted W-value is (13.7 ± 0.2) eV, measured with 122 keV γ-rays from an external ^{57}Co source [197]. Recently, a lower value of $11.5^{+0.2}_{-0.3}$ (syst.) eV was obtained in a small TPC with internal sources at energies between 2.8 keV and 42 keV [198], consistent with the value measured at the MeV-scale, 11.5 ± 0.5(syst.) $\pm\, 0.1$(stat.) eV with the EXO-200 detector [199]. The ionisation and scintillation W-values in gaseous xenon are 24.8 eV and (76 ± 6) eV, respectively [200].

The partition between excitation and ionisation depends on the density of the electron-ion pairs produced along the track of a particle, and the recombination fraction depends on the applied electric field, as well as on the ionisation density in the track. While several phenomenological models exist to describe electron-ion recombination as a function of stopping power and electric drift field (see [179] and discussions therein), a solid theory of energy loss of low-energy ions in noble fluids is still missing. For nuclear recoils as generated by interactions of neutrons, neutrinos or hypothetical WIMPs, an energy-dependent quenching is introduced via the Lindhard factor $\mathcal{L}$ [201], with $\mathcal{L}$ being around $0.2-0.25$ and $0.15-0.2$ in liquid argon [202] and xenon [203], respectively, at nuclear recoil energies in the range 3-100 keV. A comprehensive framework to simulate scintillation and ionisation yields in argon and xenon as a function of interaction type, energy and electric field in a TPC is the Noble Element Simulation Technique (NEST) [204].

To calibrate the energy scale and determine the energy resolution of low-background TPCs, mono-energetic lines from external (e.g., ^{57}Co, ^{60}Co, ^{137}Cs, ^{228}Th, etc) and internal (^{83m}Kr, ^{37}Ar) calibration sources, as well as from neutron activation lines (e.g., ^{129m}Xe, ^{131m}Xe in xenon) are used. Relative energy resolutions (σ/μ) at the level of 4-6% at energies of a few tens of keV and 2-3% at energies of a few 100 keV were reached in argon and xenon TPCs, respectively. At higher energies, relevant for the neutrinoless double beta decay of ^{136}Xe, relative resolutions of 0.67%, 0.8% and 1.2% around 2.5 MeV were obtained by LZ [205], XENON1T [206] and EXO-200 [207], respectively. Superior energy resolutions are attained in high-pressure gas TPCs with electroluminiscent amplification [208], with a relative resolution of 0.4% obtained in the NEXT-White detector [209]. This is due to the fact that the Fano factor in pure gaseous xenon, $\mathrm{F_{GXe}} = 0.15\pm0.02$, is about two orders of magnitude smaller than in the liquid phase.

To achieve a high collection efficiency for both ionisation and scintillation signals, the concentration of impurities is reduced and maintained at a level below one part per 10^9 (ppb) oxygen equivalent. While the light can be strongly reduced by the presence of water vapour, the ionisation signal also requires high purity in terms of molecules with high electronegative affinity. The purity is commonly expressed via the electron drift lifetime, τ_e, which is the time over which the number of drifting electrons, n_e, is reduced by a factor e: $n_e(t) = n_e(t_0)\exp(-t/\tau_e)$. Ideally, τ_e should be a few times larger than the total drift time in a TPC, to prevent charge losses. Lifetimes > 10 ms were achieved both in argon and xenon (corresponding to impurity concentrations $\ll$1 ppb O_2 equivalent) via continuous recirculation and purification in the liquid or gas phase.

The drift velocity of electrons, which depends on the drift field E_d and the electron mobility μ as $v_d = \mu \cdot E_d$, has been measured for drift fields between $\sim(10-10^4)$ V/cm. It also depends on the temperature in the medium and the impurity concentration, often making the comparison between different measurements difficult. In general, the drift velocity raises from about 0.25 mm/μs at low fields to 2 mm/μs at high fields in both argon and xenon. As electrons drift in the electric field, the initial electron cloud spreads both in longitudinal and transversal direction to the field, expressed in terms of longitudinal D_L and transversal D_T diffusion coefficients, with $D_L < D_T$ and $D_L/D_T \approx 1$ for fields approaching zero. In argon, D_L was measured as $\sim$4.2 cm^2/s at 200 V/cm [210], $\sim$3.7 cm^2/s at 274 V/cm [211], $\sim$7.2 cm^2/s at 500 V/cm and D_T as $\sim$12 cm^2/s [212]. In xenon, D_L is around 100 cm^2/s at low fields, reaching $\sim$25 cm^2/s at higher drift fields [188], while D_T has been measured to be $\sim$55 cm^2/s at fields between (20-600) V/cm [213]. As an example, the spatial distribution of an initially point-like electron cloud, after a drift time t, is $\sigma_D = \sqrt{2Dt}$, resulting in a value of $\sim$20 mm for 1 ms drift and a 25 cm^2/s diffusion coefficient.

The scintillation light can be attenuated by absorption on impurities or due to Rayleigh scattering, the latter depending strongly on the wavelengths of the photons and the optical properties of the materials. Since only the combined effect is observed, it is non-trivial to disentangle the two contributions. A combination of measurements and theoretical calculations yield total attenuation and Rayleigh scattering lengths between 55-110 cm and 60-99 cm for argon and 30-50 cm and 30-50 cm for xenon detectors, with refractive indexes between 1.34 and 1.57-1.72, respectively, and absorption lengths >100 cm [179, 214].

Background sources for rare-event searches, their mitigation techniques and radio-purity assays are discussed in *Section 36.6* of this *Review*. The main backgrounds in large TPCs are due to decays of other noble isotopes mixed with the argon and xenon (^{39}Ar, ^{85}Kr, ^{222}Rn), from natural, anthropogenic or cosmogenic radioactivity of detector materials in close proximity to the target (^{238}U, ^{232}Th, ^{40}K, ^{60}Co), and from muons and their secondary particles, including *in situ* production of isotopes which are sufficiently long-lived to render their vetoing difficult (e.g., ^{137}Xe in xenon TPCs). Astrophysical neutrinos cause largely irreducible backgrounds in dark matter detectors, but deliver exciting physics signatures in their own right. To mitigate the ^{39}Ar background, argon is extracted from underground sources (CO$_2$ wells), ^{85}Kr and ^{222}Rn are reduced by cryogenic distillation, exploiting the different vapour pressures of the different noble gases, or with gas chromatography using synthetic charcoal. In xenon detectors, $^{\mathrm{nat}}$Kr concentrations of < 50 ppq [215] and ^{222}Rn concentrations of 0.8 μBq/kg were achieved by cryogenic distillation In argon TPCs, ^{39}Ar concentrations of (0.73 ± 0.11) mBq/kg were demonstrated [216].

An overview of large TPCs for rare event searches is given in Table 36.6.

Table 36.6: Experiments using large TPCs for rare event searches. Shown are current, soon-to-be-operating and proposed experiments. UAr stands for underground argon; HP-GXe stands for high-pressure gaseous xenon. For some of the proposed experiments, the location or the readout scheme is not yet decided (marked as "TBD").

Experiment	Location	TPC type	Total (active) mass	Readout
Dark matter				
DarkSide-20k	LNGS	Dual-phase, UAr	50 t (50 t)	SiPMs, TPB
Argo	SNOLAB	Dual-phase*, UAr	∼400 t (∼400 t)	SiPMs, TPB
LUX-ZEPLIN	SURF	Dual-phase, Xe	10 t (7 t)	3″ PMTs
PandaX-4T	CJPL	Dual-phase, Xe	5.6 t (3.7 t)	3″ PMTs
PandaX-xT	CJPL	Dual-phase, Xe	47 t (43 t)	2″ PMTs
XENONnT	LNGS	Dual-phase, Xe	8.6 (5.9 t)	3″ PMTs
XLZD	TBD	Dual-phase, Xe	50-100 t (40-80 t)	3″ PMTs
$0\nu\beta\beta$ decay				
nEXO	SNOLAB	LXe, ^{136}Xe 90%	4.8 t (3.65 t)	SiPMs, charge pads
NEXT-100	LSC	HP-GXe, ^{136}Xe 90%	100 kg (80 kg)	3″ PMTs, SiPMs, TPB
NEXT-HD	TBD	HP-GXe, ^{136}Xe 90%	1.2 t (1 t)	Fibres + SiPMs, TPB
PandaX-III†	CJPL	HP-GXe, ^{136}Xe 90%	140 kg (100 kg)	Micromegas

*The option to build Argo as a single-phase detector is also under consideration.
†This is an R&D program for a future larger, enriched PandaX-xT detector.

36.4.1 *Dark matter and other low energy signals*

TPCs built to search for particle dark matter are based on the two-phase principle. Starting with total masses of a few kilogram the detectors evolved and reached active target masses at the tonne- and more recently multi-tonne scale. Concomitantly, the background levels in the most inner regions constantly decreased, with current electronic recoil rates of 15 events/(t y keV) in the energy region below 100 keV for xenon detectors [217]. Typically, the TPCs contain two arrays of photosensors, one immersed in the liquid, and one in the gas phase above the liquid at similar low temperature. The xenon scintillation light can be observed directly by PMTs with synthetic silica (quartz) windows or with VUV-sensitive SiPMs, while for argon detectors, tetraphenyl butadiene (TPB) is used to shift the 128 nm light to 420 nm, given that it is absorbed by quartz windows.

The DarkSide-50 experiment [216] operated a 50 kg TPC with liquid argon depleted in ^{39}Ar until 2019. DarkSide-20k [218], to operate 51.1 t of underground LAr in an octogonal TPC, the walls made of gadolinium-loaded acrylic panels, with two arrays of SiPMs, is under construction in Hall C of the Laboratori Nazionali del Gran Sasso (LNGS) in Italy. The first filling with liquid argon is planned for the end of 2026, with data taking starting in 2027. A larger, 400 t LAr detector, Argo, has been proposed for SNOLAB in Canada. After the successful operation of TPCs for LUX, PandaX-II and XENON1T, the current generation of xenon detectors, LUX-ZEPLIN (LZ) [219] at the Sanford Underground Facility (SURF) in USA, PandaX-4T [220] at the China Jinping Laboratory (CJPL) and XENONnT [221] at LNGS, employ several tons of LXe as active target mass. Their overall TPC design is rather similar, with cylindrical, polytetrafluoroethylene (PTFE) enclosed target regions viewed by two arrays of low-radioactivity, 3-inch diameter Hamamatsu R11410 PMTs. The PTFE has a high reflectivity for the Xe scintillation light [222]. Next-generation detectors, at the 50 t LXe scale or beyond, have been proposed with XLZD [223] and PandaX-xT [224], while DARWIN [225, 226] continues the R&D towards XLZD. Recent constraints on various dark matter candidates are presented in *Section 27.6.* The search for WIMP dark matter is ongoing, with the sensitivity goal of current experiments to the spin-independent WIMP-nucleon cross section around $1.5\times10^{-48}\,\mathrm{cm}^2$ at 40-50 GeV/c^2 mass [219, 221].

Owing to low electronic recoil backgrounds and low energy thresholds in noble liquid TPCs, high-sensitivity searches for dark matter electron scattering with particle candidates from a hidden sector, for keV-scale axion-like-particles (ALPs) and dark photons via absorption in LXe, as well as searches for solar axions, became feasible (see *Section 27.6*). Looking at ionisation-only signals allows for a further reduction of the energy threshold, given the much higher efficiency to detect an ionisation electron compared to a primary scintillation photon (typically 90% versus 10%). While this gain comes at the expense of higher backgrounds, it allows nonetheless to set stringent limits on light dark matter electron interactions at masses from a few tens of MeV to a few GeV, as shown by DarkSide-50 [227], PandaX-4T [228], XENONnT [229] and LZ [230]. Further, current-generation dual-phase TPCs have reached target masses which will allow for the first time the detection of solar *pp* neutrinos via elastic neutrino-electron scattering at energies down to 1 keV. Recently, the first detection of ^{8}B neutrinos via coherent elastic neutrino-nucleus scattering (CEνNS) was reported by PandaX-4T [231] and XENONnT [232].

Dual-phase TPCs were successful in gradually scaling up their target mass and in reducing the background levels for each iteration, while maintaining a low-energy threshold of ∼1 keV for electronic recoils. Notwithstanding, the construction of next-generation detectors at the multi-ten-tons scale poses multiple technological challenges. The background goals are such that electronic and nuclear recoils rates are below the ones from irreducible astrophysical neutrino interactions. This requirement sets the goals for the intrinsic ^{222}Rn and ^{85}Kr concentrations: the background from the decay of these isotopes should be significantly lower than the solar pp-neutrino elastic scattering rate. This translates into 0.1μBq/kg for ^{222}Rn[2] and 0.1 ppt (parts per billion, or 10^{-9}) for $^{\mathrm{nat}}$Kr, assuming a ^{85}Kr/$^{\mathrm{nat}}$Kr ratio of 2×10^{-11}mol/mol. While $^{\mathrm{nat}}$Kr concentrations of $<$ 50 ppq (parts per quadrillion, or 10^{-15}) were already achieved, for ^{222}Rn a factor of about 10

---

[2] A ^{222}Rn concentration of 0.1μBq/kg corresponds to less than one radon atom per 100 mol of xenon. The main background is due to ^{214}Bi β-decays which are not accompanied by an α-decay and thus cannot be tagged in the TPC.

reduction compared to the current values [233] is needed. This calls for a high liquid throughput (close to 1 t/hour) with efficient cooling power based on cryogenic heat pumps and radon-free heat exchangers. Cryogenic distillation or charcoal chromatography must go hand in hand with selection of low radon emanation materials and new coating techniques to prevent radon emanation from surfaces.

Other challenges related to the liquid target are the continuous purification for electronegative impurities and water, to maintain high charge and light yields, while not introducing radon into the TPCs, as well as new solutions for reliable storage and recuperation at large scales. A dedicated single-closed-loop cryogenic system capable of handling 100 t of underground argon was designed and constructed for DarkSide-20k [234]. Liquid phase purification powered by a liquid xenon pump, as demonstrated in [235], was employed to achieve an electron drift lifetime above 15 ms in about 8.6 t of xenon in XENONnT. A system capable of handling 30 t of xenon in liquid phase, including long-term storage and and transfer of the cryogenic liquid between storage module and detectors was constructed for PandaX-xT [224, 236].

Regarding the detector design, electrodes with large (>2.5 m) diameters, with high transparency, minimal sagging and low spurious electron emission, as well as high-voltage feed-throughs that can safely deliver 50 kV or more to the cathode must be employed. DarkSide-20k will use for the first time anode and cathode plates made out of acrylic coated with a commercial conductive polymer and with TPB. LZ successfully built custom-woven wire-mesh grids with 1.5 m diameter, produced with an in-house built loom to weave the wire meshes [237]. Finally the cryostat design must ensure stability, while reducing as much as possible the amount of material, and thus gamma and neutron emitters in proximity to the TPCs.

Besides Ar and Xe TPCs, detectors using superfluid ^{4}He, targeted at low-mass dark matter, are under development within the HeRALD [238] and DELight [239] programs, based on the basic principles demonstrated by the HERON solar neutrino project [240]. The detectors will be instrumented with transition edge sensors or magnetic micro-calorimeters to observe both atomic signals, such as scintillation light, and quasiparticle (phonon and roton) excitations. As in other noble elements, the He_2^* dimers appear in a short-lived (<10 ns) singlet and long-lived (13 s) triplet state. The former decay promptly, emitting photons with energies peaked around 16 eV, while the triplet states can propagate through the fluid and de-excite at surfaces. Liquid helium is transparent to its VUV photons, since the first excited state of atomic helium is at 20 eV. Quasiparticles will propagate ballistically through the liquid without decaying, and can also be detected via the evaporation of ^{4}He atoms from the surface of the liquid, with the helium binding energy being ∼0.7 meV.

Large volume, low-background TPCs are also developed for directional dark matter searches. An example is CYGNO [241] which aims to built a TPC with 50 cm drift, filled with a He:CF_4 gas mixture at room temperature and atmospheric pressure at LNGS. The liberated charge in a particle interaction is drifted towards an amplification stage consisting of a triple GEM structure, where the charge is multiplied and also light is produced. The readout will consist of light detectors, PMTs and scientific CMOS cameras, yielding the energy and z-position of events and the 2D track projections, respectively. The combined information thus allows for a 3D track reconstruction, with the goal being to achieve energy thresholds for electronic recoils around 1 keV.

36.4.2 $0\nu\beta\beta$ *Decay*

Experiments built to search for the $0\nu\beta\beta$-decay of ^{136}Xe, at a Q-values of 2457.8 keV, are based on single-phase TPCs, filled either with liquid or gas xenon at high pressure. The drift region is horizontal (EXO-200, NEXT-100) or vertical (nEXO, NEXT-HD, PandaX-xT-enriched).The TPCs are enclosed by radio-pure, thin-walled Cu vessels in a cryofluid, hydro-fluoro ether, or in a cold liquid scintillator, acting as a thermal bath, radiation shield and active veto in the latter case. In EXO-200, which took data at the Waste Isolation Pilot Plant (WIPP) until 2018, the charge drifted to crossed-wire planes at each anode, while the light was collected by arrays of large area avalanche photodiodes placed behind the wire planes at both ends. In nEXO, the TPC vessel is planned as a vertical Cu cylinder with 130 cm height and diameter (for 118.3 cm drift), with the charge collected at the anode by 0.6 cm pitch and 9.6 m long electrode strips, and the scintillation light observed by SiPMs arranged in a barrel configuration. Unlike for dark matter TPCs, there are no reflector panels and the field rings and cathode are coated with reflective aluminium deposition. The design drift field is 400 V/cm and the goal for the relative energy resolution is 0.8%. EXO-200 set a lower limit on the half-life of $0\nu\beta\beta$-decay of 3.5×10^{25} y with a total exposure of 231.4 kg y [242]. The proposed nEXO aims for a sensitivity of 1.35×10^{28} y with 5 t of enriched xenon and ten years of data taking [243].

TPCs using high-pressure xenon gas aim to reconstruct the tracks from the two electrons emitted in double beta decays, and the decay vertex, thus providing also a topological signature. In the NEXT project at the Laboratorio Subterráneo de Canfranc (LSC), the horizontal TPC, to be operated at 10-15 bar, features a single drift region. The primary (S1) and secondary (S2) scintillation light, the latter due to electroluminescence when the ionisation electrons cross a high-field region close to the anode, are collected by arrays of PMTs and SiPMs placed behind the cathode and anode, respectively, for energy measurements and tracking. The surfaces facing the active volume are coated with TPB to shift the VUV light to the visible spectrum. An inner Cu shield absorbs radiation from the high-pressure vessel of the cryostat.

The NEXT-White experiment, a prototype for NEXT-100 and for the proposed tonne-scale NEXT-HD, has operated a TPC with 20.8 cm radius and 53 cm drift, with 4.3 kg of xenon at 10 bar until 2023. It demonstrated excellent energy resolution ($< 1\%$ FWHM [209]) and background rejection using the capability to reconstruct the trajectories of ionising charges in the gas, thus separating the two-electron signature of $\beta\beta$-decay from single electrons due to background sources [244, 245]. Using data collected with xenon enriched and depleted in ^{136}Xe, it measured the half-life of the $2\nu\beta\beta$-decay and demonstrated clear Bragg peaks for the two electrons emitted in the decay [246]. NEXT-100 is currently acquiring data at LSC 5 bar [247], and will operate with >10 bar in 2026-2027. NEXT-HD will operate a vertical-drift TPC, 2.6 m in diameter and height, to accommodate ~1.1 t of enriched xenon at 15 bar [248]. An intense R&D programe for the *in situ* identification of the barium ions (^{136}Ba^{2+}, ^{136}Ba^{+}) produced in the $0\nu\beta\beta$-decay (called Ba-tagging) is ongoing [249–251]. PandaX-III, an R&D program for a future, enriched PandaX-xT detector, operates a high-pressure Xe gas TPC, where the xenon is mixed with 1% trimethylamine (TMA) to ensure stable operation of the Micromegas employed in the readout planes, and to minimise electron diffusion [252, 253]. Experimental searches for $0\nu\beta\beta$-decay are discussed in more detail in *Section 14.9*.

Apart from enriched xenon detectors, large TPCs using xenon in its natural isotopic abundance are also sensitive to second-order weak decays, such as the double beta decay of ^{134}Xe and ^{136}Xe, and the double electron capture process in ^{124}Xe and ^{126}Xe. In its electronic recoil channel, XENON1T observed for the first time the 2νECEC process in ^{124}Xe by detecting the simultaneously emitted K-shell X-rays/Auger electrons of the daughter atom ^{124}Te with a combined energy of 64.33 keV, which is twice the K-shell binding energy [191, 254]. The decay has also been observed by LZ [192] and PandaX-4T [193]. With a half-life around 1×10^{22} y, this is the slowest process ever measured directly. The double electron capture in ^{124}Xe can also be studied with high-pressure xenon gas TPCs, as demonstrated by NEXT [255]. LZ, PandaX-4T and XENONnT will improve upon existing results and will also search for the $2\nu\beta^{+}$EC decay. This channel has a distinct signature due to the two 511 keV gammas emitted after the positron annihilates with an electron in the medium. With a predicted half-life around 1.6×10^{23} y [256] its first observation is within reach of these running experiments, which will also measure the half-life and in particular also the shape of the $2\nu\beta\beta$-decay of ^{136}Xe with high statistics and at low energies not previously accessed. The current generation of dark matter detectors can also set constraints on the $0\nu\beta\beta$-decays of ^{136}Xe and ^{134}Xe, as predicted or shown in [191,257–261], delivering proof-of-principle methods towards higher sensitivity searches in XLZD and PandaX-xT. As an example, with 80 t of natural xenon in a TPC, a ^{136}Xe half-life exclusion sensitivity of 1.3×10^{28} y (90% C.L.) can be reached after ten years of operation [262,263], fully probing the inverted neutrino mass ordering scenario.

36.5 Sub-kelvin detectors

Revised October 2025 by O. Cremonesi (INFN, Milano-Bicocca), L. Hsu (FNAL) and G. Signorelli (Pisa U.; INFN, Pisa).

36.5.1 *Motivation for Sub-kelvin Detectors*

Detectors operating below 1 K are referred to as low-temperature detectors (LTDs). The advantage of using LTDs over conventional detectors resides in their better energy resolutions, lower noise, and improved energy thresholds, which can all be achieved with a versatile choice in materials. In certain applications, these advantages outweigh the potential drawbacks of cooling and reading out a detector payload at sub-kelvin temperatures, and thus enable exploration of new frontiers in fundamental physics, astrophysics and cosmology. Among the endeavors enabled by LTDs are direct searches for dark matter over a wide mass range, precision experiments to measure the electron neutrino mass, searches for neutrinoless double-beta decay, and X-ray observation of the Universe. Large arrays of LTDs are also employed to measure the properties of the cosmic microwave background (CMB) spectrum whose parameters are determined by fundamental physics. These include dark matter and dark energy densities, the sum of neutrino masses and the number of light relativistic species, as well as probing the physics of inflation at energy scales of $\sim 10^{16}$ GeV. This article presents a brief overview of LTDs, their features, and several applications. More detailed treatment of this subject is available in the literature [264–267].

The advantages of LTDs are enabled by the detection of very low energy excitations (e.g. phonons and quasiparticles). In a typical interaction, energy from an incident particle is dissipated through excitation of secondary particles such as electrons, ions, holes, photons, phonons etc. These particles will in turn produce their own secondaries. Thus there is a cascade down in energy until the original energy deposit is converted entirely into heat and the detector reaches thermal equilibrium. Prior to the equilibrium phase, the energy at any given moment is partitioned among multiple excitation modes. Conventional particle detectors work by sensing the higher energy excitation modes, such as ionization and scintillation, which require an average minimum energy of few eV to 10's of eV to produce. For such detectors, a large fraction of the deposited energy remains undetected in the form of heat. Furthermore, the measurements are subject to the fluctuations inherent in the partition of energy across different excitation modes. Secondaries that don't eventually escape the detector, will de-excite or recombine to dissipate their energy in the form of phonons and quasiparticles, which are characterized by energies in the range of meV down to μeV. These can be detected by LTDs at various stages of their final degradation towards thermal equilibrium. Thus LTDs allow for energy resolutions and operational thresholds much lower than detectors that only sense scintillation and ionization. Furthermore, LTDs provide a precise energy measurement owing to the relatively large number of excitation quanta that can be detected. In fact, LTDs designed to measure thermal phonons achieve the highest possible energy resolutions with optimal noise performance.

At thermal equilibrium, energy E deposited in an LTD causes a temperature rise $\Delta T = E/C$ where C is the heat capacity. Thermal equilibrium is characterized by the condition where the average heat flowing to an LTD equals the average heat flowing from the LTD (into a proper heat sink or bath). In this state, the ideal intrinsic energy resolution is determined by the statistical fluctuations in the phonon system. Fluctuations in the total number of phonons in the LTD absorber have variance C/k_B, which yields a minimum resolution of $\Delta E^2 = k_B T^2 C$ to the device energy resolution, where k_B is Boltzmann's constant. Thus, the smaller the heat capacity, the more sensitive the response of the calorimeter and the better the energy resolution. The most relevant feature of this result is that the latter is independent of the energy deposition. The heat capacity itself is the product of the detector volume (V) and the specific heat (c_p). Optimization of LTD response can be achieved by using small detector volumes and materials with low specific heat. Noise contributions from additional sources will increase the variance and are generally parameterized as a multiplicative factor ($\xi \gtrsim 1$) to the variance expression above.

Similarly, the power P from incident particles or radiation can be measured through a temperature rise given by $\Delta T = P/G$, where G is the thermal conductance to a weakly linked bath held at constant temperature. Power fluctuations are limited by G and have a spectral density of $S_P = NEP^2 = 4k_\mathrm{B}T^2G$, where NEP is the noise equivalent power, defined as the power in a 1 Hz bandwidth that gives a response signal with an amplitude equal to the noise. Hence lower conductance yields better sensitivities. To minimize thermal conductance in precise power measurements, weak thermal links can be realized by using thin membranes or by decoupling the electron and phonon systems. However, a compromise must be made. While lower G yields better noise metrics, conversely, larger G is needed to dissipate all incident power (which can be large in the case of CMB detectors) or to have a faster detector response (the characteristic response time being $\tau = C/G$).

LTDs that measure power are sometimes referred to as *bolometers* in literature, as opposed to *calorimeters* that measure energy, generating some confusion. In principle, there is no clear distinction between a calorimeter and a bolometer. The operation mode is generally determined by the ratio of the characteristic time constant and the average time between the arrival of incident particles or quanta [268].Yet another convention is to refer to *non-equilibrium* LTDs as those detectors that measure incident energy or power by counting excitations that have energy $\gg k_BT$. In such detectors, energy resolution is determined by the statistical fluctuations of the energy partition, similar to conventional ionization detectors but with a much lower average excitation energy and hence a larger number of excitation quanta.

Table 36.7: Low temperature dependence on temperature (T) for specific heat, based on different material classes. In the table below Θ_D is the Debye temperature and T_C is the transition temperature of the superconductor.

Heat Capacity	Material
$\propto \left(\frac{T}{\Theta_D}\right)^3$	Dielectric and diamagnetic
$\propto T$	Conductor
$\propto \exp\left(-\frac{2T_C}{T}\right)$	Superconductor
$\propto \left(\frac{\mu_B B}{k_B T}\right)^2 \mathrm{sech}^2\left(\frac{\mu_B B}{k_B T}\right)$	Paramagnet (in magnetic field **B**)

A variety of possible detector materials and sensor technologies makes LTDs very versatile and highly customizable. Dielectric, superconducting and paramagnetic materials are often used owing to the fact that at very low temperatures, the specific heat decreases strongly as a function of T (see table 36.7). Superconductors offer additional advantages: the abrupt change in resistance when a material transitions from its normal to superconducting state enables highly sensitive measures of temperature changes. Additionally, the existence of a small (less than a meV) but distinct energy gap that is required to break a Cooper pair, provides a means to measure energy deposits by counting the resulting quasiparticles (QP). QP relaxation processes are typically faster than thermal processes making these detectors suitable for high-rate photo-counting. In summary, both the sensitivity and energy resolution of an LTD benefit greatly from low temperature operation.

36.5.2 *Detector Types*

A generalized LTD calorimeter consists of an absorber in thermal contact with a phonon or quasiparticle sensor, and a thermal link to a heat bath at a constant temperature (see figure 36.11). The absorber provides the mass necessary for the interaction of the particle and a fast and complete thermalization of the deposited energy. The sensor accomplishes the task of translating the particle interaction into measurable parameters. It is generally sensitive to equilibrium phonons (e.g. thermistors and MMCs) and thus provides a precise measurement of the temperature. However, non-equilibrium (e.g. STJ's or KIDs) and mixed (e.g. TES) phonon sensors have been devised and implemented in many applications as well. The goal of the thermal link is to cool the absorber down to its equilibrium temperature after the absorption of a particle. In monolithic detectors the thermometer and absorber are identical, while in composite detectors the thermometer is attached to a separate absorber. This basic design applies to single-event particle detection as well as for

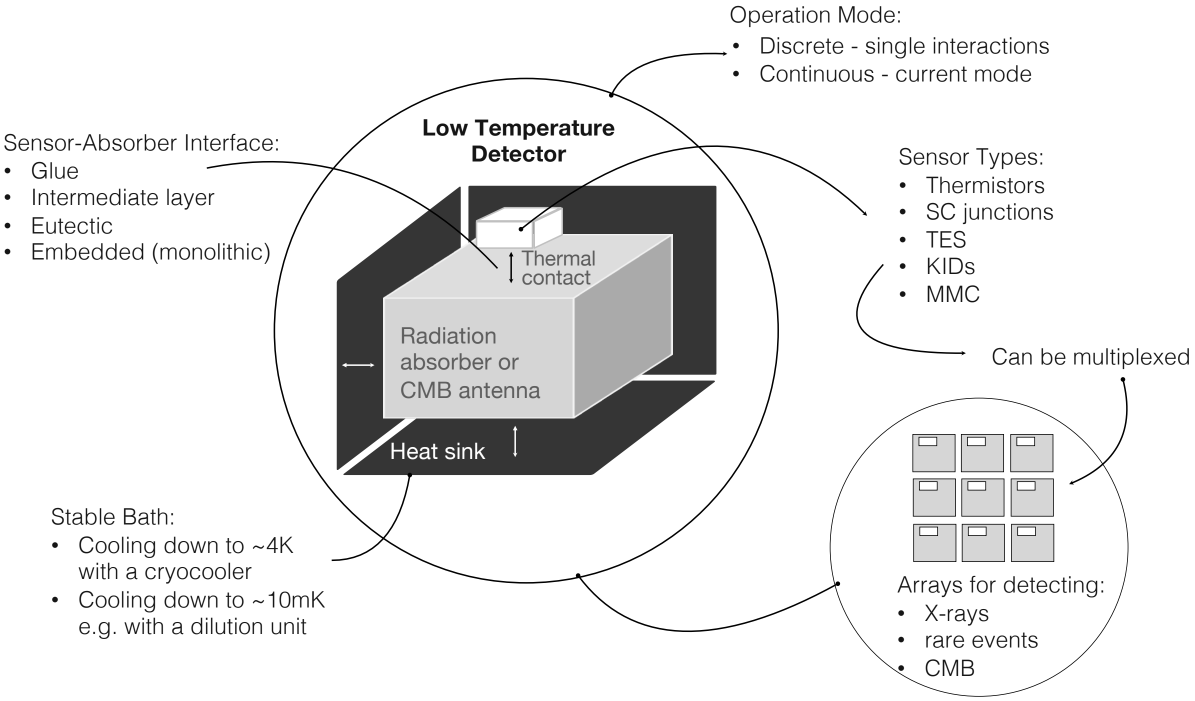

Figure 36.11: A generalized LTD consists of an absorber, a sensor and a thermal link to a stable-temperature bath. Biasing schemes and readout is described in detail in the text for individual sensor types.

continuous radiation measurement devices. In the case of the latter, a suitable absorber whose mass is irrelevant, *e.g.* an antenna at the end of a waveguide, collects the incident power and dissipates it onto a resistive (*e.g.* Au) film, which is put in contact with a sensor capable of detecting tiny temperature changes (e.g. semiconductor thermistors, transition-edge sensors, and kinetic inductance detectors, to name a few).

Superconducting Tunnel Junctions (STJs) and Kinetic Inductance Detectors (KIDs) are examples of non-equilibrium detectors. STJs exploit tunnelling of particles and QPs between two superconductors. The superconductors act as radiation absorbers, and are separated by a thin insulating layer. When such a junction is DC biased at a voltage just below the gap voltage, the excess quasiparticles generated by the incoming radiation are detected as a tunneling-current proportional to the incoming energy. Statistical fluctuations in the tunnelling process limit the energy resolution which is given by:

$$\sigma_E = \sqrt{\varepsilon(F+G)E_0}, \tag{36.5}$$

where $\varepsilon \sim \Delta$, the band-gap, while $F \sim 0.2$ and $G > 1$ are the Fano factor and tunnelling fluctuation respectively. STJs have been proven to be excellent single photon and UV-VIS spectroscopic detectors with near theoretical energy resolutions, high detection efficiencies and excellent time resolution. In astrophysics they are used as mixers to detect radiation in the 100 GHz to 1 THz range by exploiting the non-linear behaviour of their current versus voltage characteristic curve. Despite their extremely good energy resolutions, STJs cannot be scaled-up to produce sensors with large observing volumes due to readout complexity and the difficulty in uniformly suppressing the superconducting Josephson current, which is superimposed on the QP current.

Qubits share similar design elements as STJs. Using a Josephson Junction (JJ, a thin normal layer separating two superconductors) as a non-linear inductor in a superconducting LC circuit, it is possible to realize a two-level system whose status can be read out by a suitable superconducting circuit [269]. When qubits are coupled to a resonant cavity, they can be used as ultra-sensitive detectors of electromagnetic radiation, especially in the microwave regime. Incident radiation can interact with the cavity field, inducing a measurable shift in the qubit's energy levels through dispersive coupling. This interaction alters the qubit's transition frequency or induces excitation, depending on the setup, which can be read out via high-fidelity quantum measurement techniques. Similarly, qubits can be patterned onto large absorbers such as silicon or sapphire in order to detect energy depositions of less than an eV, which may arise from scatters of dark matter or neutrinos [270–272]. A particle interaction in the absorber will downconvert to sub-ballistic phonons. Those that diffuse into the JJ may tunnel across it, thus altering the qubit's state. Such qubit systems are particularly useful for detecting weak signals, such as single microwave photons or very low energy particle interactions, making them powerful tools in quantum sensing for astrophysical or dark matter detection experiments [273].

KIDs exploit the variation of the kinetic energy T stored in a superconductor by Cooper pairs whose inertia acts as an effective inductance, given by:

$$T = \frac{1}{2}nm^*v^2 = \frac{1}{2}LI^2 \tag{36.6}$$

where n is the number density of Cooper pairs, $m^* = 2m_e$ is the Cooper pair mass and $I = 2nev$ is the Cooper pair current. $L = m_e/2ne$ is defined as Kinetic Inductance and is inversely proportional to the number of Cooper pairs [274]. When a KID is placed in series with a superconducting capacitor, the resonance frequency of the circuit will be temporarily shifted by incident radiation, which converts Cooper pairs to QPs, thus changing the effective inductance. The presence and amount of radiation is observed as a change in amplitude or phase of a tuned sinusoidal signal that is sent through the circuit. In practice the change in L is small, and very high Q microwave resonance circuits are needed to sense this variation (hence the name MKIDs, for Microwave-KIDs). Furthermore, only areas of the film where large currents are flowing will be sensitive to pair breaking, thus making the response of a distributed KID position dependent. To overcome this issue, QP trapping (by coupling two superconductors with different band-gaps) is used for absorbing optical photons and X-rays. To detect lower frequencies (*e.g.* in the 100-1000 GHz range for CMB) a lumped element resonator (LEKID), with little current variation across the device, is used. The device itself, based on a series LC circuit inductively coupled to a microstrip feed line, can act as the absorber as well as the sensing element in a detector system. Macroscopic devices (few mm^2) can be fabricated by shaping the inductor in the form of a meander coupled to an inter-digitated capacitor [275]. The theoretical noise limit of these devices is governed by generation-recombination noise and takes the form:

$$NEP_{QP} = 2\varDelta\sqrt{\frac{n_{QP}}{\tau_{QP}}}, \tag{36.7}$$

where n_{QP} and τ_{QP} are the QP number and lifetime respectively. KIDs are easy to fabricate, very sensitive, broad band and easily multiplexable: they can be coupled with a single microstrip that simultaneously reads 1000s of detectors resonating at different frequencies. They provide therefore a promising solution for deploying large arrays of detectors with applications to high-energy physics, astronomy or CMB measurements, although there are still some challenges, especially at frequencies below 100 GHz, related to their worse noise performance when compared to other LTDs, and to the choice of materials with a sufficiently small energy-gap.

Semiconductor thermistors are resistive elements characterised by a strong dependence of the resistance on the temperature. Usually, they consist of small crystals of germanium or silicon with a dopant concentration slightly below the metal-to-insulator transition. However, they can also be realized in the form of amorphous films such as NbSi. At low temperatures, their resistivity (ρ) is governed by variable range hopping (VRH) conduction and is described by the expression $\rho(T) = \rho_0\ \exp\left((T_0/T)^\gamma\right)$, where T_0 and ρ_0 are parameters controlled by the doping level, while γ depends on the compensation level K (ratio of acceptor to donor concentrations). For low values of K, γ is well approximated by 1/4 while it converges to 1/2 as K increases.

Semiconductor thermistors are high impedance devices (1–100 MΩ) whose performance is usually parameterized in terms of the logarithmic sensitivity $\alpha = \mathrm{d}\log R/\mathrm{d}\log T$, typically in the range of 1–10. Silicon thermistors are fabricated using a multiple ion implantation process in high purity silicon wafers to produce a thin and uniformly doped box-like volume. The best germanium thermistors are fabricated starting from bulk, high-purity germanium crystals doped by means of neutron irradiation in the core of a nuclear reactor, referred to as nuclear transmutation doping (NTD). Individual sensors are then produced by dicing the irradiated samples and finishing them by hand. The great advantage of NTDs is the highly uniform doping level over large volumes which results in a better signal to noise ratio with respect to other doping techniques. The doping level depends on the isotopic composition of the starting material and the irradiation time.

The weak coupling to the heat sink can be provided by the electrical leads used for the read-out. However, nowadays microelectronic planar technologies and silicon micromachining are more commonly preferred, and sensors are suspended on thin silicon nitride membranes or thin silicon beams. Thermistors are read-out in an approximately constant current biasing configuration obtained by inserting large load resistors in the bias circuit, which allows for direct conversion of the thermal signal ($\varDelta$T) into a voltage signal ($\varDelta$V).

Semiconductor thermistors are very practical to use with some drawbacks. One of these is related to their high impedance which requires a JFET front-end placed as close as possible to the device in order to minimize the signal integration on parasitic electrical capacitances. This can represent a technical challenge, because JFETs must be maintained at significantly higher temperatures ($\gtrsim$100 K). Furthermore, deviations from the exponential behaviour of the conductivity have been observed at low temperatures. They are usually described in terms of a finite thermal coupling between electrons and phonons which results in an intrinsic limit to the signal rise times, which is of the order of hundreds of milliseconds at temperatures below 100 mK. Nevertheless, semiconductor thermistors are an established and robust technology, and arrays of detectors based on these devices have been widely used for neutrinoless double beta decay searches, neutrino mass measurements and X-ray spectroscopy. Energy resolutions lower than 5 eV have been achieved with Sn or HgTe absorbers.

Superconducting Transition Edge Sensors (TESs) exploit the sharp transition between superconducting and normal conducting phases, yielding a high sensitivity to temperature variations. Temperature perturbations, and hence resistance changes, are sensed as modulations in the current through the TES. TESs are operated in a constant voltage biasing configuration where Joule heating, arising from the current flowing in the TES, decreases with a rise in resistance, which then brings the TES back to its nominal operating temperature. This electrothermal feedback (ETF) is achieved by providing a TES with a voltage bias whose power, $P_J = V_{\mathrm{bias}}^2/R(T)$, heats the TES to its nominal operation point, the superconducting transition temperature. Operation in ETF mode improves linearity, speeds up response (to faster than $\tau = C/G$), and in some cases it provides tolerance for T_{C} (critical temperature) variation between multiple TESs in a large array. The low impedance in this configuration makes them well-suited for readout by SQUID (Superconducting QUantum Interference Device) based amplifiers. Logarithmic sensitivities $\alpha = \mathrm{d}\log R/\mathrm{d}\log T$ of the order of several hundreds can be achieved. By using different superconductors, or superconductor-metal pairs patterned in suitable shapes, a wide range of resistances, transition temperatures and time constants are obtainable to meet the requirements of the desired application [276].

Nano-TESs are fabricated by lithographic techniques in the form of long (few μm) and narrow (nm) wires that exhibit extremely small NEPs due to their reduced C and G, enabling single-photon sensing. Superconducting Nanowire Single-Photon Detectors (SNSPDs) are similarly patterned superconductors or superconducting bilayers maintained at a temperature well below their T_{C}. When a DC current just below the critical current is driven through the nanowire, the absorption of a single photon causes the formation of a hot spot that drives the superconductor to a normal conducting state, resulting in a very fast (tens of picoseconds) current pulse through a shunt resistor. For this reason, nano-TESs and SNSPDs are used as single photon detectors for light dark matter and axion searches in applications where large detecting mass is not critical [277].

Magnetic Metallic Calorimeters (MMC) exploit paramagnetic sensors exposed to a weak magnetic field with a weak thermal link to a heat bath. A temperature rise causes a change in the sensor magnetization, which is sensed by a SQUID magnetometer. A common material is an Au:Er mixture, with the addition of a few hundred ppm of enriched ^{166}Er, which is needed to reduce the unwanted contribution of nuclear magnetic moments of other Er isotopes. The read-out is non-dissipative and avoids the noise sources common to the dissipative devices. The use of a metallic host ensures relatively fast time response, since the typical spin-electron relaxation times are of the order of 0.1 microseconds at ∼50 mK [278]. For an optimized MMC, the energy resolution is given by $\mathit{\Delta}_E = \sqrt{2k_BT^2C}\,(\tau_0/\tau_1)^{1/4}$, where τ_0 (order of micro second) and τ_1 (order of milli second) denote the signal rising and decay times respectively [264]. In order to obtain a fast and efficient energy thermalization, MMC are typically fabricated from gold. The intrinsically large heat capacity of the paramagnet does not spoil the temperature sensitivity and allows the use of relatively large gold absorbers without degrading the device performance. Furthermore, thermal isolation from the heat sink is not generally an issue. Owing to the simple concept of these devices, MMC can be precisely customized and fabricated by employing standard microtechnology. Planar MMC arrays characterized by an excellent energy resolution, large dynamic range and good linearity have been successfully used for the detection of soft X-rays.

Performance and technological constraints limit the maximum size of LTDs. To improve overall experimental sensitivities, a large number of sensors must be deployed, typically at temperatures of a few tens of mK, where cooling power is limited to a few μW. To reduce the readout complexity and the heat load at the colder stages, multiplexing (MUX) techniques are often employed. Multiplexing consists of reading multiple detectors out through a limited number of lines that traverse room temperature to cryogenic temperatures [279]. In frequency-domain multiplexing (FDM), a tuned superconducting LC circuit is placed in series with each sensor, and a frequency comb of AC biases (usually in the MHz range) is sent to a group of sensors in parallel. A synchronous demodulation of the amplified current signal allows the recovery of the resistance variation of each detector. Microwave-multiplexing (μMUX) represents a variation of this concept, based on the usage of rf-SQUIDs, where the frequency comb is in the GHz range. Alternatively, the signal from a single detector can be recovered by readout of one detector at a time (time-domain multiplexing, TDM). KIDs have been gaining popularity owing to the fact that they naturally form resonant circuits, hence multiplexing in the frequency domain is readily achieved by adjusting their capacitance.

36.5.3 *Experimental Applications*

LTDs are sensitive over a wide range of energy, from centimetre wavelength ($\sim$ meV) through the visible spectrum ($\sim$ eV) up to the X-ray domain ($\sim$ keV) and beyond. Several broad categories of LTD applications towards measurements of fundamental physics are described in more detail in the text below and summarized in tables 36.8 and 36.9.

Bolometric detectors are favored as microwave detectors owing to their nearly constant response over frequency, playing an important role in far-infrared astronomy and in the survey of the cosmic background radiation. The high-frequency instrument of the Planck satellite (HFI) used spiderweb bolometers read by NTD-Ge thermistors, but current experiments use mainly TESs or, more recently, KIDs. Depending on the objective of the experiment, antenna coupling or absorber coupling is used. In the former case, the bolometer detects one polarization and one (or a few) modes of the radiation, while absorber-coupled bolometers do not distinguish between polarizations. In order to avoid the absorption or emission from Earth's atmosphere, many (CMB) instruments are operated by observatories located at high altitude, dry places (such as the Atacama desert or Antarctica), balloon-borne platforms, or from space. In Table 36.8, we list a subset of the ongoing or planned CMB experiments (see Section 29 of this Review for the details on present challenges).

In the Atacama Desert, CLASS continues to collect data and has recently reported large scale E-mode polarization measurements and constraints on reionization [280], while Advanced ACTPol observations (2017–2022) continue to yield new maps and cosmology results [281]. POLARBEAR-2 (PB2-A), part of the Simons Array [282]. The Simons Observatory has achieved first light and is operating [283]. At the South Pole, SPT-3G, BICEP3, and the BICEP Array remain active with new results and ongoing receiver deployments. The CMB-S4 project, initially envisioned as the next-generation ground-based CMB survey with unprecedented sensitivity and scale, has been cancelled, and the project is proceeding with an orderly shutdown. In the Canary Islands, QUIJOTE and GroundBIRD are operating, while LSPE-STRIP is nearing construction [284, 285]. In Argentina, QUBIC resumed operations in 2025 and began sky calibration [286]. In Tibet, AliCPT-1 completed its first phase and captured initial 150 GHz images of the Moon and Jupiter. Among stratospheric balloon experiments, SPIDER has flown twice (2015 and 2022/23), EBEX flew in 2012–13, and LSPE/SWIPE remains in advanced development. Finally, in space, LiteBIRD remains in development with a launch targeted for the 2030s [287], and PICO (Probe of Inflation and Cosmic Origins) has been proposed as a NASA flagship mission concept to provide complementary full-sky, high-sensitivity CMB polarization measurements.

The incoming radiation couples directly to the antenna probes (as in BICEP/Keck) or through micro-machined horn waveguides (AdvancedACT-Pol, CLASS) or lenslets (Simons Array, SPT-3G), depending on the frequency range. All of these experiments have focal planes with hundreds to hundreds of thousands of sensors. To optimize focal plane occupancy, multi-mode or multi-chroic, dual polarization sensitive detectors are used. In the former case, the sensitivity is enhanced by collecting power from a larger number of modes at the expense of angular resolution. In the latter, one single mode of the radiation is focused on a broad band antenna, and on-chip polarization separation and band-pass filters split the signal in different frequency bands directing the power to different absorbers and sensors.

Experimental design is driven by a trade-off between the sensitivity and the complexity of the production processes and readout. On the one front, single-sensor NEP at the level of 10^{-21} W/$\sqrt{\mathrm{Hz}}$ has been achieved in laboratories and research centers. Meanwhile, efforts are in place for the industrialization of the fabrication processes, which is essential for scaling up production for the large number of detectors needed for future experiments.

Massive cryogenic calorimeters have been proposed since the 1980's as particle detectors for the search of rare processes (e.g. dark matter, neutrinoless double beta decay) [288]. Almost simultaneously, the use of arrays of small mass calorimeters was suggested for X-ray astrophysics [289] and precision measurements of the neutrino mass [290, 291]. Although essential to understanding the nature of neutrinos, neutrinoless double beta decay (NDBD) has eluded discovery (or definitive exclusion) for over 50 years. Calorimeteric techniques provide the best sensitivities to NDBD. However, before the advent of low temperature calorimeters (LTC), only a few isotopes (^{48}Ca, ^{136}Xe and ^{76}Ge) could be utilized for NDBD studies with the calorimetric approach. This limitation was removed by the advancement of LTC's, and in particular by CUORE, which takes advantage of the naturally high abundance of ^{130}Te in TeO_2 crystals. Additionally, the operation of CUORE at LNGS [292] has demonstrated that the technical challenges of operating ton-sized LTD detectors in a deep, underground location are surmountable. Currently, the most promising future approach is based on the hybrid approach of scintillating LTCs, which unfortunately cannot be used for ^{130}Te. Now, new projects are being proposed based on different scintillating compounds. In particular ^{100}Mo is the choice of CUPID [293, 294] (NTD thermistors glued to $Li_2{}^{100}MoO_4$ crystals), which will use the same infrastracture of CUORE and follows from the successful operation of several demonstrators (CUPID-0 [295] and CUPID-Mo [296]), and AMORE (MMC sensors on $Ca^{100}MoO_4$ or $Li_2{}^{100}MoO_4$ crystals) [297]. With an energy resolution comparable to germanium diodes and a mass of the order of a ton, these experiments aim to probe the inverted hierarchy of neutrino masses. Extremely pure materials, careful assembly procedures, and deep underground laboratories are therefore necessary. These detectors are characterised by relatively slow responses, which still represent a major limitation for some of the proposed applications.

In the 1980's, the calorimetric technique was recognized as a feasible approach to make a direct measurement of the neutrino mass from the end-point of a beta spectrum. Thus, LTCs were proposed as a possible alternative to the standard spectrometric measurements [298]. Calorimetric measurements offer a number of advantages [299]: i) a weak dependence on the final excited states, ii) no source effects (e.g. self-absorption), and iii) lack of back-scattering from the detector. Therefore LTCs provide a faithful reconstruction of the beta spectral shape over a broad energy range below the end-point. However, the difficulty in resolving a small fraction of the spectrum near the end-point is a serious limitation that strongly constrains the source strength and the statistics that need to be accumulated. Such an inconvenience can be mitigated by selecting beta emitters

Table 36.8: Some selected experiments using LTDs to measure the CMB. These experiments constrain the physics of inflation and the absolute mass, hierarchy, and number of neutrino species. The experiment location determines the part of the sky that is observed. The size of the aperture determines the angular resolution. The table also indicates the type of sensor used, the number of sensors, the frequency range, and the number of frequency bands. Data for planned upgrades or future experiments are provided in parentheses.

Sub-K CMB Experiment	Location	Aperture	Sensor type	# Sensors (planned)	Frequency (planned)	Bands (planned)
Ground-based						
Atacama Cosmology Telescope (2007–)	Chile	6 m	TES	5, 614	30–230 GHz	5
BICEP/Keck (2006–)	South Pole	26/68 cm	TES	2,500	95–270 GHz	6
CLASS (2015–)	Chile	60 cm	TES	3,488	40–220 GHz	4
GroundBIRD (2021-)	Canary Island	30 cm	MKID	322	145–220 GHz	2
POLARBEAR / Simons Array (2012–)	Chile	3.5 m	TES	1,274 (22,764)	150 GHz (90–280 GHz)	1 (4)
South Pole Telescope (2007–)	South Pole	10 m	TES	16,260	90–220 GHz	3
Simons Observatory (2022–)	Chile	6 m/0.5 m	TES	(60,000)	(27–280 GHz)	(6)
CMB-S4 (cancelled)	Chile + South Pole	21 telescopes	TES	(500,000)	(20–280 GHz)	(11)
Balloon						
EBEX (2013–)	McMurdo	1.5 m	TES	∼1,000	150–410 GHz	3
PIPER (2016–)	New Mexico	2 m	TES	5,120	200–600 GHz	4
SPIDER (2014–)	McMurdo	30 cm	TES	1,959	90–280 GHz	3
LSPE (2026–)	Longyearbyen	60 cm	TES	(326)	(140–270 GHz)	(3)
Satellite						
Planck HFI (2003-2013)	L2	1.5 m	NTD	52	100-857 GHz	9
LiteBIRD (2030s)	L2	80 cm	TES	(4,508)	(34–448 GHz)	(15)
PICO (2040s)	L2	1.4 m	TES	(12,996)	(21–799 GHz)	(21)

with a small Q value, owing to the fact that the fraction of counts in an interval, δ close to Q, scales as $(\delta/\mathrm{Q})^3$. However, this is generally at the cost of choosing decays with more complex nuclear transitions. In addition, LTCs may be affected by specific systematics (e.g. solid state effects). Ultimately it is recognized that spectrometers and calorimeters have complicated but different systematic effects. It is therefore critical to develop complementary experiments exploiting both techniques.

LTCs were initially proposed as perfect calorimeters to measure the energy spectrum of a low Q beta emitter embedded in an absorber. However, the requirements of excellent energy resolution and a low rate (to avoid pileup) requires a very large number, $\mathrm{O}(10^4-10^6)$, of small mass devices (microcalorimeters). Early experiments used ^{187}Re, which is a long-lived beta emitter that is naturally abundant in rhenium samples and is characterised by a very low Q value (2.4709 keV [300]).

A large number of ^{187}Re based experiments have been developed over the years (MANU [301], MIBETA [302], MARE [303]). Nowadays a different approach is preferred and is based on the measurement of the atomic radiation following electron capture, typically in ^{163}Ho which is also characterized by a very low Q (2.837 keV [304]). Different experiments have been proposed to face the challenge: ECHo in Germany [305] (using MMC sensors), HOLMES in Italy [306] and NUMECS [307] in the US (using TESs). LTCs are also included in PTOLEMY's proposal, whose main purpose is to detect relic neutrinos, but which also includes an initial stage dedicated to measuring the mass of neutrinos [308]. The very large number of microcalorimeters needed to obtain sensitivities comparable to spectrometric measurements is a serious challenge, both for the readout and the thermal heat load. An alternative readout based on the use of KIDs, for their multiplexing capability, has been proposed and is presently under development.

Traditional searches for WIMP-like dark matter aim to measure the scatter of a massive (>10 GeV/c^2) dark matter particle off of a target nucleus. Similar to detectors employed for neutrinoless double beta decay, these searches benefit from large-mass absorbers for the target because the dark matter interaction rate scales directly with the number of nuclei in the target and hence its mass. Among the most successful experiments to date, are those that combine the detection of phonons with another channel such as ionization energy (EDELWEISS [309] and SuperCDMS [310]) or scintilation light (CRESST [311]). This simultaneous, dual measurement takes advantage of the fact that the energy deposited in the absorber is partitioned into these channels differently depending on whether the initial particle interaction produces electron or nuclear recoils (or both). This particle identification allows for the rejection of background from natural sources of radiation, which most commonly manifest themselves as electron recoils in the detector.

In recent years, multi-ton liquid noble detectors have outclassed LTD-based technologies in searches for heavy dark matter owing to their ability to more easily and cheaply scale to large target masses. However, the lower thresholds achieved by LTDs continue to make them the technology of choice for low-mass dark matter searches. New advances have enabled these detectors to reach much lower energy thresholds than previously obtained, albeit sometimes at the cost of being able to detect energy in more than one channel as described above. For example, the use of an electric field to generate Neganov-Trofimov-Luke [317, 318] phonons in proportion to the applied voltage, has enabled the detection of single electron hole pairs in detectors with thresholds as low as a few eV (SuperCDMS HVeV [319], EDELWEISS_SubGeV [320]) and is proposed for the CUPID light detectors [321]. These advances have enabled sensitive searches for dark photons and dark matter that scatters off electrons. Next generation experiments such as TESSERACT aim to further optimize the intrinsic energy resolution of TES detectors, coupled with a strategic choice of target materials (He, GaAs) to enable sensitivites to dark matter with masses below an MeV/c^2 [322]. KIDs can be also applied to readout silicon dice to be sensitive to GeV DM, as in the BULLKID [323] proposal. Current state-of-the-art axion searches use SQUID based quantum amplifiers such as Josephson Parametric Amplifiers along with resonant cavities operating below 100 mK to look for a signal above fluctuations in the thermal noise [324,325]. Future axion experiments are also working to close the sensitivity gap between particle and wave-like dark matter with the help of LTDs. Broad-band axion searches in the THz range are being proposed, which will make use of TES, SNSPDs or KIDs for single photon detection [326]. Finally, LTD-based dark matter detectors are also actively employed to study coherent neutrino scattering, owing to the fact that the hypothesized signal from dark matter-nucleus scattering is nearly identical to that from neutrino-nucleus scattering, with both inducing nuclear recoils in a similar energy range [327–330].

Table 36.9: Selected experiments using low temperature calorimeters. The table shows currently or soon-to-be operating experiments that will search for dark matter or neutrino properties. The dates refer to the start of the program.

Sub-K Experiment	Location	Detection mode	Absorber (Total mass)	Sensor type	# Sensor # Crystal
WIMPs					
CRESST [312] (upgrade 2026)	LNGS Italy	Athermal phonon and scint.	$CaWO_4$, Al_2O_3, Si, $LiAlO_2$	TES	variable
SuperCDMS (2025)	SNOLAB Canada	Athermal phonon and ion.	Ge/Si	TES	24
TESSERACT† (2029)	LSM Modane France	Athermal phonon quantum evaporation	GaAs, He, Si, Ge	TES	-
Neutrino mass					
ECHo [305] (2012)	Heidelberg Germany	Thermal phonon	Au:^{163}Ho (0.2μg)	MMC	16
HOLMES [306] (2015)	Milan Italy	Thermal phonon	implanted ^{163}Ho ($18\ \mu$g)	TES	1000
NUMECS† [307] (2015)	LANL USA	Thermal phonon	implanted ^{163}Ho	TES	4096
$0\nu\beta\beta$ **decay**					
CUORE [313, 314] (2015)	LNGS Italy	Thermal phonon	$^{nat}TeO_2$ (741 kg)	NTD Ge	988
CUPID [294] (2015)	LNGS Italy	Phonon and scint.	$Li_2^{100}MoO_4$ (450 kg)	NTD Ge	1596
AMoRe-I [315] (2022)	Y2L South Korea	Phonon and scint.	$Ca^{100}MoO_4/Li_2{}^{100}MoO_4$ (6.2 kg)	MMC	18
AMoRe-II [316] (2026)	Yemilab South Korea	Phonon and scint.	$Li_2{}^{100}MoO_4$ (157 kg)	MMC	360

†No payload size quoted for experiments that are primarily in R&D or design phase.

36.6 Low-radioactivity background techniques

Revised October 2025 by Al. Ianni (INFN, LNGS) and S. Schönert (TU Munich).

36.6.1 *Introduction*

The study of rare phenomena in fundamental physics, such as proton decay, neutrinoless double beta decay, dark matter, and MeV-scale neutrino interactions, requires extremely low levels of background radiation. Experiments searching for these rare events record electron recoils or nuclear recoils in the energy scale from a few eV to several MeV. The detector technologies used are multiple from organic and cryogenic liquid scintillators, to bolometers, solide state calorimeters, gaseous detectors, and crystal scintillators. As far as the background contamination is concerned at some extent the application defines the requirements, although the common denominator is that an extreme reduction of all background sources is essential. Leading experiments in rare events search have obtained in the region-of-interest (ROI) a background as low as $\sim 10^{-4}$ cts/kg/y/keV. As a first and crucial step, a dedicated radio-purity assay of the detector set-up components has to be carried out. Over the last fifty years, special screening and cleaning techniques have been developed to measure and mitigate ultra-low levels of background. In order to characterize the background sources we refer to Heusser [331] and identify the following five main categories:

- environmental radioactivity in the location where the detector is installed;
- radioimpurities in the detector and shielding;
- radon and its progenies;
- cosmic rays and induced radioactivity;
- neutrons from natural fission, (α,n) reactions, and from cosmic-ray muons interactions.

The energy range affected by these background sources is mainly $<$10 MeV. All materials contain traces of long-lived primordial radioimpurities, such as ^{238}U, ^{232}Th, ^{235}U (^{238}U/^{235}U ~ 138), and ^{40}K (^{40}K/K$^{nat} \sim 1.17 \times 10^{-4}$). We recall that 1 *ppt* of ^{238}U and ^{232}Th corresponds to 12.36 and 4.06 μBq/kg, respectively; 1 *ppb* of K^{nat} corresponds to 30.25 μBq/kg. In the Earth's crust the abundance of uranium and thorium is of the order of $1-10$ ppm which corresponds to about $10-100$ Bq/kg. Taking into account these contamination levels and the low background requirements, a fundamental background reduction and mitigation is essential to carry out rare phenomena research.

Besides primordial radionuclides other radioactive elements are produced through interactions with matter of secondary cosmic ray particles. Among these so-called cosmogenic radionuclides we recall, in particular, ^{3}H, ^{14}C, ^{7}Be, ^{39}Ar, ^{42}Ar , and, in copper, steel and iron often used as shielding materials, ^{57,60}Co.

A third category of background source in our environment consists of anthropogenic radionuclides. These are artificially produced mainly through nuclear reactions in nuclear power plants, nuclear fuel reprocessing plants, and nuclear weapons testing. Anthropogenic background elements of concern for rare phenomena are ^{85}Kr, ^{137}Cs, ^{241}Am, ^{60}Co, and ^{90}Sr. The concentration of ^{85}Kr ($T_{1/2}$=10.76 y, Q_β=687 keV) in air has been slowly increasing since World War Two with a present activity of order 1 Bq/m^3. As a consequence ^{85}Kr is a crucial background in experiments making use of nitrogen, xenon, and argon from air.

Once detector components radioactive backgrounds have been assayed and reduced by a careful selection campaign, which can last several years, a further step to push the background level beyond the screening possibilities is needed to reach the required sensitivity. For this purpose special active vetos, purification methods, and offline analyses have been developed. A meticulous background understanding and mitigation is crucial to explain any possible signal excess which may be detected. Background mitigation techniques are based on:

- use of radio-pure materials that absorb ionizing radiation;
- identify radio-pure material for detector construction;
- perform advanced surface and sub-surface cleaning treatment;
- reduce muon flux with underground detector deployment and using active vetos;
- exploit advanced detection and tagging techniques to discriminate signal from background.

In the following we describe radio-assay and background mitigation techniques developed and exploited in the framework of rare phenomena searches in deep underground laboratories.

36.6.2 *Radio-purity assay*

The radio-purity assay of detector components is a basic prerequisite to be carried out in low counting experiments. Several techniques are exploited for radio-purity assay. They are complementary to characterise the radio-purity of materials for shielding or core detector components. Next generation experiments radioassay campaign requires a considerable effort and organization for several years [332–335].

Gamma spectroscopy (GS) via high purity germanium (HPGe) detectors is a powerful and crucial technique [331]. It is nondestructive and thanks to the energy resolution allows to distinguish various radionuclides elements. Radiation from ^{238}U and ^{232}Th comes with all decay products in the radioactive chains. However, if secular equilibrium is broken, this crucial information can be addressed by separating different gamma-ray lines characterizing elements in the decay chains. In the ^{238}U chain one can have three sub-chains out of equilibrium. The first sub-chain can be assessed through ^{234}Th direct progeny of ^{238}U. The second sub-chain, which originates from ^{226}Ra, can be probed by ^{214}Pb and ^{214}Bi. A third sub-chain, which starts from ^{210}Pb, cannot be efficiently probed by GS, yet is of crucial importance and alternative methods must be used. In the ^{232}Th chain again one can probe two sub-chains which can be out of secular equilibrium: the first one through ^{228}Ac from ^{228}Ra; the second from ^{228}Th can be measured through ^{212}Pb, ^{212}Bi and ^{208}Tl. The technology for HPGe operated in deep underground counting facilities [336,337] or in shallow laboratories with an efficient active veto shielding [338] has been boosted to sensitivities of the order of 10-100 μBq/kg by carefully selecting detector components, electronics and sample handling systems. The HPGe screening method requires order of $\sim$ 0.1-a few kg of material, and weeks of acquisition to produce a reliable measurement.

A second crucial technique is based on inductively coupled plasma mass spectrometry (ICP-MS) [339]. This technique can probe primordial parent activities at the level of 1 μBq/kg. It is a destructive method and often needs special sample preparation on a small quantity of material. The ICP-MS does not measure the radioactive decay of isotopes but determines their concentration. At present, it is the most sensitive and rapid screening technique which allows to select materials at sub-ppt level of impurities. The drawback is that ICP-MS cannot assess whether the uranium and thorium chains are out of equilibrium and to reach ultra-high sensitivities one needs to carefully prepare and handle the samples in a cleanroom environment. ICP-MS screening must be coupled with other methods to properly assess the radio-purity of materials in the context of rare events searches. The Glow Discharge Mass Spectroscopy (GDMS) is a trace element analysis technique somehow alternative to ICP-MS. An advantage of GDMS is the possibility to determine the bulk composition of the sample, assuming homogeneity. Sensitivities of the order of 10 ppt can be achieved.

A third screening technique is based on neutron activation analysis (NAA) [340]. A sample exposed to a neutrons flux can be activated to form radioactive isotopes which can be detected using HPGe detectors or ICP-MS. Considering the difficulties to irradiate samples, this method is less often used. NAA can probe sensitivities at the level of 0.01 μBq/kg.

In case out of secular equilibrium conditions are measured for uranium and thorium from GS screening, a rigorous assessment cannot avoid radon emanation measurements. This matter is discussed in Section 36.6.3.

Complementarity between radio-purity assay techniques is a crucial parameter to design detectors for rare phenomena searches. As it has been pointed out above, requirements can be more stringent than the best sensitivity which can be obtained with the current radioassay techniques. In these cases, a number of prototype detectors have been built and operated to prove the feasibility to reach ultra-low backgrounds.

36.6.3 *Radon and its progeny*

Radon is considered to be rare in nature because most of its isotopes are short-lived. However, ^{222}Rn ($T_{1/2}$=3.82 d) is of particular concern in our context. ^{222}Rn is produced by ^{226}Ra and is a radioactive noble gas which can move within active detector components. ^{222}Rn daughters are heavy metals which can deposit on surfaces. Diffusive ^{222}Rn, supported by ^{226}Ra, can deposit on surfaces the long-lived ^{210}Pb, which is a major concern for low counting experiments. In addition, due to

$\sim$100 keV nuclear recoil energies from alpha decays in the ^{226}Ra sub-chain, eventually ^{210}Pb can be implanted into a sub-surface layer of a material exposed to radon. This sub-surface contamination can remain even after surface cleaning. Surface contamination of ^{210}Pb is a serious background for direct dark matter experiments through alpha decay of ^{210}Po, which can generate neutrons by (α,n) reactions. Low energy beta/gamma emissions from ^{210}Pb are also a concern. Therefore, radon-free cleanrooms are essential for the assembly of the detector components. Effective radon abatement systems are available for this purpose. Air at the level of 1 mBq/m^3 of ^{222}Rn can be produced with such systems.

In assembling and commissioning rare events experiments, special care must be dedicated to the estimate of radon emanation of the materials and continuous radon monitoring. For this purpose different methods for radon assay have been developed and exploited since the beginning of solar neutrino observations. ^{222}Rn atoms are collected inside an exhalation chamber for several half-lives before adsorption and counting. Detection limits of the order of 100 μBq (about 50 ^{222}Rn atoms) can be obtained with $\sim$50 l stainless steel electro-polished chambers [341]. This limit can be pushed down to 30 μBq for 1-liter scale chamber. Emanation of large vessels (cryostats, storage tanks, purification columns) can be determined by collecting exhaled radon into transportable charcoal traps [342]. The same method can be used for liquid samples. In this case instead of evacuating the exhalation chamber into a charcoal trap, He is flushed through a sparger tube for about 10 times the volume of the liquid used. Sensitivities of the order of 10 μBq/kg have been reached. A novel technique of Rn emanation measurement developed in the framework of nEXO allows continuous gas transport and detection in a recirculation gas loop with an electrostatic chamber [343]. Another innovative method has been developed by using cryogenic physisorption traps [344]. Surface treatments can be exploited to enhance significantly the emanation measurement sensitivity and surface treatment with epoxy coating or covering it with alluminized Mylar is also shown to reduce emanation [345].

Nitrogen or synthetic air is often used in rare events experiments for purging, stripping, and assembling the experimental apparatus. These gases might contain radon. In gases ^{222}Rn can also be detected using electrostatic collection of ^{218}Po and ^{214}Po [346, 347]. Sensitivities of the order of mBq/m^3 can be obtained. In Borexino three grades of nitrogen purity were used: regular purity, high purity, and low argon and krypton purity. The regular purity is obtained from boil-off gas and has radon, measured with the method reported above, at the level of $< 100\mu$Bq/m^3. For nitrogen stripping the purified liquid scintillator a higher purity is needed. To remove radon from regular purity nitrogen a dedicated absorber plant has been built. This system can reduce radon by a factor of 100. Finally, we mention that not only radon is found in nitrogen. For specific applications the long-lived ^{39}Ar and ^{85}Kr in nitrogen are an important source of background.

36.6.4 *Surface backgrounds*

Surface contamination of long-lived ^{222}Rn daughters can be challenging in low-counting experiments. Considering required sensitivities of the next generation experiments, this source of background has to be properly quantified and mitigated. Therefore, exposure to ^{222}Rn should be monitored and limited to reduce build-up of ^{210}Pb on surfaces. In addition, ^{222}Rn exposure could also produce sub-surface contamination as discussed in Section 36.6.3. For one cannot avoid radon contamination in many circumstances during production of detectors components, it is crucial to quantify the effectiveness of cleaning aiming at removing surface contamination of ^{210}Pb, ^{210}Bi, and ^{210}Po. Depending on material, progeny are deposited deeper into the subsurface. A simple cleaning procedure, which implies degreasing, wiping, and rinsing the material surfaces is not effective in removing these surface contaminants. Studies of cleaning procedures have been carried out exposing stainless steel, copper and other materials (PTFE a common used material) to a strong radon source. Etching, leaching, and electropolishing with subsequential passivation and rinsing have been investigated in great details. Several recipes have been proposed [348, 349]. Electropolishing has been shown to be very effective in reducing ^{210}Pb, ^{210}Bi, and ^{210}Po from both copper and stainless steel by a factor greater than 100. Etching, which is easier to perform than electropolishing, followed by passivation and rinsing with deionized water is effective in reducing ^{210}Pb and ^{210}Bi by a factor between 50 and 100. However, it is less effective for ^{210}Po, which in copper is very poorly reduced. Removing ^{210}Po from surfaces is crucial, therefore, naturally ^{210}Po contaminated copper and stainless steel surfaces have been deeply investigated with a high sensitivity ($1\,\mathrm{mBq/m^2}$) alpha spectrometer [350]. After multi-etching steps (≥ 3), followed by a passivation, a reduction of order 100 has been obtained. On the contrary, static etching (single step) is poorly effective. Electropolishing, or multi-etching are recommended in case copper is in direct contact with the active core of the detector and ultra-high radio-purity is essential or when copper electroforming cannot be used. Electroplating of a thin layer of high radio-pure copper onto the surface of less radio-pure copper has also been investigate to mitigate surface background [350]. This technique is shown to be efficient in reducing surface activity of ^{210}Po when electroformed copper is used [350].

Besides copper and steel other materials often used, such as polyethylene and teflon, have been investigated to understand how to reduce radon plate-out contaminations [351].

As far as surface contamination is concerned particulate fallout in cleanroom environments could be of concern. In general, chemical composition of dust reflects local composition of soil and dust. This is not necessarily true in cleanroom spaces, where the composition of dust depends on ongoing activities and handled materials [352]. The rate of fallout is an important information in the framework of rare events experiments, where assembling is performed in cleanrooms. The ^{210}Pb contamination, inferred from stable lead measured by ICP-MS, due to dust fallout has been investigated [352]. This contamination has a different origin with respect to ^{210}Pb from radon progeny implantation. Ultimately, one can conclude that radon exposure is more crucial than dust fallout. Therefore, the best practice for rare events experiments to face surface background contamination is to perform cleaning and assembling in a radon-free cleanroom environment.

36.6.5 *Mitigation of backgrounds and active background discrimination*

In this Section we discuss a selection of different background mitigation techniques used in experiments to search for rare events in deep underground laboratories. This includes both the avoidance or reduction of specific radioactive contamination, as well as active background suppression techniques based on specific event features and topologies.

- *Mitigation of ^{222}Rn daughters deposition.* In dark matter direct search radiogenic (α,n) reactions due to radioactive decays are of great concern. The emitted neutron can mimic a nuclear recoil induced by a dark matter particle interaction. In the DarkSide-50 and LUX-ZEPLIN (LZ) experiments to mitigate this background, cleaning of parts and assembling of the dual-phase Time Projection Chamber have been carried out in a radon-free cleanroom with ^{222}Rn activity of the order of $\lesssim 50\,\mathrm{mBq/m^3}$.
- *Underground argon.* Liquid argon is an excellent scintillator to search for dark matter interactions due to the high electron-recoils rejection power through pulse shape discrimination. Events from $\beta-\gamma$ background can be rejected at the level of 10^7 or better with respect to nuclear-recoils. Liquid argon is very effective as active shield and has been used in experiments for neutrinoless double beta decay. However, a major drawback for dark matter search using argon as a target is due to the fact that atmospheric argon contains about 1 Bq/kg of cosmogenic ^{39}Ar ($T_{1/2}$=269 y, Q_β=565 keV) [353]. For neutrinoless double beta decay search using argon as an active veto, ^{42}Ar ($T_{1/2}$=32.9 y, Q_β=599 keV) with its short lived progeny

^{42}K ($T_{1/2}$=12 h, Q_β=3525 keV) is a major source of background. ^{39}Ar limits significantly the dark matter and ^{42}Ar the neutrinoless double beta decay sensitivity search. Therefore, a source of argon with reduced ^{39}Ar and ^{42}Ar is crucial. Centrifugation or differential thermal diffusion are established methods to separate $^{39/42}$Ar and ^{40}Ar. However, this is an expensive method for a large fiducial mass. Argon from underground natural gas reservoirs is shown to contain low ^{39}Ar [354], and it is expected that ^{42}Ar is similar or even strongly reduced. Therefore, the use of underground argon mitigates the $^{39/42}$Ar backgrounds. DarkSide-50, with a mass of 150 kg of underground argon, has shown that this source of argon contains ^{39}Ar at a level reduced by a factor of $(1.4 \pm 0.3) \times 10^3$ with respect to atmospheric argon [355]. DarkSide-20k and LEGEND-1000 are planning to exploit underground argon from the Urania facility with a production capacity of order 300 kg/day [356]. The former to reduce ^{39}Ar and the latter ^{42}Ar.

- *Electro-formed copper.* High radio-purity copper is often used as shielding and as core detectors components. The radioimpurities in the copper can be a dominant source of external background. Copper electro-forming is a technique used to reduce this background component in rare events experiments. Copper electro-forming is a well known process to obtain ultra-high radio-purity copper. This technique has been used in the framework of the Majorana and LEGEND-200 experiments to search for neutrinoless double beta decay and in ANAIS to search for dark matter annual modulation. Sub-ppt levels in uranium and thorium have been achieved with electro-formed copper [334, 357].
- *Background suppression using topological event information.* In addition to rigorous selection of high-purity target and shielding materials from external radiation, additional active suppression techniques must usually be employed in low background experiments to achieve the appropriate experimental sensitivities. While signal and background events may be indistinguishable if only their energy deposition is measured, their event features may differ significantly in time and space. Liquid scintillators use the characteristic photon emission time distributions to distinguish between electron- and alpha-like signals [358] and nuclear recoils [359], respectively. High-purity germanium detectors use the time evolution of the induced charges to separate point-like signal candidates for neutrinoless double-beta decay events from background signals induced, for example, by gamma interactions with multiple interactions within a crystal, or from β or α events on the n+ or p+ electrodes [360]. The operation of bare high-purity germanium detectors in an instrumented liquid argon shield enabled the GERDA and LEGEND experiments to identify backgrounds with signal-like event topology within the HPGe detectors, but with characteristic energy deposition in the surrounding liquid argon. These synergistic background suppression techniques enabled for a first time ever a quasi background-free search for neutrinoless double beta decays with GERDA [361] and LEGEND-200 [362].

  EXO-200 [242] exploited topological event information distinghuishing single-site against multi-site events with a liquid xenon TPC for neutrinoless double beta decay in ^{136}Xe to reject background and threby enhancing signal discovery sensitivity. With a gas xenon TPC the NEXT experiment will fully exploit the differences in the spatial ionization patterns of double beta decay and single electron events [363]. The former is characterized by two Bragg peaks at opposite ends of the tracks, the latter on the contrary displays only one peak. The combination of topology information and good energy resolution offer a powerful tool for background rejection. In general, the 3D reconstruction of detected events in a multivariate fit, which accounts for spacial surface and bulk distributions of signal and background together with other properties, such as pulse shape and topological features, is a powerful tool for background mitigation [364].

- *Signal selection in direct Dark Matter experiments.* In direct dark matter experiments electron recoil events have to be mitigated with respect to nuclear recoil events. In semiconductor bolometers, operating at a few tens of mK under a bias electric field and used as calorimeters, drifting charges produce a large phonon signal proportional to the ionization, which allows to discriminate electron recoils by the combination of charge and phonon signals [365]. In scintillating bolometers the phonon and light signals are used for the same purpose [366]. Cryogenic scintillators, such as xenon and argon, in time projection chambers offer a strong electron recoils background mitigation through the detection of a primary scintillation signal in liquid and a secondary signal in gas from the drift and extraction of ionization electrons. This background mitigation technique is also being used for neutrinoless double beta decay with ^{136}Xe. The accurate fiducialization and good rejection of multiple-scattering events allow dark matter optimized experiments to attempt a search for this very rare phenomenon.
- *Neutron tagging.* Present and next generation experiments need large neutron tagging detectors. In DarkSide-50 a dedicated active veto has been developed to both suppress and measure *in situ* the rate of neutron-induced background events [367]. The detector consisted of a boron-loaded liquid scintillator, which served both as shielding against γ-rays and as a tag for neutrons. Neutrons are thermalised and captured on ^{10}B. Experimental data has shown a neutron rejection power greater than 99.1% with 5% concentration of TMB in 30 tonnes pseudocumene-based liquid scintillator. The LZ direct dark matter detector with a central TPC of 7 tonnes of liquid xenon makes use of an outer Gd-loaded liquid scintillator neutron tagging veto, which works similarly to the DarkSide-50 veto, replacing boron with gadolinium. The 22 tonnes liquid scintillator is based on linear alkyl benzene (LAB) as solvent. This detector has been designed to operate with a neutron tagging efficiency greater than 95%. The nuclear-recoil background is reduced by a factor of 10. The XENONnT detector is making use of a cylindrical stainless steel tank filled with Gd-loaded water, which surrounds the cryostat with a TPC of 5.9 tonnes of active liquid xenon. The Gd concentration in water is 0.2% in mass. Neutrons leaving the TPC volume will be moderated and captured by the Gd with a probability of 91%. The gamma-rays emitted after the capture are detected from Cherenkov photons, providing a neutron tagging [368]. When operated with only demineralized water the efficiency for detecting neutrons is (82±1)% [369].

  Neutron tagging techniques are also crucial for coherent neutrino-nucleus elastic scattering detection from pion-decay-at-rest neutrino source at spallation sources [370, 371]. Neutrons can be produced in the Pb shielding from CC and NC interactions and propagate into the nuclear recoil sensitive volume, generating a beam-related background. Careful shielding design and implementation of neutron tagging is crucial.
- *Mitigation of cosmogenic background.* In recent years the required sensitivity to search for dark matter and neutrinoless double beta decay asks for a strong reduction of cosmogenic background. Muons can produce neutrons that can enter the active volume of the detector from the surrounding rock or from external detector components. The yield of these so-called *cosmogenic neutrons* depend on the muon energies and the material properties of the medium the muon passes through. In addition, muons can produce by spallation radioisotopes inside the detector active volume. Cosmogenic backgrounds are a function of depth and experimental design, and can limit the sensitivity to search for rare events. Most of these radioisotopes are short-lived and their effect can be easily removed by an active veto based on the time correlation with a crossing muon. However, a number of cosmogenic radioisotopes are long-lived and they require an important consideration. Mitigation of these cosmogenic backgrounds

produced in-situ deep underground are a major challenge for upcoming and future experiments. Optimizing the detector design and analysis strategies at a given depth equals an effective muon flux reduction. In particular, we mention two discrimination techniques for muon-induced isotopes: 1) ^{11}C tagging by a three-fold coincidence between the crossing muon, the capture of the ejected neutron from ^{12}C, and the ^{11}C decay [372]; 2) similar delayed coincidence tagging can be exploited to mitigate the background due to ^{77}Ge and its metastable state ^{77m}Ge, which have been identified as dominant cosmogenic background in the search for neutrinoless double beta decay of ^{76}Ge [373].

- *Purification.* A number of high efficiency specific purification methods have been developed for different detectors in order to remove long-lived radio-isotopes, ^{39}K, ^{85}Kr, and ^{210}Pb progeny. For organic liquid scintillators, distillation and water extraction have been shown to be very effective to reach radiopurity levels of the order of $10^{-5}\mu$Bq/kg or better in uranium and thorium, and $10^{-3}\mu$Bq/kg in ^{210}Pb [374]. Distillation has been used to reduce ^{85}Kr in xenon by a factor of 10^3 [375]. Cryogenic distillation can be used to reduce the isotopic abundance of ^{39}Ar in argon extracted from underground with a 350 m column in the ARIA project [376]. Cryogenic distillation has been used in XENONnT to reduce online radon reaching a level of order 1 μBq/kg in the inner 5.9 tonne of liquid xenon [233]. For semiconductors [377] and scintillating crystals [378] zone-refining followed by single-crystal growth has been exploited to remove impurities at the cost of a small fraction of material kept after the purification.
- *Direct isotope tagging.* In neutrinoless double beta decay in order to explore half-lives greater than 10^{28} y one needs an almost background-free detector. The most robust signature is the identification of the daughter atom in the decay: for example, for ^{136}Xe, the ^{136}Ba^{2+}. Important step forwards to establish a valid and promising method for this tagging have been recently made [379, 380].

References

[1] A. Aab *et al.* (the Pierre Auger Collaboration), Earth and Space Science **7**, 4, e2019EA000582 (2020), URL `https://agupubs.onlinelibrary.wiley.com/doi/abs/10.1029/2019EA000582`.

[2] S. Bacholle and the EUSO Collaboration, The Astrophysical Journal Supplement Series **253**, 2, 36 (2021), URL `https://doi.org/10.3847/1538-4365/abd93d`.

[3] R. M. Baltrusaitis *et al.*, Nucl. Instrum. Meth. **A240**, 410 (1985).

[4] D. J. Bird *et al.* (the HiRes Collaboration), Astrophys. J. **424**, 491 (1994).

[5] T. Abu-Zayyad *et al.* (the HiRes Collaboration), Nucl. Instrum. Meth. **A450**, 253 (2000).

[6] A. Watson, European Phys. J. Web of Confs. **210**, 00001 (2019), [arXiv:1901.06676].

[7] P. Sokolsky, European Phys. J. Web of Confs. **283**, 01003 (2023).

[8] H. Tokuno *et al.*, Nucl. Instrum. Meth. **A676**, 54 (2012), [arXiv:1201.0002].

[9] J. Abraham *et al.* (the Pierre Auger Collaboration), Nucl. Instrum. Meth. **A620**, 227 (2010), [arXiv:0907.4282].

[10] A. Coleman *et al.*, Astroparticle Physics **149**, 102819 (2023), ISSN 0927-6505, URL `https://www.sciencedirect.com/science/article/pii/S0927650523000051`.

[11] M. Malacari *et al.* (the FAST Collaboration), Astroparticle Physics **119**, 102430 (2020), ISSN 0927-6505, URL `https://www.sciencedirect.com/science/article/pii/S0927650520300037`.

[12] Y. Tameda *et al.* (the CRAFFT Collaboration), in "Proc. 38th Int. Cosmic Ray Conf. (ICRC 2023)," 329 (2023), [arXiv:2309.03325].

[13] F. Arqueros, J. R. Hoerandel and B. Keilhauer, Nucl. Instrum. Meth. **A597**, 23 (2008), [arXiv:0807.3844].

[14] F. Arqueros, J. R. Hoerandel and B. Keilhauer, Nucl. Instrum. Meth. **A597**, 1 (2008), [arXiv:0807.3760].

[15] J. Rosado, F. Blanco and F. Arqueros, Astropart. Phys. **34**, 164 (2010), [arXiv:1004.3971].

[16] M. Ave *et al.* (the AIRFLY Collaboration), Astropart. Phys. **28**, 41 (2007), [arXiv:astro-ph/0703132].

[17] J. Rosado, F. Blanco and F. Arqueros, Astropart. Phys. **55**, 51 (2014), [arXiv:1401.4310].

[18] J. H. Boyer *et al.*, Nucl. Instrum. Meth. **A482**, 457 (2002).

[19] J. T. Brack *et al.*, Astropart. Phys. **20**, 653 (2004).

[20] B. Fick *et al.*, JINST **1**, 11, P11003 (2006).

[21] J. Abraham *et al.* (the Pierre Auger Collaboration), Astropart. Phys. **33**, 108 (2010), [arXiv:1002.0366].

[22] P. Abreu *et al.* (the Pierre Auger Collaboration), Astropart. Phys. **34**, 368 (2011), [arXiv:1010.6162].

[23] R. Thalman *et al.* Journal of Quantitative Spectroscopy and Radiative Transfer , **147**, 171 (2014), Erratum-ibid. **189**, 281 (2017).

[24] Abraham, J. *et al.* (the Pierre Auger Collaboration), Nucl. Instrum. Methods **A789**, 172 (2015).

[25] M. Unger *et al.*, Nucl. Instrum. Meth. **A588**, 433 (2008), [arXiv:0801.4309].

[26] Gaisser, T. K. and Hillas, A. M. *Proc. 15th Int. Cosmic Ray Conf.* Bulgarska Akademiia na Naukite, Conf. Papers **8**, 353 (1978), (archived at http://adsabs.harvard.edu/abs/1977ICRC....8..353G).

[27] A. Aab *et al.* (the Pierre Auger Collaboration), Journal of Cosmology and Astroparticle Physics **2019**, 03, 018 (2019), [arXiv:1806.07422], URL `https://dx.doi.org/10.1088/1475-7516/2019/03/018`.

[28] A. Aab *et al.* (the Pierre Auger Collaboration), Phys. Rev. D **100**, 082003 (2019), URL `https://link.aps.org/doi/10.1103/PhysRevD.100.082003`.

[29] A. Abdul Halim *et al.* (the Pierre Auger Collaboration), "Astrophys. J. Suppl." **264**, 2, 50 (2023).

[30] A. Abdul Halim *et al.* (the Pierre Auger Collaboration), Phys. Rev. Lett. **132**, 021001 (2024), URL `https://link.aps.org/doi/10.1103/PhysRevLett.132.021001`.

[31] A. Abdul Halim *et al.* (the Pierre Auger Collaboration), The Pierre Auger Observatory Upgrade – Preliminary Design Report (2016), [arXiv:1604.03637].

[32] T. Huege *et al.* (the Pierre Auger Collaboration), in "Proc. 39th Int. Cosmic Ray Conf. (ICRC 2025)," (2025), [arXiv:2507.08500], URL `https://arxiv.org/abs/2507.08500`.

[33] P. A. Klimov *et al.*, Space Sci. Rev. **212**, 3-4, 1687 (2017), [arXiv:1706.04976].

[34] B. A. Khrenov *et al.*, Cosmic Research **58**, 5, 317 (2020).

[35] G. Abdellaoui *et al.* (the JEM-EUSO Collaboration), Journal of Instrumentation **13**, 5 (2018), ISSN 17480221.

[36] G. Abdellaoui *et al.* (the JEM-EUSO Collaboration), Astroparticle Physics **154**, 102891 (2024).

[37] J. Eser *et al.* (the JEM-EUSO Collaboration), Proceedings of Science **444**, 397 (2023).

[38] G. Filippatos *et al.*, arXiv preprint (2024), [arXiv:2406.13673], URL `https://arxiv.org/abs/2406.13673`.

[39] F. Capel *et al.*, Advances in Space Research **62**, 2954 (2018).

[40] A. V. Olinto (the POEMMA Collaboration), Journal of Cosmology and Astroparticle Physics **2021**, 06, 007 (2021), URL `https://dx.doi.org/10.1088/1475-7516/2021/06/007`.

[41] J. F. Krizmanic *et al.* (the POEMMA Collaboration), POEMMA (Probe of Extreme Multi-Messenger Astrophysics) Roadmap Update (2023), [arXiv:2309.14561].

[42] M. Battisti *et al.*, Nuclear Instruments and Methods in Physics Research Section A: Accelerators, Spectrometers, Detectors and Associated Equipment **1069**, 169819 (2024), ISSN 0168-9002, URL `http://dx.doi.org/10.1016/j.nima.2024.169819`.

[43] K. Bernlohr, Astropart. Phys. **12**, 255 (2000), [arXiv:astro-ph/9908093].

[44] T. Hassan *et al.*, Astropart. Phys. **93**, 76 (2017), [arXiv:1705.01790].

[45] T. C. Weekes, in "International WE - Heraeus Summer School: Physics with Cosmic Accelerators," (2005), [arXiv:astro-ph/0508253].

[46] R. Mirzoyan, in "Handbook of X-ray and Gamma-ray Astrophysics," (2024), [arXiv:2406.15037].

[47] J. Cortina and C. Delgado, in C. Bambi and A. Santangelo, editors, "Handbook of X-ray and Gamma-ray Astrophysics," Springer (2024), ISBN 978-981-16-4544-0, [arXiv:2306.06415].

[48] C. Bambi and A. Santangelo, editors, *Handbook of X-ray and Gamma-ray Astrophysics*, Springer (2024), ISBN 978-981-16-4544-0.

[49] G. Pühlhofer, F. Leuschner and H. Salzmann, in C. Bambi and A. Santangelo, editors, "Handbook of X-ray and Gamma-ray Astrophysics," Springer (2024), ISBN 978-981-16-4544-0, [arXiv:2405.11104].

[50] J. Albert *et al.* (MAGIC), Astrophys. J. **674**, 1037 (2008), [arXiv:0705.3244].

[51] O. Blanch and J. Sitarek, in C. Bambi and A. Santangelo, editors, "Handbook of X-ray and Gamma-ray Astrophysics," Springer (2024), ISBN 978-981-16-4544-0, [arXiv:2507.22585].

[52] J. Holder *et al.*, AIP Conf. Proc. **1085**, 657 (2009), [arXiv:0810.0474].

[53] D. Hanna and R. Mukherjee, in C. Bambi and A. Santangelo, editors, "Handbook of X-ray and Gamma-ray Astrophysics," Springer (2024), ISBN 978-981-16-4544-0, [arXiv:2507.09813].

[54] G. Pareschi (ASTRI), EPJ Web Conf. **319**, 01003 (2025).

[55] W. Hofmann and R. Zanin, in C. Bambi and A. Santangelo, editors, "Handbook of X-ray and Gamma-ray Astrophysics," Springer (2024), ISBN 978-981-16-4544-0, [arXiv:2305.12888].

[56] S. Zhang, PoS **ICRC2023**, 808 (2023).

[57] Z. Zhang, R. Yang and S. Zhang, arXiv e-prints arXiv:2509.20694 (2025), [arXiv:2509.20694].

[58] F. A. Aharonian *et al.*, Astropart. Phys. **15**, 335 (2001), [arXiv:astro-ph/0006163].

[59] C. Borwankar *et al.*, Astropart. Phys. **159**, 102960 (2024), [arXiv:2404.01649].

[60] A. Schliesser and R. Mirzoyan, Astropart. Phys. **24**, 382 (2005), [arXiv:astro-ph/0507617].

[61] S. Fegan, Astropart. Phys. **158**, 102948 (2024), [arXiv:2411.16434].

[62] V. Vassiliev, P. F. Brousseau and S. J. Fegan, Astropart. Phys. **28**, 10 (2007), [arXiv:astro-ph/0612718].

[63] L. Di Venere (CTA-SCT project), Nucl. Instrum. Meth. A **1056**, 168432 (2023).

[64] S. A. Mueller *et al.*, Astropart. Phys. **158**, 102933 (2024), [arXiv:2401.16148].

[65] D. Neise *et al.*, Nucl. Instrum. Meth. A **876**, 17 (2017).

[66] A. Hahn *et al.*, Nucl. Instrum. Meth. A **1064**, 169350 (2024), [arXiv:2404.14346].

[67] D. Malyshev and L. Mohrmann, in C. Bambi and A. Santangelo, editors, "Handbook of X-ray and Gamma-ray Astrophysics," Springer (2024), ISBN 978-981-16-4544-0, [arXiv:2309.02966].

[68] W. Hofmann *et al.*, Astropart. Phys. **122**, 135 (1999), [arXiv:astro-ph/9904234].

[69] M. de Naurois and L. Rolland, Astropart. Phys. **32**, 231 (2009), [arXiv:0907.2610].

[70] R. D. Parsons and J. A. Hinton, Astropart. Phys. **56**, 26 (2014), [arXiv:1403.2993].

[71] D. Heck *et al.*, FZKA-6019 (1998).

[72] M. Gaug *et al.*, Astrophys. J. Suppl. **243**, 1, 11 (2019), [arXiv:1907.04375].

[73] F. Schmuckermaier *et al.*, Astron. Astrophys. **673**, A2 (2023), [arXiv:2302.12072].

[74] A. Donath *et al.* (Gammapy), Astron. Astrophys. **678**, A157 (2023), [arXiv:2308.13584].

[75] D. Berge, S. Funk and J. Hinton, Astron. Astrophys. **466**, 1219 (2007), [arXiv:astro-ph/0610959].

[76] V. A. Acciari *et al.* (MAGIC), Astron. Astrophys. **635**, A158 (2020), [arXiv:2001.09566].

[77] Z. Zhang *et al.*, Chin. Phys. C **49**, 3, 035001 (2025), [arXiv:2409.14382].

[78] M. Holler *et al.* (H.E.S.S.), PoS **ICRC2015**, 847 (2016), [arXiv:1509.02902].

[79] N. Park (VERITAS), PoS **ICRC2015**, 771 (2016), [arXiv:1508.07070].

[80] T. C. Weekes *et al.*, Astrophys. J. **342**, 379 (1989).

[81] E. Aliu *et al.* (MAGIC), Science **322**, 1221 (2008), [arXiv:0809.2998].

[82] F. Aharonian *et al.* (H.E.S.S.), Astron. Astrophys. **686**, A308 (2024), [arXiv:2403.12608].

[83] `http://tevcat.org/`.

[84] F. Aharonian *et al.* (H.E.S.S.), Astrophys. J. **636**, 777 (2006), [arXiv:astro-ph/0510397].

[85] B. S. Acharya *et al.* (CTA Consortium), *Science with the Cherenkov Telescope Array*, WSP (2018), ISBN 978-981-327-008-4, [arXiv:1709.07997].

[86] K. Abe *et al.* (CTA-LST Project), Astron. Astrophys. **690**, A167 (2024), [arXiv:2407.02343].

[87] S. Abe *et al.* (MAGIC), Mon. Not. Roy. Astron. Soc. **529**, 4, 4387 (2024), [arXiv:2402.04755].

[88] A. Acharyya *et al.* (VERITAS), Astrophys. J. **966**, 1, 28 (2024), [arXiv:2401.01853].

[89] N. Vogel *et al.*, Mon. Not. Roy. Astron. Soc. **537**, 3, 2334 (2025), [arXiv:2411.16471].

[90] A. Bernstein *et al.*, *Report on the Depth Requirements for a Massive Detector at Homestake* (2009), [arXiv:0907.4183].

[91] A. Abusleme *et al.* (JUNO), Chin. Phys. C **49**, 1, 013003 (2025), [arXiv:2405.17860].

[92] G. Bellini *et al.* (BOREXINO), Nature **512**, 7515, 383 (2014).

[93] M. Yeh *et al.*, Nucl. Instrum. Meth. A **660**, 51 (2011).

[94] S. D. Biller, E. J. Leming and J. L. Paton, Nucl. Instrum. Meth. A **972**, 164106 (2020), [arXiv:2001.10825].

[95] J. Boger *et al.* (SNO), Nucl. Instrum. Meth. A **449**, 172 (2000), [arXiv:nucl-ex/9910016].

[96] T. K. Gaisser, F. Halzen and T. Stanev, Phys. Rept. **258**, 173 (1995), [Erratum: Phys. Rept. 271, 355 (1996)], [hep-ph/9410384].

[97] J. G. Learned and K. Mannheim, Ann. Rev. Nucl. Part. Sci. **50**, 679 (2000).

[98] U. F. Katz and C. Spiering, Prog. Part. Nucl. Phys. **67**, 651 (2012), [arXiv:1111.0507].

[99] M. G. Aartsen *et al.* (IceCube), J. Phys. **G44**, 5, 054006 (2017), [arXiv:1607.02671].

[100] S. Adrián-Martínez *et al.* (KM3NeT), J. Phys. **G43**, 8, 084001 (2016), [arXiv:1601.07459].

[101] A. Gazizov and M. P. Kowalski, Comput. Phys. Commun. **172**, 203 (2005), [arXiv:astro-ph/0406439].

[102] A. D. Avrorin *et al.*, Phys. Part. Nucl. **46**, 2, 211 (2015).

[103] M. G. Aartsen *et al.* (IceCube), JINST **12**, 03, P03012 (2017), [arXiv:1612.05093].

[104] M. G. Aartsen *et al.* (IceCube-Gen2), J. Phys. G **48**, 6, 060501 (2021), [arXiv:2008.04323].

[105] M. Agostini *et al.* (P-ONE), Nature Astron. **4**, 10, 913 (2020), [arXiv:2005.09493].

[106] Z. P. Ye *et al.* (TRIDENT), Nature Astron. **7**, 12, 1497 (2023), [arXiv:2207.04519].

[107] T.-Q. Huang *et al.*, PoS **ICRC2023**, 1080 (2023).

[108] H. Zhang *et al.*, Astropart. Phys. **171**, 103123 (2025), [arXiv:2408.05122].

[109] A. Albert *et al.* (ANTARES), Phys. Rept. **1121-1124**, 1 (2025), [arXiv:2504.09473].

[110] F. Hu, PoS **ICRC2023**, 1203 (2023).

[111] T. Huege, Phys. Rept. **620**, 1 (2016), [arXiv:1601.07426].

[112] F. G. Schroder, Prog. Part. Nucl. Phys. **93**, 1 (2017), [arXiv:1607.08781].

[113] G. A. Askar'yan, Sov. Phys. JETP **14**, 2, 441 (1962), [Zh. Eksp. Teor. Fiz.41,616(1961)].

[114] G.A. Askaryan, Sov. Phys. JETP **21**, 658 (1965).

[115] E. Zas, F. Halzen and T. Stanev, Phys. Rev. D **45**, 362 (1992).

[116] C. W. James *et al.*, Phys. Rev. **E84**, 056602 (2011), [arXiv:1007.4146].

[117] C. W. James, Phys. Rev. D **105**, 2, 023014 (2022), [arXiv:2201.01298].

[118] S. Chiche *et al.*, Phys. Rev. Lett. **132**, 23, 231001 (2024), [arXiv:2404.14541].

[119] J. Alvarez-Muniz, R. A. Vazquez and E. Zas, Phys. Rev. **D62**, 063001 (2000), [arXiv:astro-ph/0003315].

[120] C. Glaser *et al.*, Eur. Phys. J. C **80**, 77 (2020), [arXiv:1906.01670].

[121] D. Saltzberg *et al.*, Phys. Rev. Lett. **86**, 2802 (2001), [hep-ex/0011001].

[122] O. Scholten *et al.*, J. Phys. Conf. Ser. **81**, 012004 (2007).

[123] J. Alvarez-Muñiz *et al.*, Phys. Rev. D **74**, 023007 (2006), URL `https://link.aps.org/doi/10.1103/PhysRevD.74.023007`.

[124] L. Gerhardt and S. R. Klein, Phys. Rev. **D82**, 074017 (2010), [arXiv:1007.0039].

[125] J. Alvarez-Muniz, R. A. Vazquez and E. Zas, Phys. Rev. **D61**, 023001 (2000), [arXiv:astro-ph/9901278].

[126] D. García-Fernández, A. Nelles and C. Glaser, Phys. Rev. D **102**, 8, 083011 (2020), [arXiv:2003.13442].

[127] S. R. Klein, *Probing high-energy interactions of atmospheric and astrophysical neutrinos* (2020), [arXiv:1906.02221].

[128] K. Greisen, Phys. Rev. Lett. **16**, 748 (1966).

[129] G. T. Zatsepin and V. A. Kuzmin, JETP Lett. **4**, 78 (1966), [Pisma Zh. Eksp. Teor. Fiz.4,114(1966)].

[130] A. A. Halim *et al.* (Pierre Auger), JCAP **05**, 024 (2023), [arXiv:2211.02857].

[131] A. Connolly and A. G. Vieregg, *Radio Detection of High Energy Neutrinos*, chapter 15, 217–240, World Scientific (2017), URL `https://www.worldscientific.com/doi/abs/10.1142/9789814759410_0015`.

[132] R. Abbasi *et al.* (IceCube), Astropart. Phys. **34**, 382 (2011), [arXiv:1004.1694].

[133] P. Allison *et al.* (ARA), Astropart. Phys. **108**, 63 (2019), [arXiv:1712.03301].

[134] A. Anker *et al.* (ARIANNA), JCAP **1911**, 030 (2019), [arXiv:1909.02677].

[135] J. A. Aguilar *et al.* (RNO-G), Eur. Phys. J. C **82**, 2, 147 (2022), [arXiv:2107.02604].

[136] I. Plaisier, S. Bouma and A. Nelles, Eur. Phys. J. C **83**, 5, 443 (2023), [arXiv:2302.00054].

[137] A. G. Vieregg, K. Bechtol and A. Romero-Wolf, JCAP **1602**, 02, 005 (2016), [arXiv:1504.08006].

[138] J. A. Aguilar *et al.*, Astropart. Phys. **145**, 102790 (2023), [arXiv:2103.06079].

[139] S. W. Barwick *et al.* (ARIANNA), Astropart. Phys. **90**, 50 (2017), [arXiv:1612.04473].

[140] S.-H. Wang *et al.* (TAROGE, Arianna), JCAP **11**, 022 (2022), [arXiv:2207.10616].

[141] S. Aiello *et al.* (KM3NeT), Nature **638**, 8050, 376 (2025), [Erratum: Nature 640, E3 (2025)].

[142] R. Abbasi *et al.* ((IceCube Collaboration)§, IceCube), Phys. Rev. Lett. **135**, 3, 031001 (2025), [arXiv:2502.01963].

[143] A. Aab *et al.* (Pierre Auger), JCAP **1910**, 10, 022 (2019), [arXiv:1906.07422].

[144] J. D. Bray *et al.*, Phys. Rev. **D91**, 6, 063002 (2015), [arXiv:1502.03313].

[145] O. Scholten *et al.*, Phys. Rev. Lett. **103**, 191301 (2009), [arXiv:0910.4745].

[146] P. W. Gorham *et al.* (ANITA), Phys. Rev. **D99**, 12, 122001 (2019), [arXiv:1902.04005].

[147] P. Allison *et al.* (ARA), Phys. Rev. D **102**, 4, 043021 (2020), [arXiv:1912.00987].

[148] A. Anker *et al.* (ARIANNA), JCAP **03**, 053 (2020), [arXiv:1909.00840].

[149] T. Winchen *et al.*, J. Phys. Conf. Ser. **1181**, 1, 012077 (2019), [arXiv:1903.08472].

[150] A. van Vliet, R. Alves Batista and J. R. Hörandel, Phys. Rev. D **100**, 2, 021302 (2019), [arXiv:1901.01899].

[151] S. Barwick *et al.*, Journal of Glaciology **51**, 173, 231–238 (2005).

[152] J.A. Dowdeswell and S. Evans, Rept. on Prog. in Phys. **67**, 1821 (2004).

[153] S. W. Barwick *et al.*, JCAP **1807**, 07, 055 (2018), [arXiv:1804.10430].

[154] C. Deaconu *et al.*, Phys. Rev. **D98**, 4, 043010 (2018), [arXiv:1805.12576].

[155] P. W. Gorham *et al.* (ANITA), Phys. Rev. Lett. **103**, 051103 (2009), [arXiv:0812.2715].

[156] P. W. Gorham *et al.* (ANITA), Phys. Rev. Lett. **121**, 16, 161102 (2018), [arXiv:1803.05088].

[157] P. W. Gorham *et al.* (ANITA), Phys. Rev. Lett. **126**, 7, 071103 (2021), [arXiv:2008.05690].

[158] A. Abdul Halim *et al.* (Pierre Auger), Phys. Rev. Lett. **134**, 12, 121003 (2025), [arXiv:2502.04513].

[159] I. Kravchenko *et al.* (RICE), Phys. Rev. **D73**, 082002 (2006), [arXiv:astro-ph/0601148].

[160] P. Allison *et al.* (ARA), Phys. Rev. **D93**, 8, 082003 (2016), [arXiv:1507.08991].

[161] J. Avva *et al.*, Nucl. Instrum. Meth. **A869**, 46 (2017), [arXiv:1605.03525].

[162] J. A. Aguilar *et al.* (RNO-G), JINST **16**, 03, P03025 (2021), [arXiv:2010.12279].

[163] R.D. Dagkesamanskii and I.M. Zheleznykh, Sov. Phys. JETP Lett. **50**, 233 (1989).

[164] G. R. Olhoeft and D. W. Strangway, Earth and Planetary Science Letters **24**, 3, 394 (1975).

[165] J. D. Bray, Astropart. Phys. **77**, 1 (2016), [arXiv:1601.02980].

[166] C. W. James *et al.*, EPJ Web Conf. **135**, 04001 (2017), [arXiv:1704.05336].

[167] A. Aab *et al.* (Pierre Auger), Phys. Rev. Lett. **116**, 24, 241101 (2016), [arXiv:1605.02564].

[168] P. A. Bezyazeekov *et al.* (Tunka-Rex), Phys. Rev. **D97**, 12, 122004 (2018), [arXiv:1803.06862].

[169] S. Buitink *et al.* (LOFAR), Phys. Rev. **D90**, 8, 082003 (2014), [arXiv:1408.7001].

[170] A. Abdul Halim *et al.* (Pierre Auger), Phys. Rev. Lett. **132**, 2, 021001 (2024), [arXiv:2310.19963].

[171] D. Fargion, Astrophys. J. **570**, 909 (2002), [arXiv:astro-ph/0002453].

[172] X. Bertou *et al.*, Astropart. Phys. **17**, 183 (2002), [arXiv:astro-ph/0104452].

[173] J. L. Feng *et al.*, Phys. Rev. Lett. **88**, 161102 (2002), [hep-ph/0105067].

[174] P. Abreu *et al.* (Pierre Auger), PoS **ICRC2021**, 262 (2021).

[175] Q. Abarr *et al.* (PUEO), JINST **16**, 08, P08035 (2021), [arXiv:2010.02892].

[176] A. Corstanje *et al.*, Phys. Rev. D **112**, 2, 023017 (2025), [arXiv:2504.16873].

[177] J. Álvarez Muñiz *et al.* (GRAND), Sci. China Phys. Mech. Astron. **63**, 1, 219501 (2020), [arXiv:1810.09994].

[178] D. Nygren, eConf **C740805**, 58 (1974).

[179] V. Chepel and H. Araujo, JINST **8**, R04001 (2013), [arXiv:1207.2292].

[180] E. Aprile and T. Doke, Rev. Mod. Phys. **82**, 2053 (2010), [arXiv:0910.4956].

[181] D. Gonzalez-Diaz, F. Monrabal and S. Murphy, Nucl. Instrum. Meth. A **878**, 200 (2018), [arXiv:1710.01018].

[182] E. Aprile *et al.*, *Noble Gas Detectors*, Wiley (2008), ISBN 978-3-527-40597-8, 978-3-527-61002-0.

[183] A. I. Bolozdynya, *Emission detectors*, World Scientific (2010).

[184] L. Baudis, Phil. Trans. Roy. Soc. Lond. A **382**, 2266, 20230083 (2023), [arXiv:2311.05320].

[185] D. S. Akerib *et al.* (LUX), Phys. Rev. D **97**, 11, 112002 (2018), [arXiv:1802.06162].

[186] B. Lenardo *et al.*, IEEE Trans. Nucl. Sci. **62**, 6, 3387 (2015), [arXiv:1412.4417].

[187] W. F. Schmidt, IEEE Trans. Electric. Insul. **19**, 389 (1984).

[188] L. Baudis *et al.*, Eur. Phys. J. C **83**, 8, 717 (2023), [arXiv:2303.13963].

[189] J. Albert *et al.* (EXO-200), Phys. Rev. C **89**, 1, 015502 (2014), [arXiv:1306.6106].

[190] A. Gando *et al.* (KamLAND-Zen), Phys. Rev. Lett. **122**, 19, 192501 (2019), [arXiv:1901.03871].

[191] E. Aprile *et al.* (XENON), Phys. Rev. C **106**, 2, 024328 (2022), [arXiv:2205.04158].

[192] J. Aalbers *et al.* (LZ), J. Phys. G **52**, 1, 015103 (2025), [arXiv:2408.17391].

[193] Z. Bo *et al.* (PandaX-4T, PandaX), JHEP **05**, 119 (2025), [arXiv:2411.14355].

[194] J. B. Albert *et al.* (EXO-200), Phys. Rev. D **96**, 9, 092001 (2017), [arXiv:1704.05042].

[195] K. Abe *et al.* (XMASS), PTEP **2018**, 5, 053D03 (2018), [arXiv:1801.03251].

[196] T. Doke *et al.*, Jap. J. Appl. Phys. **41**, 1538 (2002).

[197] C. E. Dahl, *The Physics of Background Discrimination in Liquid Xenon, and First Results from XENON10 in the Hunt for WIMP Dark Matter*, Ph.D. thesis, Princeton University (2009).

[198] L. Baudis, P. Sanchez-Lucas and K. Thieme, Eur. Phys. J. C **81**, 12, 1060 (2021), [arXiv:2109.07151].

[199] G. Anton *et al.* (EXO-200), Phys. Rev. C **101**, 6, 065501 (2020), [arXiv:1908.04128].

[200] J. J. Gomez-Cadenas, F. Monrabal Capilla and P. Ferrario, Front. in Phys. **7**, 51 (2019), [arXiv:1903.02435].

[201] M. S. J. Lindhard, V. Nielsen and P. Thomsen, Kgl. Danske Videnskab., Selskab. Mat. Fys. Medd **33**, 1 (1963).

[202] A. Hitachi and A. Mozumder (2019), [arXiv:1903.05815].

[203] P. Sorensen and C. E. Dahl, Phys. Rev. D **83**, 063501 (2011), [arXiv:1101.6080].

[204] M. Szydagis *et al.*, JINST **6**, P10002 (2011), [arXiv:1106.1613].

[205] G. Pereira, C. Silva and V. N. Solovov (LZ), JINST **18**, 04, C04007 (2023).

[206] E. Aprile *et al.* (XENON), Eur. Phys. J. C **80**, 8, 785 (2020), [arXiv:2003.03825].

[207] G. Anton *et al.* (EXO-200), Phys. Rev. Lett. **123**, 16, 161802 (2019), [arXiv:1906.02723].

[208] D. Nygren, Nucl. Instrum. Meth. A **603**, 337 (2009).

[209] J. Renner *et al.* (NEXT), JHEP **10**, 230 (2019), [arXiv:1905.13110].

[210] P. Agnes *et al.* (DarkSide), Nucl. Instrum. Meth. A **904**, 23 (2018), [arXiv:1802.01427].

[211] P. Abratenko *et al.* (MicroBooNE), JINST **16**, 09, P09025 (2021), [arXiv:2104.06551].

[212] Y. Li *et al.*, Nucl. Instrum. Meth. A **816**, 160 (2016), [arXiv:1508.07059].

[213] J. B. Albert *et al.* (EXO-200), Phys. Rev. C **95**, 2, 025502 (2017), [arXiv:1609.04467].

[214] M. Babicz *et al.*, JINST **15**, 09, P09009 (2020), [arXiv:2002.09346].

[215] E. Aprile *et al.* (XENON), PTEP **2022**, 5, 053H01 (2022), [arXiv:2112.12231].

[216] P. Agnes *et al.* (DarkSide), Phys. Rev. D **98**, 10, 102006 (2018), [arXiv:1802.07198].

[217] E. Aprile *et al.* (XENON), Phys. Rev. Lett. **129**, 16, 161805 (2022), [arXiv:2207.11330].

[218] P. Agnes (DarkSide), EPJ Web Conf. **280**, 06003 (2023).

[219] D. S. Akerib *et al.* (LZ), Nucl. Instrum. Meth. A **953**, 163047 (2020), [arXiv:1910.09124].

[220] Y. Meng *et al.* (PandaX-4T), Phys. Rev. Lett. **127**, 26, 261802 (2021), [arXiv:2107.13438].

[221] E. Aprile *et al.* (XENON), JCAP **11**, 031 (2020), [arXiv:2007.08796].

[222] S. Kravitz *et al.*, Eur. Phys. J. C **80**, 3, 262 (2020), [arXiv:1909.08730].

[223] J. Aalbers *et al.* (XLZD), Eur. Phys. J. C (2024), [arXiv:2410.17137].

[224] X. Wang *et al.*, JINST **18**, 05, P05028 (2023), [arXiv:2301.06044].

[225] J. Aalbers *et al.* (DARWIN), JCAP **1611**, 11, 017 (2016), [arXiv:1606.07001].

[226] J. Aalbers *et al.*, J. Phys. G **50**, 1, 013001 (2023), [arXiv:2203.02309].

[227] P. Agnes *et al.* (DarkSide), Phys. Rev. Lett. **130**, 10, 101002 (2023), [arXiv:2207.11968].

[228] S. Li *et al.* (PandaX), Phys. Rev. Lett. **130**, 26, 261001 (2023), [arXiv:2212.10067].

[229] E. Aprile *et al.* (XENON), Phys. Rev. Lett. **129**, 16, 161805 (2022), [arXiv:2207.11330].

[230] J. Aalbers *et al.* (LZ), Phys. Rev. D **108**, 7, 072006 (2023), [arXiv:2307.15753].

[231] Z. Bo *et al.* (PandaX), Phys. Rev. Lett. **133**, 19, 191001 (2024), [arXiv:2407.10892].

[232] E. Aprile *et al.* (XENON), Phys. Rev. Lett. **133**, 19, 191002 (2024), [arXiv:2408.02877].

[233] E. Aprile *et al.* (XENON), Phys. Rev. X **15**, 3, 031079 (2025), [arXiv:2502.04209].

[234] T. N. Thorpe (DarkSide-20k), SciPost Phys. Proc. **12**, 069 (2023), [arXiv:2210.00322].

[235] G. Plante *et al.*, Eur. Phys. J. C **82**, 10, 860 (2022), [arXiv:2205.07336].

[236] A. Abdukerim *et al.* (PandaX), Sci. China Phys. Mech. Astron. **68**, 2, 221011 (2025), [arXiv:2402.03596].

[237] K. Stifter (LZ), J. Phys. Conf. Ser. **1468**, 1, 012016 (2020).

[238] R. Anthony-Petersen *et al.* (SPICE, HeRALD), Phys. Rev. D **110**, 7, 072006 (2024), [arXiv:2307.11877].

[239] B. von Krosigk *et al.*, SciPost Phys. Proc. **12**, 016 (2023), [arXiv:2209.10950].

[240] R. E. Lanou, H. J. Maris and G. M. Seidel, Phys. Rev. Lett. **58**, 2498 (1987).

[241] F. D. Amaro *et al.*, Phys. Lett. B **855**, 138759 (2024).

[242] G. Anton *et al.* (EXO-200), Phys. Rev. Lett. **123**, 16, 161802 (2019), [arXiv:1906.02723].

[243] G. Adhikari *et al.* (nEXO), J. Phys. G **49**, 1, 015104 (2022), [arXiv:2106.16243].

[244] A. Simón *et al.* (NEXT), JHEP **07**, 146 (2021), [arXiv:2102.11931].

[245] P. Ferrario *et al.* (NEXT), JHEP **10**, 052 (2019), [arXiv:1905.13141].

[246] P. Novella *et al.* (NEXT), Phys. Rev. C **105**, 5, 055501 (2022), [arXiv:2111.11091].

[247] C. Adams *et al.* (NEXT) (2025), [arXiv:2505.17848].

[248] C. Adams *et al.* (NEXT), JHEP **2021**, 08, 164 (2021), [arXiv:2005.06467].

[249] A. D. McDonald *et al.*, Phys. Rev. Lett. **120**, 13, 132504 (2018), [arXiv:1711.04782].

[250] P. Herrero-Gómez *et al.* (NEXT), Nature Commun. **13**, 1, 7741 (2022), [arXiv:2201.09099].

[251] H. Rasiwala *et al.* (nEXO Ba-tagging group), Nucl. Instrum. Meth. B **541**, 298 (2023), [arXiv:2303.04698].

[252] W. Zhang *et al.* (PandaX-III), JINST **18**, 12, C12001 (2023), [arXiv:2311.13396].

[253] S. Wen *et al.*, Nucl. Instrum. Meth. A **1062**, 169206 (2024).

[254] E. Aprile *et al.* (XENON), Nature **568**, 7753, 532 (2019), [arXiv:1904.11002].

[255] G. Martínez-Lema *et al.* (NEXT), JHEP **21**, 203 (2020), [arXiv:2006.07320].

[256] C. Wittweg *et al.*, Eur. Phys. J. C **80**, 12, 1161 (2020), [arXiv:2002.04239].

[257] S. Zhang *et al.* (PandaX), Sci. Bull. **70**, 1779 (2025), [arXiv:2412.13979].

[258] L. Luo *et al.* (PANDA-X), JHEP **05**, 089 (2025), [arXiv:2502.03017].

[259] X. Yan *et al.* (PandaX), Phys. Rev. Lett. **132**, 15, 152502 (2024), [arXiv:2312.15632].

[260] D. S. Akerib *et al.* (LZ), Phys. Rev. C **102**, 1, 014602 (2020), [arXiv:1912.04248].

[261] D. S. Akerib *et al.* (LZ), Phys. Rev. C **104**, 6, 065501 (2021), [arXiv:2104.13374].

[262] F. Agostini *et al.* (DARWIN), Eur. Phys. J. C **80**, 9, 808 (2020), [arXiv:2003.13407].

[263] J. Aalbers *et al.* (XLZD), J. Phys. G **52**, 4, 045102 (2025), [arXiv:2410.19016].

[264] C. Enss, editor, *Cryogenic particle detection*, volume 99 of *Topics in applied physics*, Springer, Berlin, Germany (2005).

[265] K. Pretzl, *Cryogenic Detectors* (2020).

[266] *Proc. of the Low Temperature Detectors for Neutrinos and Dark Matter*, Low Temperature Detectors for Neutrinos and Dark Matter (start 1987).

[267] G. H. Rieke, *Detection of Light*, Cambridge University Press, 3rd edition (2021).

[268] H. Kraus, Superconductor Science and Technology **9**, 10, 827 (1996), URL `https://doi.org/10.1088/0953-2048/9/10/001`.

[269] M. H. Devoret, A. Wallraff and J. M. Martinis, Superconducting Qubits: A Short Review (2004), [arXiv:cond-mat/0411174], URL `https://arxiv.org/abs/cond-mat/0411174`.

[270] R. Linehan *et al.*, Phys. Rev. D **111**, 063047 (2025), URL `https://link.aps.org/doi/10.1103/PhysRevD.111.063047`.

[271] C. Fink *et al.*, Physical Review Applied **22**, 5 (2024), ISSN 2331-7019, URL `http://dx.doi.org/10.1103/PhysRevApplied.22.054009`.

[272] K. Ramanathan *et al.* (2024), [arXiv:2405.17192].

[273] A. V. Dixit *et al.*, Phys. Rev. Lett. **126**, 14, 141302 (2021), [arXiv:2008.12231].

[274] J. Zmuidzinas, Annual Review of Condensed Matter Physics **3**, 1, 169 (2012), URL `https://doi.org/10.1146/annurev-conmatphys-020911-125022`.

[275] S. Doyle *et al.*, Journal of Low Temperature Physics **151**, 1, 530 (2008), URL `https://doi.org/10.1007/s10909-007-9685-2`.

[276] K. Irwin and G. Hilton, *Transition-Edge Sensors*, 63–150, Springer Berlin Heidelberg, Berlin, Heidelberg (2005), ISBN 978-3-540-31478-3, URL `https://doi.org/10.1007/10933596_3`.

[277] F. Paolucci and F. Giazotto, Instruments **5**, 2 (2021), ISSN 2410-390X, URL `https://www.mdpi.com/2410-390X/5/2/14`.

[278] S. B. Bandler *et al.*, J. Low Temp. Phys. **93**, 709 (1993).

[279] D. Prele, Journal of Instrumentation **10**, 08, C08015 (2015), URL `https://doi.org/10.1088/1748-0221/10/08/c08015`.

[280] Y. Li *et al.* (CLASS), Astrophys. J. **986**, 2, 111 (2025), [arXiv:2501.11904].

[281] S. e. a. A. C. Naess, arXiv e-prints (2025), aCT data from 2017–2022; Accessed 2025-08-13, URL `https://arxiv.org/abs/2503.14451`.

[282] B. Westbrook and the POLARBEAR/Simons Array Collaboration, Journal of Low Temperature Physics **193**, 5?6, 758?770 (2018), ISSN 1573-7357, URL `http://dx.doi.org/10.1007/s10909-018-2059-0`.

[283] N. Galitzki *et al.* (SO), Astrophys. J. Suppl. **274**, 2, 33 (2024), [arXiv:2405.05550].

[284] S. e. a. Thoen, arXiv e-prints (2024), accessed 2025-08-13, URL `https://arxiv.org/abs/2407.17019`.

[285] F. e. a. Paonessa, arXiv e-prints (2025), URL `https://arxiv.org/abs/2506.22617`.

[286] A. Mennella *et al.* (QUBIC), EPJ Web Conf. **293**, 00030 (2024), [arXiv:2311.02779].

[287] E. Allys *et al.* (LiteBIRD), PTEP **2023**, 4, 042F01 (2023), [arXiv:2202.02773].

[288] E. Fiorini and T. Niinikoski, Nucl. Instrum. Meth. A **224**, 83 (1984).

[289] S. H. Moseley, J. C. Mather and D. McCammon, Thermal detectors as x-ray spectrometers (1984).

[290] V. Barger and D. Cline (1985), telemark, 1984.

[291] A. Blasi *et al.* (1985), `I.N.F.N./BE-85/2`, internal report.

[292] D. Q. Adams *et al.* (CUORE), Science **0**, 0, eadp6474, URL `https://www.science.org/doi/abs/10.1126/science.adp6474`.

[293] W. R. Armstrong *et al.* (CUPID) (2019), [arXiv:1907.09376].

[294] K. Alfonso *et al.* (CUPID) (2025), [arXiv:2504.14369].

[295] O. Azzolini *et al.* (CUPID), Phys. Rev. Lett. **129**, 11, 111801 (2022), [arXiv:2206.05130].

[296] C. Augier *et al.*, Eur. Phys. J. C **82**, 11, 1033 (2022), [arXiv:2202.08716].

[297] A. Agrawal *et al.* (AMoRE), Eur. Phys. J. C **85**, 2, 172 (2025), [Erratum: Eur.Phys.J.C 85, 256 (2025)], [arXiv:2407.12227].

[298] D. Mccammon *et al.* (1984).

[299] G. Drexlin *et al.*, Adv. High Energy Phys. **2013**, 293986 (2013), [arXiv:1307.0101].

[300] P. Filianin *et al.*, Phys. Rev. Lett. **127**, 7, 072502 (2021), [arXiv:2108.07039].

[301] D. Pergolesi *et al.*, Nucl. Instrum. Meth. A **559**, 349 (2006).

[302] M. Sisti *et al.*, Nuclear Instruments and Methods in Physics Research Section A: Accelerators, Spectrometers, Detectors and Associated Equipment **520**, 1, 125 (2004), ISSN 0168-9002, proceedings of the 10th International Workshop on Low Temperature Detectors, URL `https://www.sciencedirect.com/science/article/pii/S0168900203031814`.

[303] E. Ferri *et al.*, Phys. Procedia **61**, 227 (2015).

[304] C. Velte, *Measurement of a high energy resolution and highstatistics 163Ho electron capture spectrum for the ECHo experiment.*, Ph.D. thesis, U. Heidelberg (main) (2020).

[305] F. Mantegazzini *et al.*, Nucl. Instrum. Meth. A **1055**, 168564 (2023), [arXiv:2301.06455].

[306] B. K. Alpert *et al.* (2025), [arXiv:2503.19920].

[307] M. P. Croce *et al.*, J. Low Temp. Phys. **184**, 3-4, 958 (2016), [arXiv:1510.03874].

[308] M. Farino *et al.* (PTOLEMY) (2025), [arXiv:2503.10025].

[309] E. Armengaud *et al.* (EDELWEISS), Phys. Rev. D **86**, 051701 (2012), [arXiv:1207.1815].

[310] R. Agnese *et al.* (SuperCDMS), Phys. Rev. D **95**, 8, 082002 (2017), [arXiv:1610.00006].

[311] G. Angloher *et al.* (CRESST), Phys. Rev. D **110**, 8, 083038 (2024), [arXiv:2405.06527].

[312] G. Angloher *et al.* (2025), [arXiv:2505.01183].

[313] R. Ardito *et al.* (2005), [hep-ex/0501010].

[314] D. Q. Adams *et al.* (CUORE) (2024), [arXiv:2404.04453v1].

[315] A. Agrawal *et al.* (AMoRE), Phys. Rev. Lett. **134**, 8, 082501 (2025), [arXiv:2407.05618].

[316] S. Kim (AMoRE), PoS **TIPP2023**, 014 (2025).

[317] P. Luke *et al.*, Nucl. Instrum. Meth. A **289**, 406 (1990).

[318] B. Neganov *et al.*, J Low Temp Phys **93**, 417–422 (1993), URL `https://doi.org/10.1007/BF00693454`.

[319] M. F. Albakry *et al.* (SuperCDMS), Phys. Rev. D **111**, 1, 012006 (2025), [arXiv:2407.08085].

[320] E. Armengaud *et al.* (EDELWEISS), Phys. Rev. D **106**, 6, 062004 (2022), [arXiv:2203.03993].

[321] A. Armatol *et al.* (2025), [arXiv:2507.15732].

[322] *Snowmass2021-Letter of Interest The TESSERACT Dark Matter Project* (2020).

[323] A. Cruciani *et al.*, Appl. Phys. Lett. **121**, 21, 213504 (2022), [arXiv:2209.14806].

[324] T. Braine *et al.* (ADMX), Phys. Rev. Lett. **124**, 10, 101303 (2020), [arXiv:1910.08638].

[325] S. Ahn *et al.* (CAPP), Phys. Rev. X **14**, 3, 031023 (2024), [arXiv:2402.12892].

[326] *Snowmass2021-Letter of Interest Opening the Terahertz Axion Window* (2020).

[327] C. Augier *et al.* (Ricochet), Eur. Phys. J. C **84**, 2, 186 (2024), [arXiv:2306.00166].

[328] C. Bellenghi *et al.*, Eur. Phys. J. C **79**, 9, 727 (2019), [arXiv:1905.10611].

[329] I. Colantoni *et al.*, J. Low Temp. Phys. **199**, 3-4, 593 (2020).

[330] L. Pattavina *et al.* (RES-NOVA), JCAP **10**, 064 (2021), [arXiv:2103.08672].

[331] G. Heusser, Ann. Rev. Nucl. Part. Sci. **45**, 543 (1995).

[332] D. S. Akerib *et al.*, The European Physical Journal C **80**, 11 (2020), URL `https://doi.org/10.1140%2Fepjc%2Fs10052-020-8420-x`.

[333] D. S. Leonard *et al.*, Nucl. Instrum. Meth. A **871**, 169 (2017), [arXiv:1703.10799].

[334] N. Abgrall *et al.*, Nucl. Instrum. Methods Phys. Res. A **828**, 22 (2016).

[335] E. Aprile *et al.* (XENON), Eur. Phys. J. C **82**, 7, 599 (2022), [arXiv:2112.05629].

[336] M. Laubenstein, International Journal of Modern Physics A **32**, 30, 1743002 (2017), URL `https://doi.org/10.1142/s0217751x17430023`.

[337] P. Scovell *et al.*, Astroparticle Physics **97**, 160 (2018), URL `https://doi.org/10.1016/j.astropartphys.2017.11.006`.

[338] G. Heusser *et al.*, The European Physical Journal C **75**, 11 (2015), URL `https://doi.org/10.1140%2Fepjc%2Fs10052-015-3704-2`.

[339] N. Jakubowski, Analytical and Bioanalytical Chemistry **392**, 5, 775 (2008), URL `https://doi.org/10.1007%2Fs00216-008-2374-4`.

[340] M. Clemenza, J. Radioanal. Nucl. Chem. **318**, 3, 1765 (2018).

[341] G. Heusser *et al.*, Applied Radiation and Isotopes **52**, 3, 691 (2000), URL `https://doi.org/10.1016%2Fs0969-8043%2899%2900231-6`.

[342] M. Wojcik, G. Zuzel and H. Simgen, International Journal of Modern Physics A **32**, 30, 1743004 (2017), URL `https://doi.org/10.1142%2Fs0217751x17430047`.

[343] A. Anker *et al.*, Nucl. Instrum. Methods Phys. Res. A **1081**, 170876, 170876 (2026).

[344] D. Wiebe, S. Lindemann and M. Schumann, Journal of Instrumentation **19**, 04, P04014 (2024), ISSN 1748-0221, URL `http://dx.doi.org/10.1088/1748-0221/19/04/P04014`.

[345] Y. Wu *et al.*, Nuclear Instruments and Methods in Physics Research Section A: Accelerators, Spectrometers, Detectors and Associated Equipment **1080**, 170771 (2025), ISSN 0168-9002, URL `http://dx.doi.org/10.1016/j.nima.2025.170771`.

[346] Y. Takeuchi *et al.*, Nuclear Instruments and Methods in Physics Research Section A: Accelerators, Spectrometers, Detectors and Associated Equipment **421**, 1-2, 334 (1999), URL `https://doi.org/10.1016%2Fs0168-9002%2898%2901204-2`.

[347] J. Kiko, Nuclear Instruments and Methods in Physics Research Section A: Accelerators, Spectrometers, Detectors and Associated Equipment **460**, 2-3, 272 (2001), URL `https://doi.org/10.1016%2Fs0168-9002%2800%2901082-2`.

[348] E. Hoppe *et al.*, Nuclear Instruments and Methods in Physics Research Section A: Accelerators, Spectrometers, Detectors and Associated Equipment **579**, 1, 486 (2007), URL `https://doi.org/10.1016%2Fj.nima.2007.04.101`.

[349] A. D. C.D. Christofferson, V.E. Giuseppe, in "Low Radiation Techniques, Jaca, Spain, 2019," (2019).

[350] R. Bunker *et al.*, Nuclear Instruments and Methods in Physics Research Section A: Accelerators, Spectrometers, Detectors and Associated Equipment **967**, 163870 (2020), URL `https://doi.org/10.1016/j.nima.2020.163870`.

[351] S. Bruenner *et al.*, The European Physical Journal C **81**, 4 (2021), URL `https://doi.org/10.1140/epjc/s10052-021-09047-2`.

[352] M. L. di Vacri *et al.*, Nucl. Instrum. Meth. A **994**, 165051 (2021), [arXiv:2006.12746].

[353] H. Loosli, Earth and Planetary Science Letters **63**, 1, 51 (1983), URL `https://doi.org/10.1016%2F0012-821x%2883%2990021-3`.

[354] D. Acosta-Kane *et al.*, Nuclear Instruments and Methods in Physics Research Section A: Accelerators, Spectrometers, Detectors and Associated Equipment **587**, 1, 46 (2008), URL `https://doi.org/10.1016%2Fj.nima.2007.12.032`.

[355] P. Agnes *et al.* (DarkSide), Phys. Rev. D **93**, 8, 081101 (2016), [Addendum: Phys.Rev.D 95, 069901 (2017)], [arXiv:1510.00702].

[356] H. O. Back *et al.*, in "Snowmass 2021," (2022), [arXiv:2203.09734].

[357] I. Bandac *et al.*, Appl. Radiat. Isot. **126**, 127 (2017).

[358] G. Ranucci, in "IEEE Symposium Conference Record Nuclear Science 2004.", volume 2, 804–809 Vol. 2 (2004).

[359] P. Adhikari *et al.*, The European Physical Journal C **80**, 4 (2020), URL `https://doi.org/10.1140%2Fepjc%2Fs10052-020-7789-x`.

[360] D. Budjáš *et al.*, Journal of Instrumentation **4**, 10, P10007 (2009), URL `https://doi.org/10.1088/1748-0221/4/10/p10007`.

[361] M. Agostini *et al.* (GERDA), Phys. Rev. Lett. **125**, 25, 252502 (2020), [arXiv:2009.06079].

[362] H. Acharya *et al.* (LEGEND) (2025), [arXiv:2505.10440].

[363] A. Simón *et al.* (NEXT), JHEP **21**, 146 (2020), [arXiv:2102.11931].

[364] G. Adhikari *et al.*, J. Phys. G Nucl. Part. Phys. **49**, 1, 015104 (2022).

[365] R. Agnese *et al.* (SuperCDMS Collaboration), Phys. Rev. Lett. **120**, 061802 (2018), URL `https://link.aps.org/doi/10.1103/PhysRevLett.120.061802`.

[366] W. Westphal *et al.*, Nucl. Instrum. Meth. A **559**, 372 (2006).

[367] S. Westerdale, E. Shields and F. Calaprice, Astroparticle Physics **79**, 10 (2016), URL `https://doi.org/10.1016%2Fj.astropartphys.2016.01.005`.

[368] Marco Selvi, The XENONnT Neutron Veto (2023), URL `https://indico.cern.ch/event/1188759/`.

[369] E. Aprile *et al.*, Eur. Phys. J. C Part. Fields **85**, 6 (2025).

[370] D. Akimov *et al.* (COHERENT), Science **357**, 6356, 1123 (2017), [arXiv:1708.01294].

[371] D. Akimov *et al.*, in "Snowmass 2021," (2022), [arXiv:2204.04575].

[372] H. Back *et al.* (Borexino Collaboration), Phys. Rev. C **74**, 045805 (2006), URL `https://link.aps.org/doi/10.1103/PhysRevC.74.045805`.

[373] C. Wiesinger, L. Pandola and S. Schönert, Eur. Phys. J. C **78**, 7, 597 (2018), [arXiv:1802.05040].

[374] J. Benziger *et al.*, Nuclear Instruments and Methods in Physics Research Section A: Accelerators, Spectrometers, Detectors and Associated Equipment **587**, 2-3, 277 (2008), URL `https://doi.org/10.1016/j.nima.2007.12.043`.

[375] K. Abe *et al.*, Nucl. Instrum. Meth. A **716**, 78 (2013), [arXiv:1301.2815].

[376] E. Aaron *et al.* (DarkSide-20k), Eur. Phys. J. C **83**, 5, 453 (2023), [arXiv:2301.09639].

[377] K.-P. Gradwohl *et al.*, Journal of Instrumentation **15**, 12, P12010 (2020), URL `https://doi.org/10.1088/1748-0221/15/12/p12010`.

[378] B. Suerfu, F. Calaprice and M. Souza, Physical Review Applied **16**, 1 (2021), URL `https://doi.org/10.1103/physrevapplied.16.014060`.

[379] I. Rivilla *et al.*, Nature **583**, 7814, 48 (2020), URL `https://doi.org/10.1038/s41586-020-2431-5`.

[380] A. McDonald *et al.*, Physical Review Letters **120**, 13 (2018), URL `https://doi.org/10.1103/physrevlett.120.132504`.